

國立交通大學

電控工程研究所

碩士論文

效率最佳化之單相無刷直流風扇馬達使用
霍爾感測器或無感測控制

Efficiency Optimization Control for Single-Phase Brushless
DC Fan Motors with or without Hall Sensor

研究生：陳煒超

指導教授：鄒應嶼 博士

中華民國 九十八年 十月

效率最佳化之單相無刷直流風扇馬達使用
霍爾感測器或無感測控制

Efficiency Optimization Control for Single-Phase
Brushless DC Fan Motors with or without Hall Sensor

研究生：陳煒超 Student: Wei-Chao Chen

指導教授：鄒應嶼 博士 Advisor: Dr. Ying-Yu Tzou

國立交通大學

電控工程研究所

碩士論文

A Thesis

Submitted to Institute of Electrical and Control Engineering

College of Electrical Engineering

National Chiao Tung University

in Partial Fulfillment of the Requirements

for the Degree of Master

in

Electrical and Control Engineering

October 2009

Hsinchu, Taiwan, Republic of China

中華民國九十八年十月

效率最佳化之單相無刷直流風扇馬達使用 霍爾感測器或無感測控制

研究生：陳煒超

指導教授：鄒應嶼 博士

國立交通大學電控工程研究所

中文摘要

本論文實現效率最佳化之單相無刷直流風扇馬達使用霍爾感測器或無感測控制策略。本文提出簡單的模型方法並配合適當的參數鑑別，建立符合單相無刷直流風扇馬達特性的數學模型，其非線性的轉子磁通量分布特色是利用建表的方式來代表。經由電腦模擬與實際量測結果比對後，可驗證該模型的準確性。本文比較不同的控制策略，包含開迴路硬換相電壓模式控制、開迴路軟換相電壓模式控制以及閉迴路電流模式控制，分析其電流波形以及運轉效率的優劣。本文結合閉迴路電流模式控制以及開迴路軟換相電壓模式控制的優點，配合霍爾感測器輸出訊號的回授，可使單相無刷直流風扇馬達在廣泛的速度範圍內達到效率最佳化。本論文亦實現高效率且低成本的單相無刷直流風扇馬達無感測驅動，延伸軟換相的控制方法，調整功率開關的空白時間，使線圈上的電流產生不連續導通的狀態，偵測其反抗電動勢的零交越點即為電流的換相點。為了解決無感測啟動的問題，本文配合單相馬達非對稱氣隙的特色，使用特殊的啟動機制，不論轉子初始位置在哪裡，皆可使馬達往既定的方向旋轉，並以 kick-off 的方式加速馬達，直到反抗電動勢大小足以提供無感測演算法正確的運作，便可切換到無感測驅動模式。在無感測驅動下，亦使用閉迴路電流模式的控制方法來提升風扇馬達的運轉效率，而電流命令係利用查表的方式來取代霍爾感測器的訊號。本文使用數位訊號處理器 (TMS320LF2407A) 驗證所提出控制策略的可行性與性能。實驗結果顯示，在有感測控制下使用效率最佳化的控制方法，其直流鏈電流的平均值至少有 12% 的改善，其相電流的方均根值至少有 10% 的改善，其相電流的峰值至少有 42% 的改善；在無感測控制下，可使風扇馬達穩定啟動並操作在廣泛的速度範圍，而且其運轉效率幾乎與有感測的結果相同。

Efficiency Optimization Control for Single-Phase Brushless DC Fan Motors with or without Hall Sensor

Student: Wei-Chao Chen

Advisor: Dr. Ying-Yu Tzou

Institute of Electrical and Control Engineering
National Chiao Tung University

Abstract

This thesis develops efficiency optimization control strategies for single-phase brushless dc (BLDC) fan motors with or without Hall sensor. A simple modeling method with feasible parameter identification is proposed to meet characteristics of single-phase BLDC fan motor. The nonlinear rotor flux distribution is modeled by a look-up table. With simulation assistance, the proposed model has been verified with measurement results. This thesis compares the different control strategies include open-loop voltage-mode control of hard-commutation scheme, open-loop voltage-mode control of soft-commutation scheme, and closed-loop current-mode control scheme, and analyzes the current response and overall efficiency. With the linear Hall sensor feedback, the advantages of current-mode control scheme and soft-commutation scheme are adopted to achieve maximum efficiency over the entire speed range. This thesis also develops a low-cost and high efficiency sensorless control for single-phase BLDC fan motor drives. The proposed scheme detects the back-EMF zero-crossing-point (ZCP) to realize current commutation without Hall sensor. An adjustable blanking time control method is used to ensure correct detection of the ZCP. To overcome the sensorless start-up problem, a specific strategy based on characteristic of asymmetric air gap is developed to ensure the motor running in predefined direction. Then, an open-loop control called kick-off speed up the fan motor to middle-speed where sensorless control algorithm based on the back-EMF can work properly. The closed-loop current-mode control scheme is also applied to improve the overall efficiency. However, the current reference is produced by look-up table to estimate the Hall sensor signal. Experimental implementation has been constructed on a single-chip DSP controller (TMS320LF2407A) to verify the performance and feasibility of the proposed control strategies. When using the control scheme with Hall sensor, experimental results show that there are at least a 12 % reduction for average value of dc-link current, a 10 % reduction for RMS value of phase current, and a 42% reduction for peak value of phase current. When using sensorless commutation control, the fan motor can start-up smoothly and operate under wide speed range, moreover, the overall efficiency is almost the same to the results of control scheme with Hall sensor.

誌 謝

首先要感謝我的老師鄒應嶼教授兩年來的指導，除了專業知識上的啟發之外，也讓我思考與解決問題的能力有很大的成長。謝謝老師在研究及教學上的督促鼓勵，生活上的關心，以及學習經驗的分享，相信這些在我以後的生活與工作上都將有極大的助益。

感謝育宗、晏詮與宗罄學長，在這兩年中給我許多的協助，除了課業上的問題外，也提供我很多寶貴的建議。感謝同窗戰友茗皓、宗翰、哲瑋與家豪昔日的相互扶持與鼓勵，謝謝你們在這些日子裡的陪伴，一起做研究一起歡樂日子讓人懷念，尤其是武漢研討會之旅，將會是人生最難忘的回憶之一。謝謝學弟哲瑋、彥勳、甫尊、政江、建成與智偉，有了你們的加入，讓實驗室充滿朝氣與笑容，也豐富我的研究生活；也希望將來大家在社會上都能夠很有成就，同時不要忘記我們永遠都是實驗室的夥伴。感謝月貴在一些行政事務與實驗器材購買上的幫助，減輕了我們許多工作的負擔。

最後要感謝我的父母、弟弟以及所有關心我的長輩，謝謝你們給我的支持與關懷，願與你們一同分享這份喜悅與榮耀。

謹以此論文獻給所有我的長輩與師長們…

陳煒超

2009 秋 於新竹交大

Table of Contents

Abstract (Chinese)	i
Abstract (English).....	ii
Acknowledgement.....	iii
Table of Contents	iv
List of Tables.....	vi
List of Figures	vii
Chapter 1 Introduction.....	1
1.1 Research Background and Recent Development.....	1
1.2 Research Motivation and Objectives.....	4
1.3 Thesis Organization.....	6
Chapter 2 Basic Operation of Single-Phase BLDC Fan Motors.....	7
2.1 Structure of Single-Phase BLDC fan motors.....	7
2.2 Mathematical Modeling.....	10
2.3 Parameter Identification.....	12
2.3.1 Electrical Parameters.....	12
2.3.2 Mechanical Parameters.....	14
2.4 A Study of Dynamic Behavior.....	17
2.4.1 Basic Operation Principle.....	17
2.4.2 Analyses of Steady-State Response.....	18
2.4.3 Verification of Proposed Model.....	23
Chapter 3 Efficiency Optimization of Single-Phase BLDC Fan Motor Drives.....	27
3.1 PWM Control Strategies.....	27
3.1.1 PWM Switching Scheme 1.....	28
3.1.2 PWM Switching Scheme 2.....	35
3.1.3 PWM Switching Scheme 3.....	37
3.1.4 PWM Switching Scheme 4.....	39
3.2 Open-Loop Voltage-Mode Control of Soft-Commutation Scheme.....	42
3.3 Efficiency Optimization Control Scheme.....	47
3.3.1 Principle of Efficiency Optimization.....	47
3.3.2 System Configuration.....	48
3.3.3 Digital Current-Loop Controller Design and Consideration.....	50

3.3.4	Analyses of Simulation Results.....	57
Chapter 4	Sensorless Control for Single-Phase BLDC Fan Motor Drives	63
4.1	Sensorless Control Scheme.....	63
4.1.1	Basic Operation Principle.....	63
4.1.2	Zero-Crossing Point Detection.....	66
4.2	Sensorless Start-Up Strategy.....	67
4.2.1	Starting Method based on Asymmetric Air Gap	67
4.2.2	Start-Up Procedure.....	70
4.2.3	Open-Loop Voltage-Mode Control without Hall sensor.....	72
4.3	Closed-Loop Current-Mode Control of Sensorless Motor Drives.....	76
4.3.1	System Configuration.....	76
4.3.2	Analyses of Simulation Results.....	78
Chapter 5	Laboratory Setup and Implementation of Single-Phase BLDC Fan Motor	
	Control System.....	82
5.1	Laboratory Setup	82
5.2	Software Implementation.....	84
5.3	Analyses of Experimental Results.....	87
5.3.1	Commutation Control with Hall Sensor.....	87
5.3.2	Sensorless Commutation Control.....	99
Chapter 6	Conclusions	105
6.1	Conclusions.....	105
6.2	Future Works.....	107
References	108
Vita	108

List of Tables

1.1	Functions of commercial drive IC.....	2
2.1	Parameters of the tested motor	16
3.1	Parameters and operation conditions for calculating power losses.....	35
5.1	Specifications of the tested motor	69



List of Figures

2.1	Structure of the single-phase BLDC fan motor (a) real motor configuration and (b) exploded perspective view	8
2.2	Cross-sectional view of stator and rotor assembly with asymmetric air gap	8
2.3	Operational principle of Hall sensor	9
2.4	Schematic of the full-bridge inverter and equivalent modeling for a single-phase BLDC fan motor.....	11
2.5	Block diagram for modeling of the single-phase BLDC fan motor	12
2.6	Step voltage input and current response.....	14
2.7	The table of rotor flux distribution versus rotor position	14
2.8	Speed response from stop to rotate.....	16
2.9	The open-loop voltage-mode control of hard-commutation scheme (a) the schematic of commutation control circuit and (b) operation waveform	18
2.10	Steady-state current response when using open-loop voltage-mode control of hard-commutation scheme	19
2.11	Steady-state torque response when using open-loop voltage-mode control of hard-commutation scheme.....	20
2.12	Equivalent dc-bus model of power stage.....	22
2.13	Steady-state response of dc-bus current	23
2.14	Simulation results with the open-loop voltage-mode control of hard-commutation scheme under (a) duty = 100%, (b) duty = 80%, and (c) duty = 50%	24
2.15	Phase current comparison between simulation result and experiment measurement (a) duty = 100%, (b) duty = 80%, (c) duty = 50%, and (d) duty = 20%	25
2.16	The RMS value of phase current and rotor speed curves under different duty ratios	26
3.1	Switch configuration of motor drives.....	28
3.2	(a) PWM switching scheme 1 and (b) macro view of switching pattern.	28
3.3	Model of transistor's characteristic	30
3.4	Conducting current of transistor S2 and S4.....	30
3.5	Conducting current of transistor S1 and S3.....	31
3.6	The switching transition during turn-on time and turn-off time.....	32
3.7	Model of diode's characteristic	33

3.8	Conducting current of diode D2 and D4.	34
3.9	Pie chart of total power losses for PWM switching scheme 1.	35
3.10	(a) PWM switching scheme 2 and (b) macro view of switching pattern.	37
3.11	Pie chart of total power losses for PWM switching scheme 2.	37
3.12	(a) PWM switching scheme 3 and (b) macro view of switching pattern.	39
3.13	Pie chart of total power losses for PWM switching scheme 3	39
3.14	(a) PWM switching scheme 4 and (b) macro view of switching pattern	41
3.15	Pie chart of total power losses for PWM switching scheme 4	41
3.16	The operation waveform for open-loop voltage-mode control of soft-commutation scheme.....	43
3.17	The steady-state waveforms when using soft-commutation scheme with different blanking times at 4000 RPM (a) no blanking time, (b) blanking time of 10% commutation cycle, and (c) blanking time of 15% commutation cycle.....	44
3.18	The equivalent circuit after turning off the switches.....	46
3.19	The steady-state waveforms when using soft-commutation scheme (a) 3000 RPM with blanking time of 10% commutation cycle and (b) 1000 RPM with blanking time of 5% commutation cycle.....	46
3.20	Architecture of closed-loop current-mode control system.	49
3.21	Current multiplier control scheme with linear Hall sensor feedback.....	49
3.22	The current response when motor is standstill.....	50
3.23	The operation principle of single-update-mode triangular-carrier modulator.....	51
3.24	The general digital PWM modulator.....	53
3.25	Frequency response of $G_{PWM}(s)$	53
3.26	Block diagram of current-loop control.....	54
3.27	The continuous time equivalent of current-loop control system.....	55
3.28	Block diagram of digital PI controller.....	57
3.29	Loop gain frequency response with $PI(s)$ and $PI(z)$	59
3.30	Simulation result of step response at operation point of 250 mA	59
3.31	Simulation results of steady-state response based on closed-loop current-mode control scheme (a) 4000 RPM, (b) 3000 RPM, (c) 1000 RPM, and (d) 500 RPM	61
3.32	The current-loop controller enters the limit region if the fan motor is over	

4000 RPM.....	62
3.33 If the fan motor accelerates over 4000RPM, the control system switches the control mode.....	62
4.1 Operation waveform of sensorless control method.....	65
4.2 Three possible relationships between the phase current and the back EMF.....	65
4.3 Operation waveform for back-EMF ZCP detection.....	66
4.4 Two possible rotor positions when motor is standstill.....	68
4.5 Motor state while positive current pulse is supplied at Position 1.....	69
4.6 Motor state while positive current pulse is supplied at Position 2.....	69
4.7 Motor state while negative current pulse is supplied at Position 1.....	69
4.8 Motor state while negative current pulse is supplied at Position 2.....	70
4.9 Sensorless start-up control steps for single-phase BLDC fan motors (a) inverter circuit and (b) control steps.....	71
4.10 Speed response during sensorless start-up procedure.....	72
4.11 Block diagram of open-loop voltage-mode sensorless control for single-phase BLDC fan motor.....	73
4.12 Sensorless start-up control from standstill to 4000 RPM.....	73
4.13 Simulation results of sensorless control at 4000 RPM (a) steady state waveforms of phase current and phase voltage and (b) Non-excited voltage sampling and ZCP detection.....	74
4.14 Sensorless start-up control from standstill to 1000 RPM.....	75
4.15 Simulation results of sensorless control at 1000 RPM (a) steady state waveforms of phase current and phase voltage and (b) Non-excited voltage sampling and ZCP detection.....	76
4.16 Block diagram of sensorless control system with closed-loop current-mode control.....	77
4.17 Current multiplier control scheme with estimated Hall sensor by look-up table.....	77
4.18 Simulation results of current-loop control at different speed operation (a) 4000 RPM, (b) 3000 RPM, (c) 1000 RPM, and (d) 500 RPM.....	80
4.19 Statistics curves for different control schemes (a) RMS value of phase current and (b) peak value of phase current.....	81
5.1 Schematic of the prototype control system for single-phase BLDC fan motor.....	83
5.2 Experimental setup for single-phase BLDC fan motor control system.....	83

5.3	Interrupt configuration in the DSP controller.....	85
5.4	Program flow chart for control algorithms (a) drive with Hall sensor (b) drive without Hall sensor.....	86
5.5	Overall functional block diagram of the single-phase BLDC fan motor control system.....	86
5.6	Steady-state response when using the open-loop voltage-mode control of hard-commutation scheme (a) 4000 RPM, (b) 3000 RPM, and (c) 1000 RPM.....	89
5.7	Steady-state response when using the soft-commutation control scheme (a) 4000 RPM, (b) 3000RPM, and (c) 1000 RPM.....	90
5.8	Step response at zero current (a) 400 mA step input and (b) 240 mA step input.....	91
5.9	Steady-state response of closed-loop current-mode control scheme at 3000 RPM (a) Hall sensor and phase current and (b) current reference and response	92
5.10	Steady-state response of closed-loop current-mode control scheme at 1000 RPM (a) Hall sensor and phase current and (b) current reference and response	93
5.11	Steady-state response of closed-loop current-mode control scheme at 500 RPM (a) Hall sensor and phase current and (b) current reference and response	94
5.12	When the fan motor over 4000 RPM, the working mode switches from current-loop control to soft-commutation control	95
5.13	Statistics curves of various control schemes (a) average value of dc-link current versus rotor speed, (b) RMS value of phase current versus rotor speed, and (c) peak value of phase current versus rotor speed.....	96
5.14	Percentage improvement for two methods (a) average value of dc-link current (b) RMS value of phase current, and (c) peak value of phase current.	97
5.15	Compare commercial IC with proposed control scheme (a) RMS value of phase current and (b) peak value of phase current.	98
5.16	ZCP detection procedure at 3000 RPM.....	99
5.17	Steady-state response of closed-loop current-mode sensorless control (a) 3000 RPM, (b) 2000 RPM, (c) 1000 RPM, and (d) 500 RPM.....	101
5.18	Sensorless start-up procedure (a) toward 3000 RPM and (b) toward 1000 RPM.....	102

5.19 Statistics curves of various control schemes (a) average value of dc-link current versus rotor speed, (b) RMS value of phase current versus rotor speed, and (c) peak value of phase current versus rotor speed..... 104



Chapter 1

Introduction

1.1 Research Background and Recent Development

With fast advance in technology, it is essential for the electronic products to be elaborated and sophisticated, and the internal functions are various and high speed. A common problem associated with modern electronic product is forced air cooling. The easiest way with low cost for forced air cooling is brushless dc (BLDC) fan motor installations. The phase windings of BLDC fan motor can be categorized as single-phase or three-phase, their flux distribution can be either sinusoidal or trapezoidal. The three-phase BLDC fan motors have the characteristics of high ratio of torque to weight, low noise, fast response, high efficiency and easy maintenance. However, it is an involved and costly process to fabricate the three-phase motor and it needs more requirements for six switches of inverter and three Hall sensors. For simple structure and requirement of single-phase BLDC fan motor, it's easy to employ to slim type application of consumer electronics. Moreover, due to the characteristics of wide speed range, small size, easy controllability, and long lifetime expectancy, single-phase BLDC motors are now the major choice for forced air cooling in PC, NB, and other information appliances.

With rapidly development of integrated circuit, the integration of control and drive ICs have been widely implemented in fan motors. Taking PCs for example, there are many inside devices such as power supply, CPU, and video graphic array (VGA) card, etc. Each device usually combines with single-phase BLDC fan motor and its drive IC. Based on International Data Corporation (IDC) research, the worldwide shipment of PC is over 150 million units in

2008. It tells that the small size single-phase BLDC fan motors have significant market potential, and development in motor drive IC will become a major trend. Many single-phase BLDC fan motor drive ICs have been commercialized such as LB11961 of Sanyo, BD6964FVM of Rohm, THMC45 of Texas Instruments, and APX 9262 of Anpec, etc. The functions of commercial drive IC list in Table 1.1. Among them, LB11961 has the feature of build-in variable speed function controlled by voltage of thermal resistor, that is, the fan motor speed is varied with environment temperature. The overall efficiency improvement is based on soft-commutation scheme to reduce the current spike at commutation boundary. The additional functions of rotor locked detection and auto-restart are used to protect the motor if the rotor is unexpected stop. These low cost and high performance drive ICs give the system host a new solution for air cooling.

TABLE 1.1
Functions of commercial drive IC

	Sanyo	Rohm	TI	Anpec	LSI	Melexis	UTC
Lock Detection & Auto-Restart	⊙	⊙	⊙	⊙	⊙	⊙	⊙
Lowest Speed Setting Pin	⊙						
PWM Control	⊙	⊙	⊙	⊙	⊙	⊙	⊙
Soft-Start	⊙	⊙					
Soft-Commutation PWM	⊙	⊙				⊙	⊙
Current Protection	⊙	⊙	⊙	⊙	⊙	⊙	⊙

Most commercial single-phase BLDC fan motor drive ICs utilize an open-loop voltage-mode control of hard-commutation scheme with full-bridge circuitry to realize variable speed control, and the commutation control is accomplished via a linear Hall sensor [1]-[3]. However, such method is disadvantageous for current spikes at commutation boundary, which will result in numbers of undesirable effects such as acoustic noise, reducing efficiency and

increasing power circuit rating. There are many methods to compensate for these effects. One method is by advancing the Hall sensor position so that commutation takes place before the current reach too high [4]. Nevertheless, it is inconvenient to modify Hall sensor position which is often installed on drive PCB. Another method called soft-commutation is employed to reduce the current spikes by modifying the switching patterns of inverter [5]-[6]. However, the overall efficiency is improved only for high speed. The above methods still can not remove the root problem of current spike at commutation boundary, so the overall efficiency will be seriously degraded in wide speed control applications.

The linear Hall sensor provides the information of rotor position and velocity via signal processing technique. However, there are some disadvantages such as additional installation of the sensor, signal conditioning circuit, sensitive to magnetic noises, and unsuitable for high temperature environment. To prevent the above problems, many sensorless techniques are presented to develop reliable and low cost control strategies for BLDCMs, which can be generally classified into two categories [7]. The first type is based on back-EMF sensing [8]-[10]. Since the back-EMF voltage is the function of the rotor position, the most common approach is to extract the rotor position from the unexcited phase. However, these methods are not suitable for single-phase BLDC fan motor because of no unexcited phase and low signal-to-noise ratio (SNR) of the measured signals at low speed operation. The second type is to derive the rotor position with a mathematic motor model by measuring the phase voltage and current. By using these quantities, the rotor position can be determined using a state observer, or a Kalman filtering technique, or by direct calculations [11]-[12]. These methods are computationally intensive, and large rotor position detection errors may occur because of quantization and truncation errors, and measurement inaccuracies. Besides, the estimation performance is affected with some motor parameters varying with thermal or operation conditions. It also suffers the low SNR of the measured signals at low-speed operations.

A common problem associated with the sensorless motor drive system is its starting performance. Using above sensorless algorithms, the measured signal is too small to make precise position estimation when motor is at standstill or low speed. The most common solution to the problem is the open-loop start-up method from a pre-determined rotor position [13]. The permanent magnet rotor will align to the direction corresponding to the induced magnetic field. With a known initial rotor position, an open loop control with ramp up frequency of injecting current is applied to speed up the motor from standstill. However, especially for the single-phase BLDC fan motor, it has only single phase winding, so the induced stator field is just two opposite directions. The motor may start to rotate in company with temporary reversing rotation or even unable to startup. Another starting method is the initial rotor position estimation which is based on the saturation effect of stator iron core due to the permanent magnet [14]. Reference [15] detects the initial rotor position by the time periods of discharge of stator windings, which are excited before discharge. Nevertheless, such methods have drawbacks being complicated or have to sense the current and voltage.

1.2 Research Motivation and Objectives

The research objectives of this thesis are in three-folds. The first one is to introduce a simple modeling method with feasible parameter identification to meet the characteristics of single-phase BLDC fan motors [16]-[20]. The constructed mathematical model of the highly nonlinear single-phase BLDC fan motor makes it easier for developing more sophisticated control schemes and analyzing the system performance. Simulation results can be verified with measurement results to confirm the validity of propose model.

The second objective of this research is to develop an efficiency optimization control scheme over the entire speed control range. This can be achieved by two aspects, one is choosing an appropriate PWM control strategy and another is increasing the utilization ratio

of driving current. To reduce the power losses in the inverter, the characteristics and the relative advantages and drawbacks of different PWM switching schemes are compared [21]-[23]. To increase the motor output power, this research adopts the closed-loop current-mode control for low and middle speed [24]-[27]; and switch to open-loop voltage-mode soft-commutation control for high speed operation. On the other hand, as the performance of digital signal processors has increased rapidly during last decade, the interest for digital motor control has grown. So, the digital current-loop controller design and consideration are also introduced [28]-[31].

The third objective of this research is the implementation of a low cost and high efficiency sensorless control for single-phase BLDC fan motor drives. The sensorless control scheme extends the soft-commutation method which will ensure the correct detection of the back-EMF zero-crossing point (ZCP) [32]-[35]. In order to promote the overall efficiency, the closed-loop current-mode control scheme is also applied to the sensorless control system. The current reference is produced by look-up table to estimate the linear Hall sensor. A specific sensorless start-up strategy is realized based on the feature of asymmetric air gap to ensure the motor running in predefined direction no matter where the initial rotor position is [36]-[38]. Then, an open-loop control called kick-off speed up the fan motor to middle-speed where sensorless control algorithm based on the back-EMF can work properly.

With the rapidly development of integrated circuit, digital motor control systems have been widely implemented with software based on microcontrollers or digital signal processors (DSPs). These approaches provide flexibility and are suitable for motor drive applications. The proposed control schemes have been implemented on a single-chip DSP controller (TMS320LF2407A) to verify the performance and feasibility for single-phase BLDC fan motors. Experimental verification has been carried out on a single-phase BLDC fan motor control system.

1.3 Thesis Organizations

The thesis is organized as follows. The simple modeling method with illustrated parameter identification and the basic operation principle for single-phase BLDC fan motors are proposed in Chapter 2. Simulation results can be verified with measurement results to confirm the validity of proposed model.

In Chapter 3, the design and realization of efficiency optimization control scheme for single-phase BLDC fan motors with linear Hall sensor is presented. This research adopts the advantages of closed-loop current-mode control scheme and soft-commutation control scheme to achieve efficiency optimization over entire speed control range. The overall efficiency can be compared by various control schemes based on calculation of RMS value and peak value of phase current. The detailed description will be discussed in this chapter.

In Chapter 4, a low cost and high efficiency sensorless control system for single-phase BLDC fan motors is implemented. Using the ZCP detection of back-EMF, the driving current can be commutated without Hall sensor. Besides, due to the feature of asymmetric air gap, a specific starting strategy is employed to start-up the fan motor from standstill to full speed. The detailed description of the sensorless technique, starting procedure and simulation results of system response will be discussed in this chapter.

In Chapter 5, the laboratory setup of the single-phase BLDC fan motor control system with or without Hall sensor is introduced, and the DSP-based software implementation issues are discussed. The overall performance of the proposed control schemes are verified through extensive real-time experimental results. Some concluding remarks and suggested future works related to this research are summarized and discussed in Chapter 6.

Chapter 2

Basic Operation of Single-Phase BLDC Fan Motors

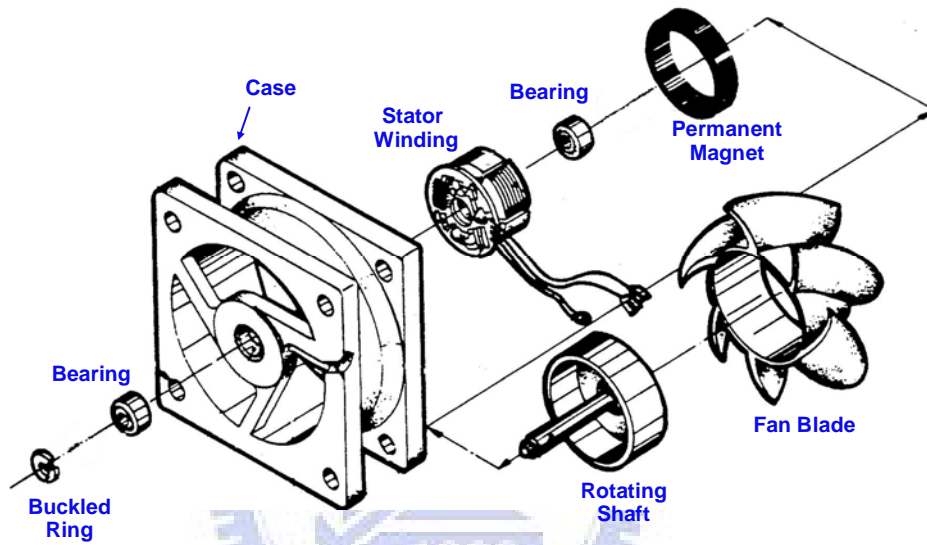
2.1 STRUCTURE OF SINGLE-PHASE BLDC FAN MOTORS

Among the numerous types of fan motors, single-phase BLDC motors are now the major choice for forced air cooling applications. Fig. 2.1(a) is the configuration of single-phase BLDC fan motor which is usually an additive device for CPU or power supply to keep from overheating. Fig. 2.1(b) is an exploded perspective view of fan motor and it can be seen that the fan motor comprises a fan case which is provided to cover the fan blades, the container which supports the rotating shaft of the fan, and ball bearings which are inserted into the motor body. Moreover, the magnetic part covers the fan blades from outside and an annular permanent magnet inserts into the inner border.

The distinctive feature of the single-phase BLDC motor is the asymmetric air gap to eliminate dead point. If dead point, where the developed torque value is zero, exists in single-phase BLDC motors, there is a possibility that the motor will stop at the dead-point and be unable to start. Fig. 2.2 shows the cross-sectional view of stator and rotor assembly with asymmetric air gap. A four poles and external-rotor type of single-phase BLDC fan motor is used in this paper. The fan motor is wound with a single coil and the winding terminals are connected to an inverter which is switched at a frequency corresponding to rotor velocity.



(a)



(b)

Fig. 2.1. Structure of the single-phase BLDC fan motor (a) real motor configuration and (b) exploded perspective view.

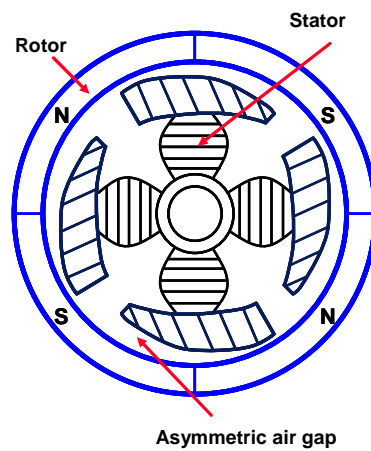


Fig. 2.2. Cross-sectional view of stator and rotor assembly with asymmetric air gap.

The electronic commutation for a single-phase BLDC fan motor is accomplished by controlling the inverter to excite the corresponding current. Since the torque production performance largely depends on the phase relationship between excitation current and back-EMF, a reliable and accurate rotor position sensing device is required. The rotor position sensing can be achieved by the use of Hall sensors for low-cost applications, or by resolvers and optical encoders for high-performance applications. In practice, Hall sensors are the most widely used for electronic commutation of BLDCM drives. The operational principle of Hall sensor is shown in Fig. 2.3. When a magnetic field is applied to a semiconductor carrying with a constant current I_H , a voltage which is proportional to the applied magnetic field will be generated. The directions of the applied magnetic field, the current flowing, and the Hall voltage are perpendicular. In general, Hall sensors have a number of advantages, including the capability of operating at frequencies in excess of 100 kHz, high reliability, and low cost. However, Hall-effect sensors are sensitive to the temperature due to their physical characteristics, and can not be used at high-temperature conditions.

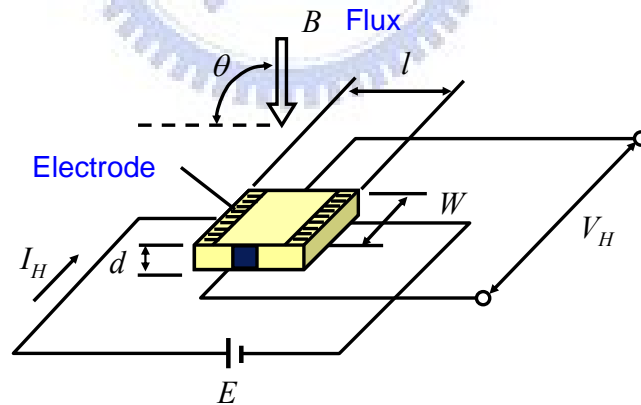


Fig. 2.3. Operational principle of Hall sensor.

2.2 MATHEMATICAL MODELING

The BLDCMs, along with an appropriate power converter and either speed or position feedback, have become popular in many sophisticated control applications. The proper design and compensation of such system requires an accurate mathematical model with all of the components of the system. This research proposes a simple modeling method to meet the characteristics of single-phase BLDC fan motor, and to investigate both static and dynamic relationship between the driving circuit and the real motor [16]-[19]. By way of proposed model, it will assist designers to analyze the system performance and make the design work more practical.

Fig. 2.4 shows the schematic of the full-bridge inverter and equivalent modeling for a single-phase BLDC fan motor. The stator winding can be modeled as a winding resistance in series with a winding inductance and a back-EMF voltage. The voltage equation describing the dynamic behavior of single-phase BLDC fan motor is given as follow

$$v = L_s \frac{di}{dt} + iR_s + v_{emf} \quad (2-1)$$

where v and i are the phase voltage and phase current, respectively. R_s and L_s are the winding resistance and the winding inductance, respectively. v_{emf} is the back-EMF voltage induced by rotor flux variation and the value is proportional to motor speed.

$$v_{emf} = K_E \cdot \omega_r \quad (2-2)$$

where ω_r is the rotor velocity and K_E is the back-EMF constant which is associated with the form of nonlinear flux distribution in this application. So, equation (2-2) can be revised as

$$v_{emf} = K \cdot \phi_f(\theta_e) \cdot \omega_r \quad (2-3)$$

where K is constant and ϕ_f is the normalized value of flux distribution which is varied with rotor position θ_e .

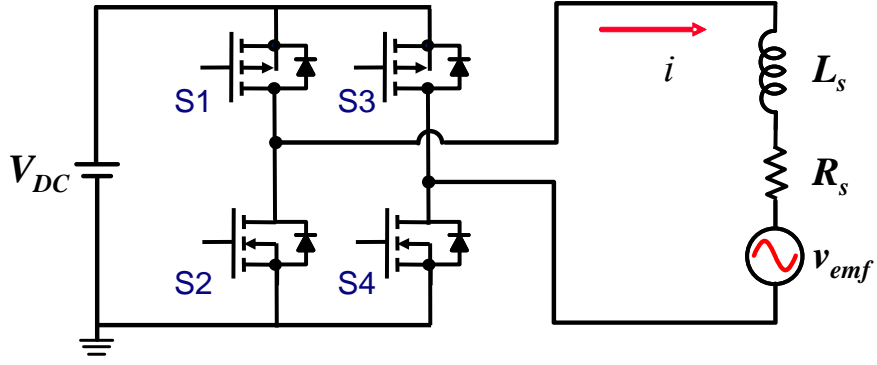


Fig. 2.4. Schematic of the full-bridge inverter and equivalent modeling for a single-phase BLDC fan motor.

The energy transforms from electrical system to mechanical system can be expressed as

$$T_e = K_T \cdot i \quad (2-4)$$

where K_T is the torque constant and is equivalent to the back-EMF constant K_E . As mention before, K_T and K_E are function of rotor position due to the flux distribution. However, for single-phase BLDC fan motor, it's inadequate to represent the nonlinear flux distribution with simple equation. For this reason, building up the table in term of flux distribution is necessary to confirm accuracy of the equivalent model.

For the mechanical system, the developed torque must overcome the inertial acceleration torque, friction torque and the load torque. Therefore, the torque-speed characteristics can be formulated as

$$T_e = J_m \frac{d\omega_r}{dt} + B_m \omega_r + T_L \quad (2-5)$$

where the inertial acceleration torque is represented by the product of the moment of inertia J_m and the angular acceleration $d\omega_r/dt$. The load torque referred to the motor shaft and fan blade, while the friction torque is the product of the rotor velocity and viscous friction coefficient B_m .

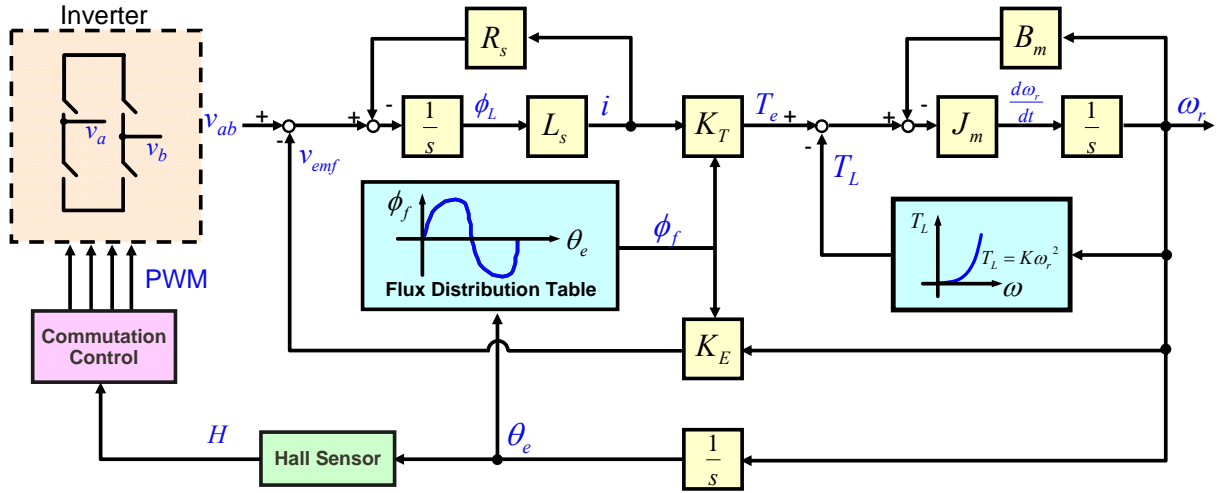


Fig. 2.5. Block diagram for modeling of the single-phase BLDC fan motor.

According to previous equations, the modeling of the single-phase BLDC fan motor can be represented by a block diagram as shown in Fig. 2.5. The motor is fed with a high frequency PWM voltage by a voltage-source full-bridge PWM inverter. The corresponding output voltage is applied to the motor winding, and then the electromagnetic torque is produced to rotate the fan motor. It should be noted that the value of K_E and K_T is obtained from flux distribution table depending on rotor position which is derived by integration of rotor velocity. The output signal of the linear Hall sensor is proportional to rotor flux density and is also characterized by a rotor flux distribution table.

2.3 PARAMETER IDENTIFICATION

2.3.1 Electrical Parameters

After the mathematical modeling of the single-phase BLDC fan motor is constructed, the precise parameter identification will improve the consistence to a real motor. Because of single coil, the electrical parameter identification includes winding resistance R_s , winding inductance L_s and back-EMF constant K_E . The resistance and inductance determine the electrical time constant for dynamic current response. The back-EMF constant is associated with developed torque and speed range of motor.

Usually, the resistance and inductance can be measured by R - L - C meter. However, there is another method which injects a step voltage into the stator winding and observes the current response to extract the parameters. Under this condition, the fan motor should be keep standstill to avoid the interference of the back-EMF voltage, and then the phase winding terminal is injected a step voltage

$$v(t) = V \cdot u_s(t - t_0). \quad (2-6)$$

Fig. 2.6 shows the current response which is similar to a first-order R - L series circuit,

$$i(t) = \frac{V}{R_s} (1 - e^{-\frac{R_s}{L_s}(t-t_0)}) \cdot u_s(t - t_0) \quad (2-7)$$

$$i_{ss} = \frac{V}{R_s} \quad (2-8)$$

$$\tau = \frac{L_s}{R_s}. \quad (2-9)$$

From (2-8) and (2-9), the series resistance R_s can be determined by steady state current i_{ss} , and the series inductance L_s can be determined by time constant τ and transient time $t_{ss}-t_0$.

Based on (2-2) and (2-3), the back-EMF constant K_E is the amplitude of back-EMF voltage per rotation speed, and it can be obtained from sensing back-EMF voltage and rotor velocity. The back-EMF voltage can be measured by forcing the motor to run at high speed and then release the motor to free running. The measured terminal voltage can be used for the identification of back-EMF constant as well as the table of rotor flux distribution which is shown in Fig. 2.7.

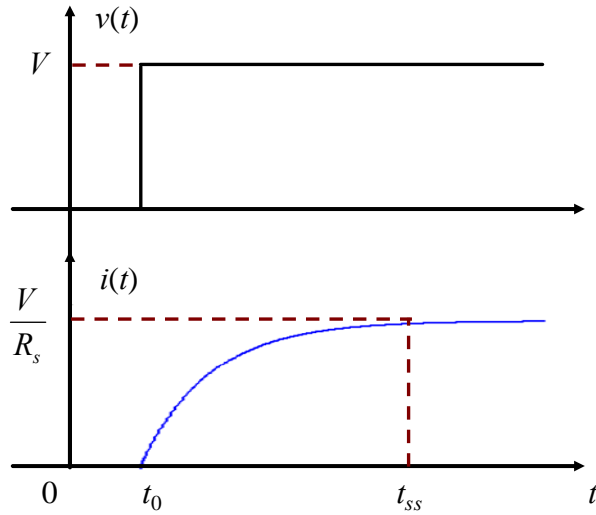


Fig. 2.6. Step voltage input and current response.

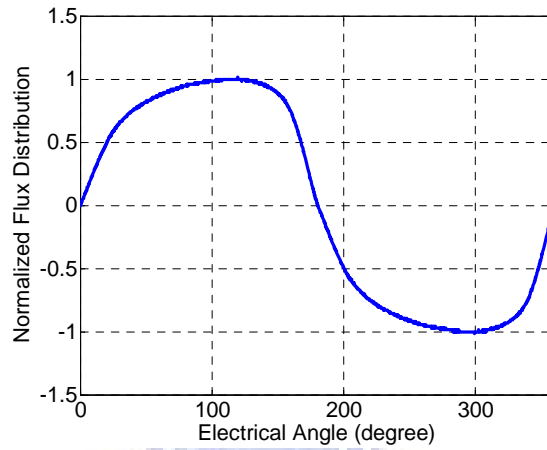


Fig. 2.7. The table of normalized flux distribution versus rotor position.

2.3.2 Mechanical Parameters

The interaction of stator field with the rotor field creates an electromagnetic torque. According to (2-4) and (2-5), the fan motor speed response is directly related to mechanical parameter. When fan motor rotates at stable speed, i.e., $d\omega_r/dt$ is zero, then (2-5) can be revised to

$$K_T \cdot i = B_m \omega_r + T_L. \quad (2-10)$$

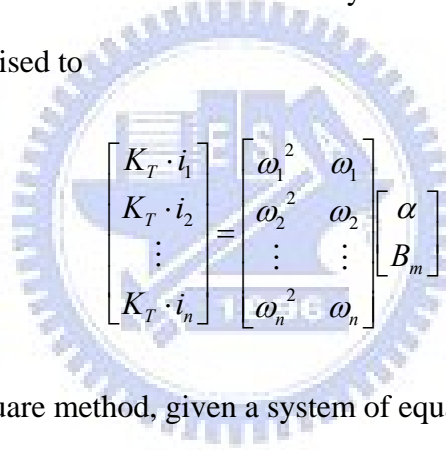
Due to mechanical structure of fan motor, the load torque is proportional to the square of fan motor speed, i.e.,

$$T_L = \alpha \cdot \omega_r^2 \quad (2-11)$$

where α is constant which is related to mechanical structure of fan motor. Therefore, the torque-speed function at stable speed becomes

$$K_T \cdot i = B_m \omega_r + \alpha \omega_r^2. \quad (2-12)$$

The least square method is used to derive the viscous coefficient B_m and constant α . It assumes that the best-fit curve of a given type which has the minimal sum of the square error from a given set of data. With different rotor velocity and corresponding RMS value of phase current, (2-12) can be revised to



$$\begin{bmatrix} K_T \cdot i_1 \\ K_T \cdot i_2 \\ \vdots \\ K_T \cdot i_n \end{bmatrix} = \begin{bmatrix} \omega_1^2 & \omega_1 \\ \omega_2^2 & \omega_2 \\ \vdots & \vdots \\ \omega_n^2 & \omega_n \end{bmatrix} \begin{bmatrix} \alpha \\ B_m \end{bmatrix}. \quad (2-13)$$

According to the least square method, given a system of equations

$$A\mathbf{x} = \mathbf{b} \quad (2-14)$$

where

$$A = \begin{bmatrix} \omega_1^2 & \omega_1 \\ \omega_2^2 & \omega_2 \\ \vdots & \vdots \\ \omega_n^2 & \omega_n \end{bmatrix}, \quad \mathbf{b} = \begin{bmatrix} K_T \cdot i_1 \\ K_T \cdot i_2 \\ \vdots \\ K_T \cdot i_n \end{bmatrix}, \quad \mathbf{x} = \begin{bmatrix} \alpha \\ B_m \end{bmatrix}. \quad (2-15)$$

It cannot expect in general to find a vector \mathbf{x} for which $A\mathbf{x}$ equals \mathbf{b} . Instead, it can look for a vector $\hat{\mathbf{x}}$ for which $A\hat{\mathbf{x}}$ is closet to \mathbf{b} . So, there is a unique solution

$$\hat{\mathbf{x}} = (A^T A)^{-1} A^T \mathbf{b} \quad (2-16)$$

, that is, $\hat{\mathbf{x}}$ satisfies the minimal sum of square error. Therefore, the viscous coefficient B_m and constant α can be obtained by (2-16).

Eventually, the remainder is the moment inertia of the fan motor. During the fan motor accelerates from stop to rotate as shown in Fig. 2.8, the rotor velocity can be calculated by linear Hall sensor, and the acceleration $d\omega_r/dt$ can also be approximately estimated. Based on (2-5) and along with viscous coefficient B_m and constant α , the moment inertia of fan motor can be derived. Following the above parameter identification methods, the single-phase BLDC fan motor's parameters list in Table 2.1.

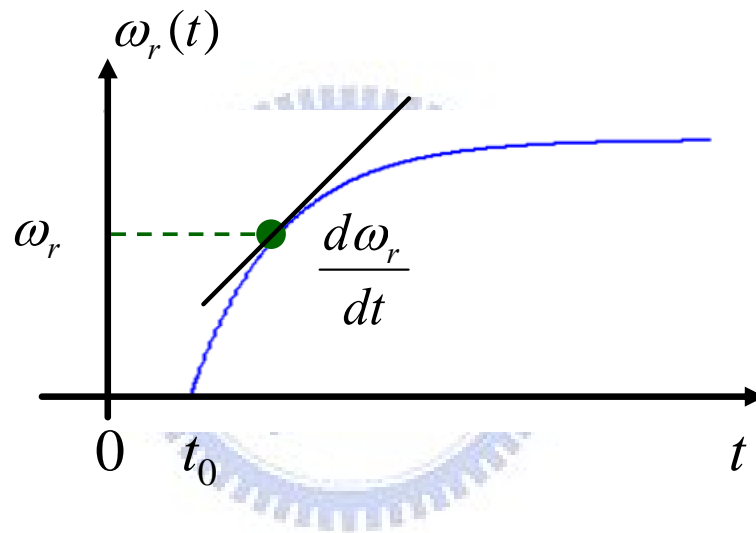


Fig. 2.8. Speed response from stop to rotate.

TABLE 2.1
Parameters of the tested motor

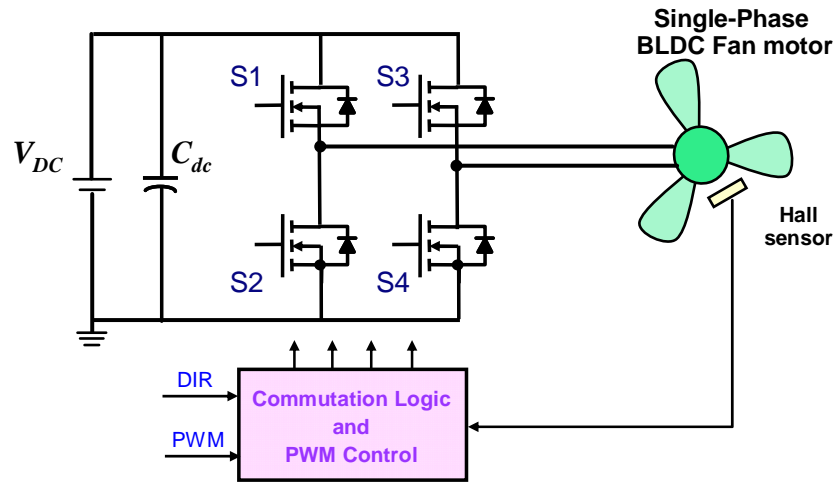
Single-phase brushless dc fan motor	
Type	4 poles
Rated voltage	12 V
Stator resistance	9.3 Ω
Stator inductance	5.6 mH
Back-EMF constant	1.82 mV/rpm
Rotor inertia	$1.6 \times 10^{-6} \text{ kg} \cdot \text{m}^2$
Viscous coefficient	$1.3 \times 10^{-6} \text{ N} \cdot \text{m} \cdot \text{s/rad}$

2.4 A STUDY OF DYNAMIC BEHAVIOR

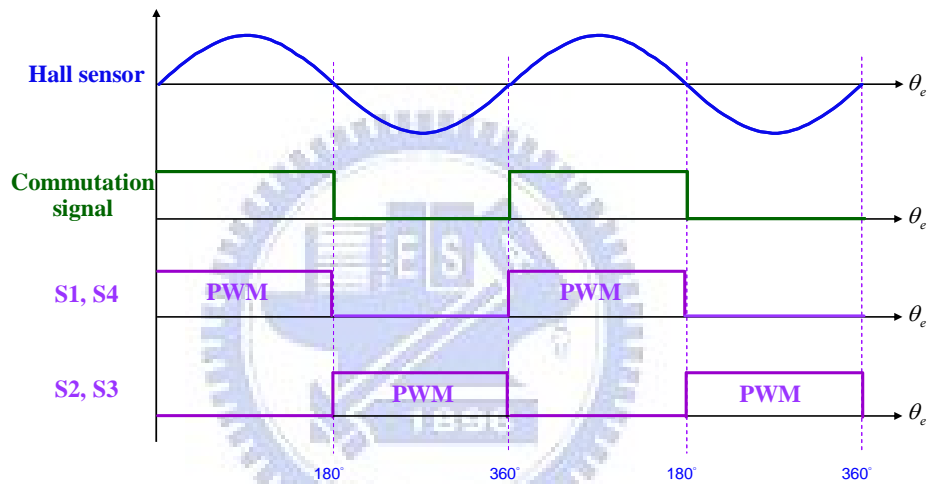
2.4.1 Basic Operation Principle

Due to the flux distribution varies with rotor positions, the magnetic field produced from stator winding should synchronize with rotor field. Fig. 2.9(a) shows the schematic of the commutation control circuit for the single-phase BLDC fan motor with Hall sensor feedback [1]-[3]. The full-bridge inverter consists of four switches S1 to S4 which were controlled to supply required direction of driving current. Each switch connects with anti-parallel diode to remain driving current during the current commutation. Each winding terminal is connected to a pair of switches as shown. When both switches in the same phase are on, the bus voltage is short circuit. This condition should be inhibited at all times. To eliminate short circuit during switching transients, a small dead-time is introduced in between turn-off of one switch and turn-on of the other switch in the same phase.

A linear Hall sensor is fixed to a on drive PCB of the single-phase motor, and biased by a constant voltage. The linear Hall sensor produces an output signal which is proportional to the intensity of the induced rotor field, so it is used to provide rotor position and velocity feedback information via signal processing technique. Fig. 2.9(b) shows the operation waveform based on open-loop voltage-mode control of hard-commutation scheme. The control system accepts the Hall sensor feedback and determines the switching status to commutate the phase current. The phase winding will be conducted 180 electrical degrees for both positive and negative driving current. When the Hall sensor waveform goes through zero from negative to positive transistors S1 and S4 are switched ON and switches S2 and S3 are switched OFF, while when the Hall sensor waveform goes through zero from positive to negative switches S2 and S3 are switched ON and switches S1 and S4 are switched OFF. In other words, transistors S1, S4 and the transistors S2, S3 are complementarily turned ON/OFF to change the directions of the driving current whereby the single-phase motor is revolved.



(a)



(b)

Fig. 2.9. The open-loop voltage-mode control of hard-commutation scheme (a) the schematic of commutation control circuit and (b) operation waveform.

2.4.2 Analyses of Steady-State Response

Fig. 2.10 is the steady-state current response when using open-loop voltage-mode of hard-commutation scheme. There is a significant current spike at commutation boundary. The dynamic behavior of current response is given as follow

$$i(t) = \frac{v - v_{emf}}{R_s} (1 - e^{-\frac{R_s t}{L_s}}) \quad (2-17)$$

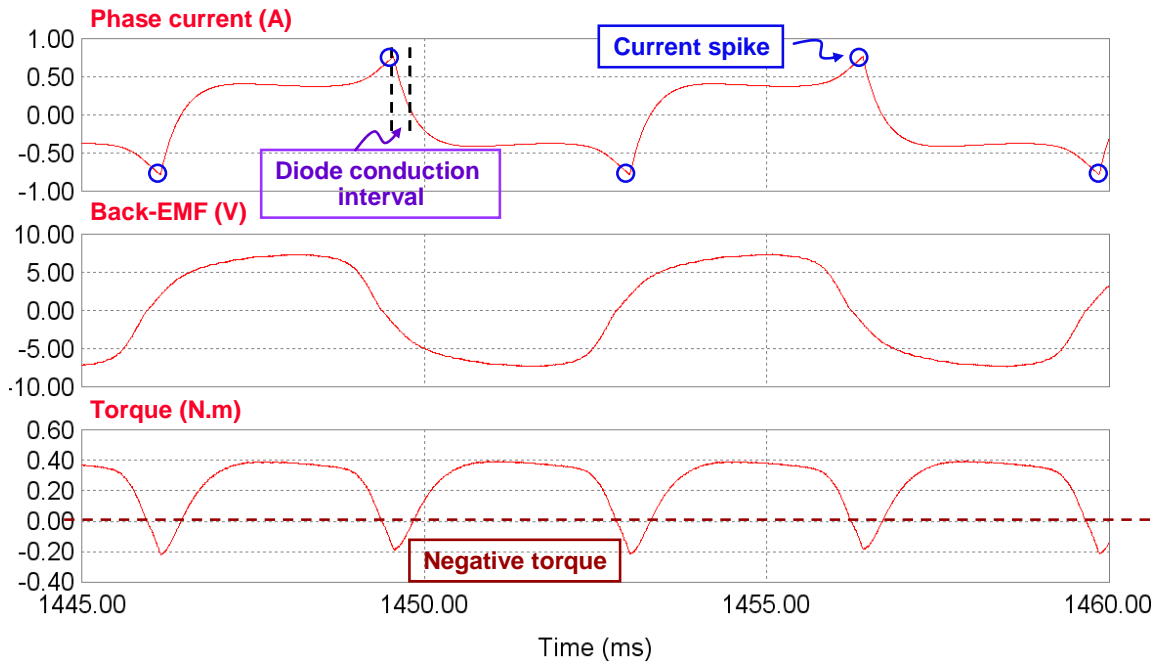


Fig. 2.10. Steady-state current response when using open-loop voltage-mode control of hard-commutation scheme.

where v is the input voltage of phase winding, R_s and L_s are the series resistance and the series inductance of stator winding, respectively. v_{emf} is the back-EMF induced by rotor flux variation. Owing to the back-EMF seriously drops at commutation boundary, and it results in a great rising slope of current response, that is the current spike. Moreover, due to the winding inductance, the polarity of the phase current cannot be changed instantaneously, so the current will pass through the anti-parallel diode and decrease to zero at commutation boundary. It results in the driving current out of phase with back-EMF and a negative torque is generated, and consequently the overall efficiency is seriously degraded in wide speed control applications for single-phase BLDC fan motors.

Because of non-linear flux distribution, there are obvious torque ripples during motor revolution [20]. This will result in undesirable effects such as speed ripple and acoustic noise. As commonly known, it is better to achieve constant torque for smooth revolution, which requires very high current to compensate the weak magnetic field at commutation boundary. However, such high current will reduce the overall efficiency and increase the power circuit

rating. Fig. 2.11 shows the steady-state torque response at 4000 RPM. From (2-4) and (2-5), the developed torque can be revised as

$$T_{av} + \Delta T_e = J_m \frac{d\omega_r}{dt} + B_m \omega_r + T_L \quad (2-18)$$

where T_{av} is the average torque and ΔT_e is the torque ripple. So, the corresponding speed ripple can be calculated by

$$\Delta \omega_r = \frac{\Delta T_e \cdot \Delta t}{J_m} \quad (2-19)$$

From (2-19), the speed ripple is proportional to the torque ripple which is related to the flux distribution and phase current waveform. For the same model of single-phase BLDC fan motor, a suitable current shaping will reduce the torque ripple as well as speed ripple.

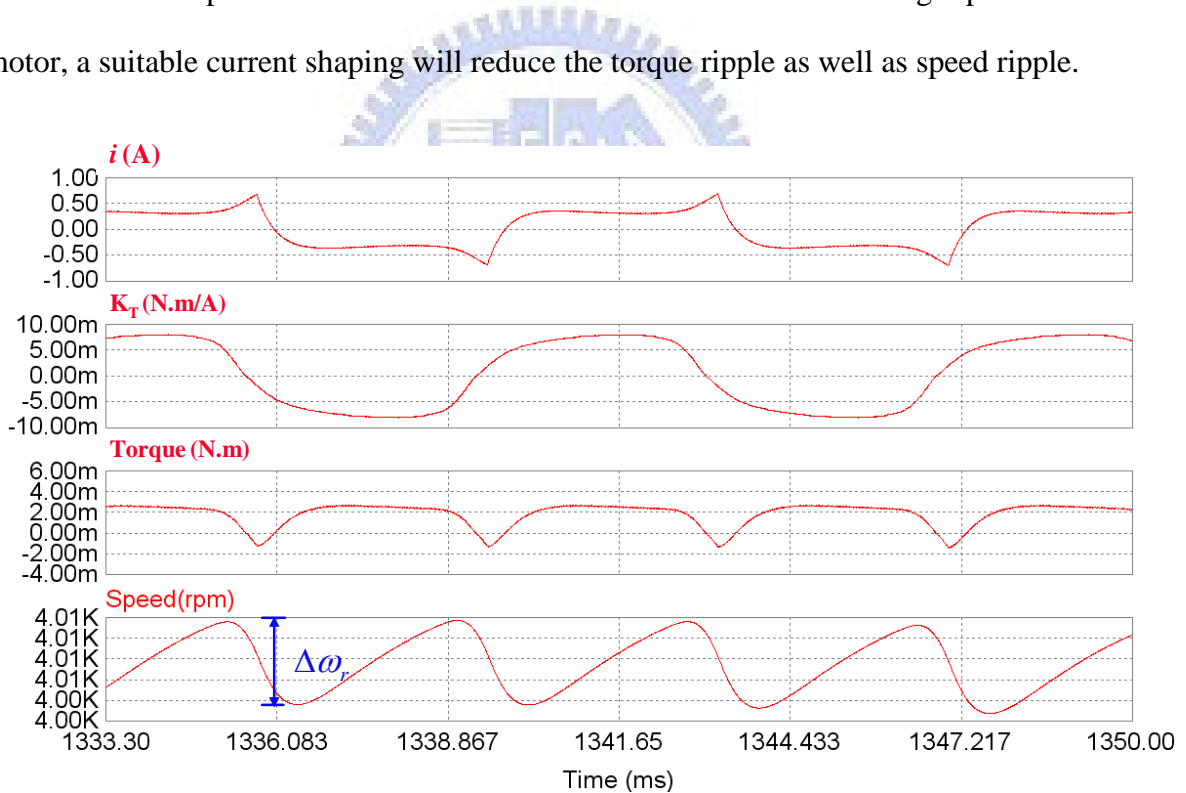


Fig. 2.11. Steady-state torque response when using open-loop voltage-mode control of hard-commutation scheme.

On the other hand, the ideal voltage sources V_{DC} at the input usually accompany with a suitable sized capacitor. The capacitor normally large enough to store a considerable amount of energy and their purpose is to deliver it to the load, rapidly enough not to cause the circulation of high-frequency currents through the primary source. Fig. 2.12 shows the equivalent model of dc-bus circuit. The current i_{dcm} passes through the inverter to the motor winding, so there exists high-frequency current due to current commutation.

When the motor is operated at predefined speed, the corresponding current i_{dcm} is served as independence current source which can be expressed as

$$i_{dcm} = i_{dcr} + i_{cap} \quad (2-20)$$

where i_{dcr} is the average current and i_{cap} is current ripple which is composed of twice angular frequency and switching frequency of current ripple. Because the operation speed and required input power have been determined, the average current will be derived as

$$i_{dcr} = \frac{P_{in}}{V_{DC}} \quad (2-21)$$

where P_{in} is the required input power at operation speed and V_{DC} is dc-link voltage source. The average current will pass through the dc-link voltage source, so the equivalent circuit is a resistor R_{dc} which can be given as

$$R_{dc} = \frac{V_{DC}}{i_{dcr}} \quad (2-22)$$

After properly modeling of dc-bus circuit, the transfer function from i_{dcr} to i_{dcm} can be expressed as

$$\frac{I_{dcr}(s)}{I_{dcm}(s)} = \frac{1}{s \cdot C_{dc} \cdot R_{dc} + 1} \quad (2-23)$$

which is a typical first-order low-pass filter. Therefore, the addition of capacitor will filter the

high-frequency current i_{dcm} . In order to reduce the twice angular frequency of current ripple, the bandwidth of low-pass filter should be low enough which will require a very large dc-link capacitor. Fig. 2.13 shows the simulation results of above discussion. If the capacitor is large enough to absorb the high-frequency current i_{cap} , the current i_{dcm} will be filtered to an average value i_{dcr} which is convenient to calculate the input power of motor drives.

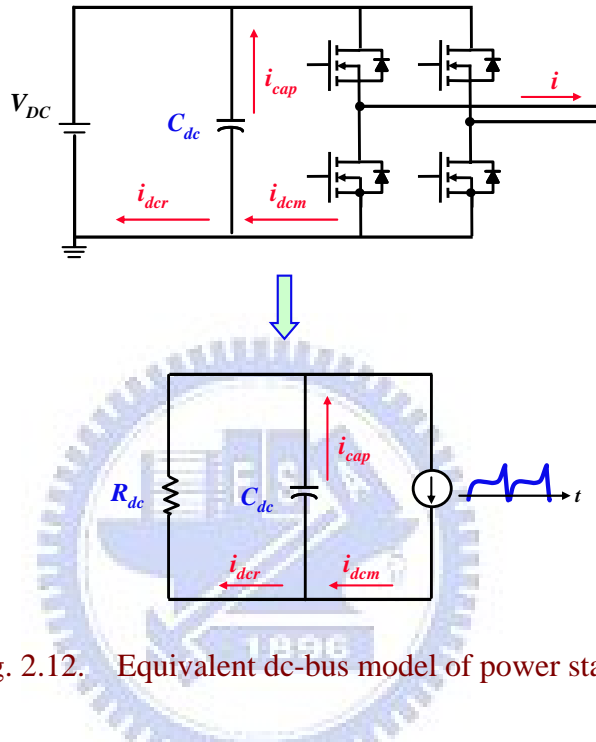


Fig. 2.12. Equivalent dc-bus model of power stage.

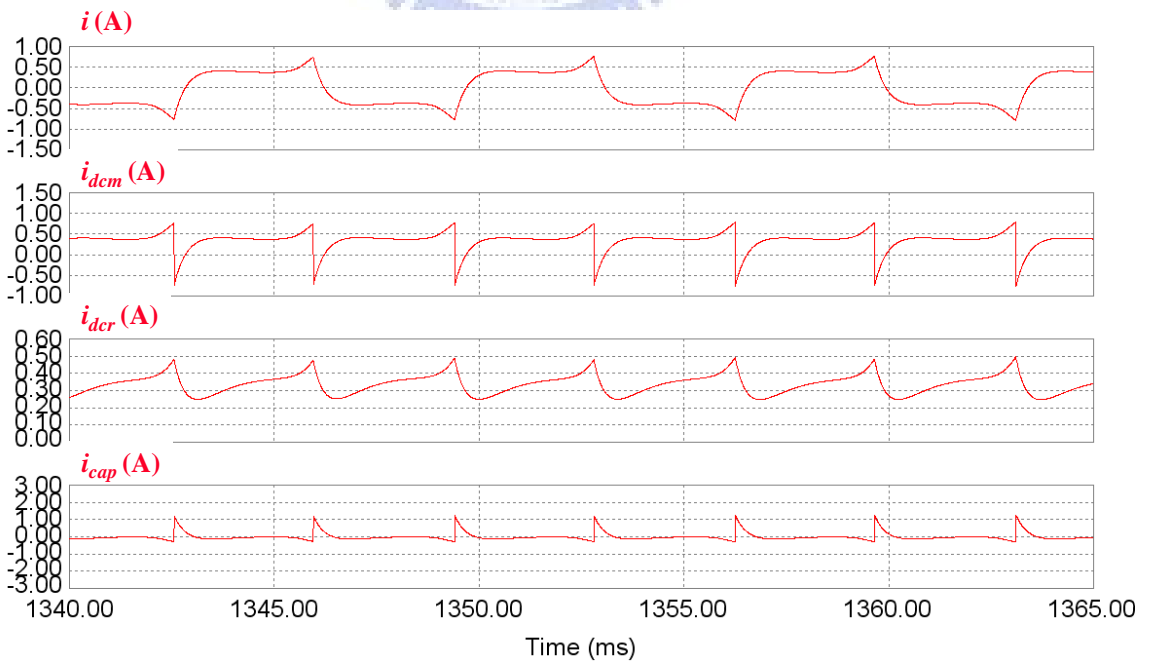
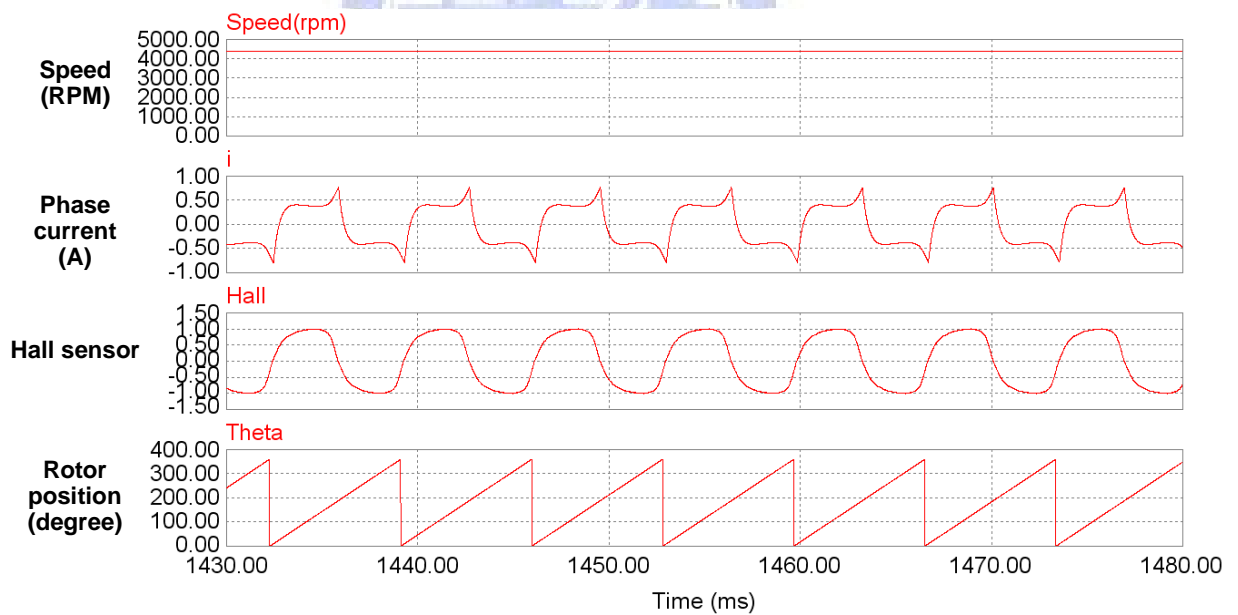


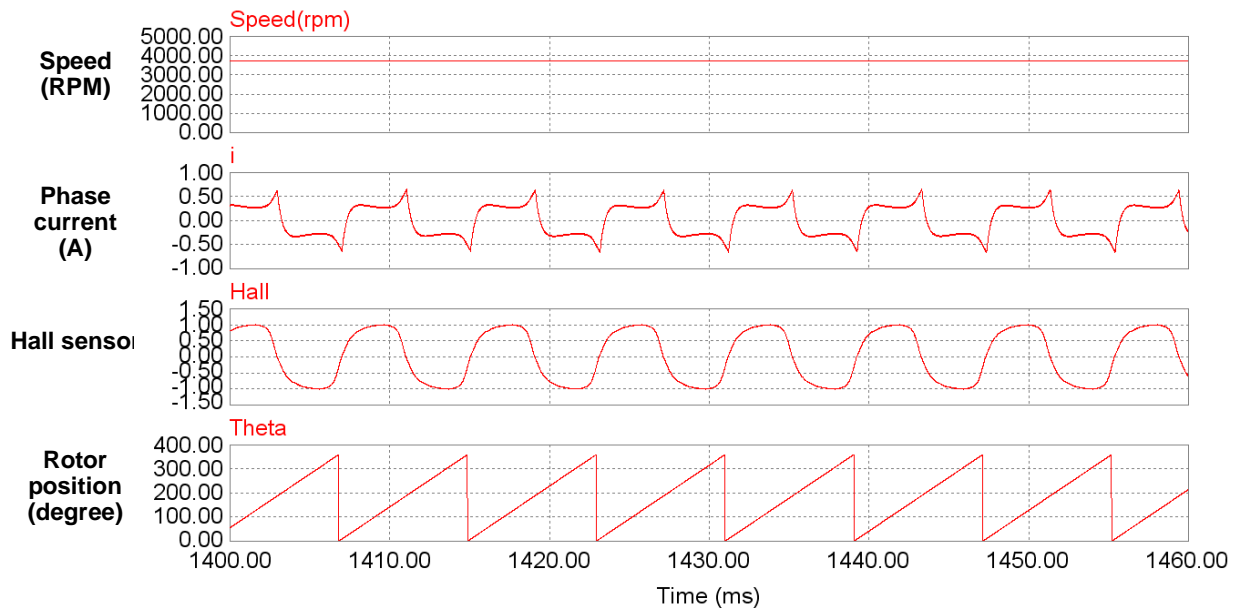
Fig. 2.13. Steady-state response of dc-bus current.

2.4.3 Verification of Proposed Model

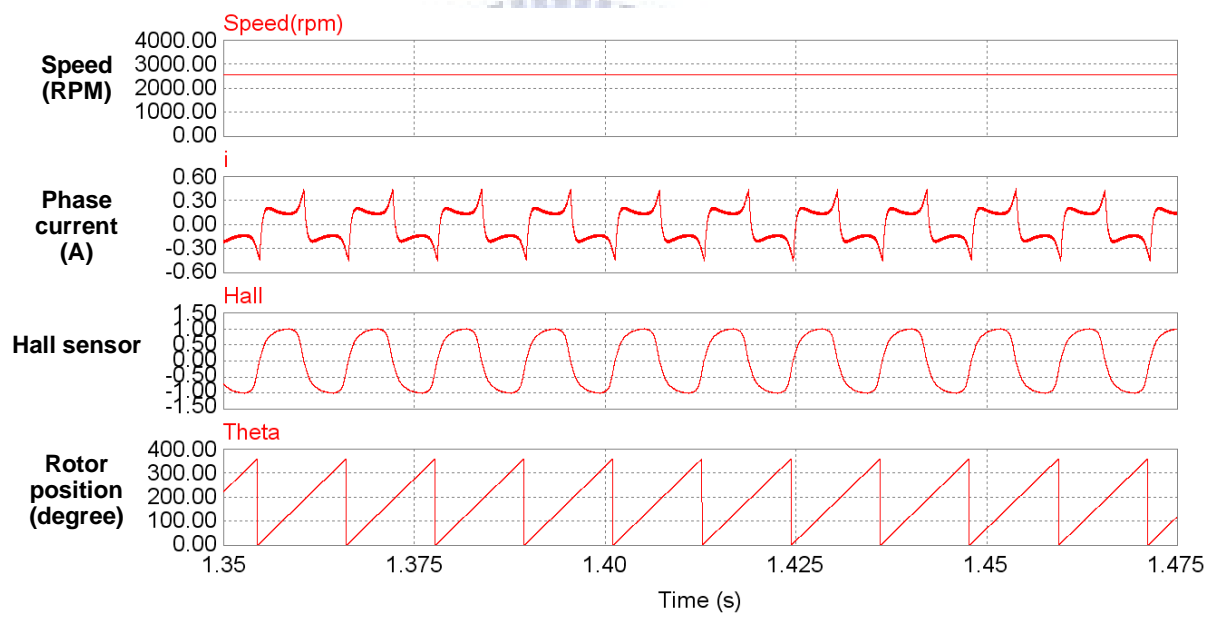
According to previous description, a simple modeling method with an illustrated parameter identification scheme for single-phase BLDC fan motor has been proposed. The parameters of Table I substitute the proposed model and verify with a real single-phase BLDC fan motor by computer simulation and experiment measurement. Using the open-loop voltage-mode of hard-commutation scheme, Fig. 2.14 shows the simulation results of steady-state response under duty ratio 100 %, 80 %, and 50 %, respectively. Fig. 2.15 shows the consistency of the proposed model and the real fan motor, it can be seen that simulation results are close to experiment measurements under different duty ratio. Fig. 2.16 shows the RMS value of phase current and rotor speed curves under different duty ratio, the simulation result is also close to experiment measurement. That is, above of all confirm the validity of the proposed model.



(a)

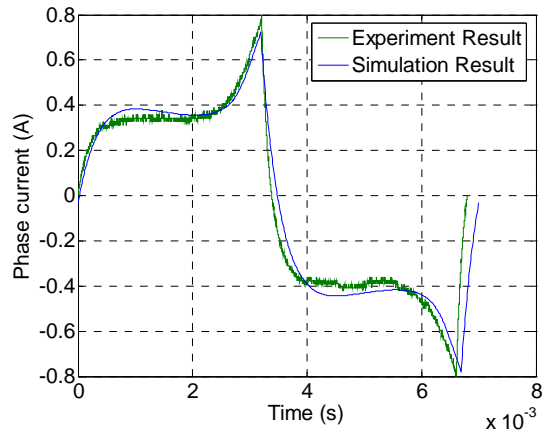


(b)

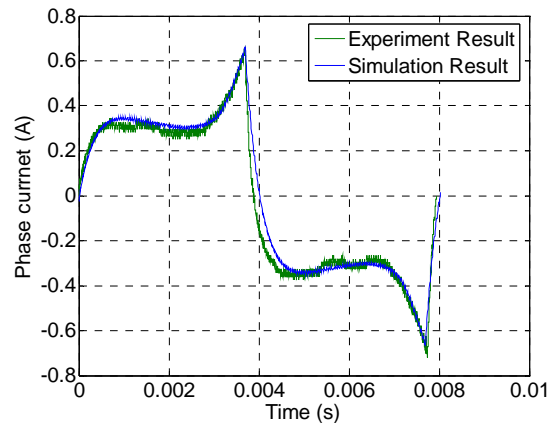


(c)

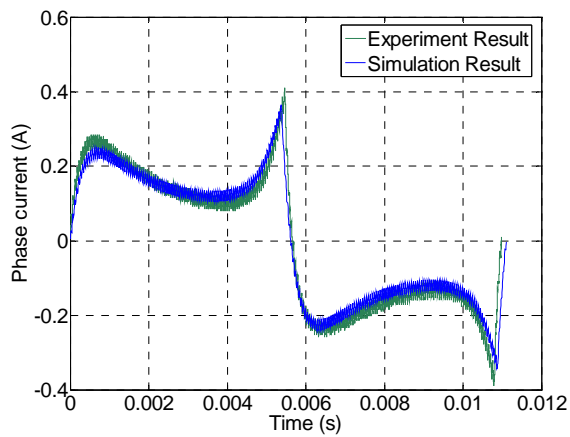
Fig. 2.14. Simulation result with open-loop voltage-mode control of hard-commutation scheme under (a) duty = 100 %, (b) duty = 80 %, and (c) duty = 50 %.



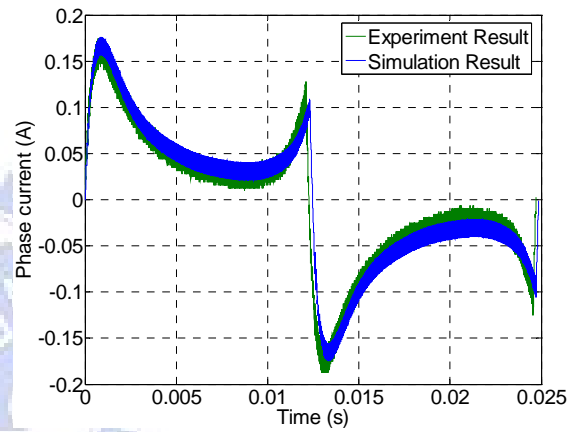
(a)



(b)

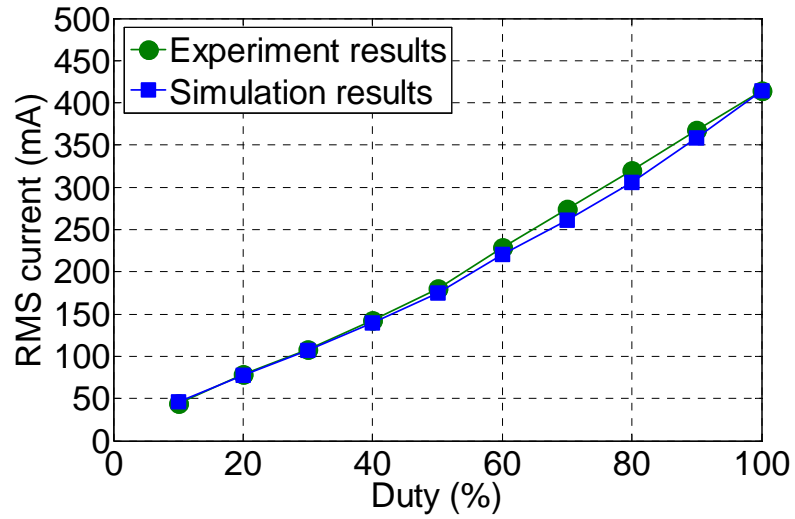


(c)

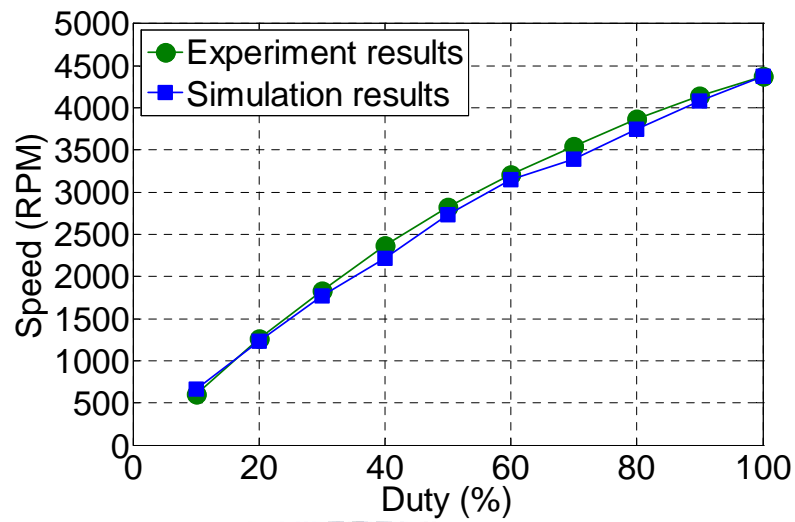


(d)

Fig. 2.15. Phase current comparison between simulation result and experiment measurement (a) duty = 100 %, (b) duty = 80 %, (c) duty = 50 %, and (d) duty = 20 %.



(a)



(b)

Fig. 2.16. The RMS value of phase current and rotor speed curves under different duty ratios.

Chapter 3

Efficiency Optimization of Single-Phase BLDC Fan Motor Drives

From previous discussion, it has been found that due to the high operation speed and high winding inductance, the phase current and back-EMF is out of phase if open-loop voltage-mode control of hard-commutation scheme is used. Consequently, a negative torque component is generated and there is the current spike at commutation boundary. Such current spike will bring about acoustic noise, reducing efficiency and increasing power circuit rating. For these reasons, the efficiency optimization control scheme over entire speed control range is presented in this chapter.

3.1 PWM CONTROL STRATEGIES

The overall efficiency can be improved from two aspects. One is choosing an appropriate PWM control strategy to reduce the power losses in the inverter. And another is increasing the utilization ratio of phase current as well as motor output power. Based on the motor parameters and application requirements, there are four different switching schemes [21], which encompass most of the currently available techniques, will be introduced for application of single-phase BLDC fan motors. The characteristics and the relative advantages and drawbacks of each scheme are also compared.

3.1.1 PWM Switching Scheme 1

The switch configuration of motor drives is shown in Fig. 3.1. In single-phase BLDC fan motors, the switching state during a PWM period takes only one of the following four possible states: driving, short to high, short to low, and regeneration. In this scheme, positive voltage is applied by permanently turning on S4 while S1 will be pulse-width modulating as shown in Fig. 3.2. When both S1 and S4 are driving states, phase current is increasing. Motor current during the PWM off period passes through an anti-parallel diode of S2 and the conducting transistor S4 (short to low state). In this example, only high side switches are modulated. A similar result will occur when only low side switches are modulated.

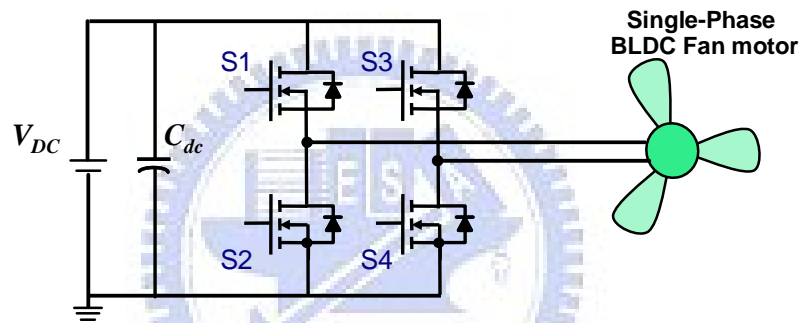


Fig. 3.1. Switch configuration of motor drives.

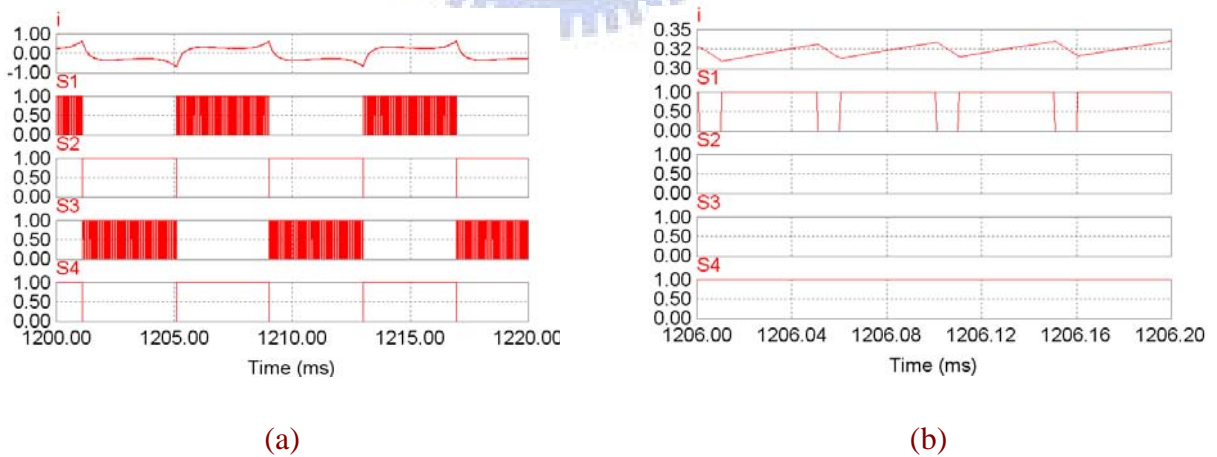


Fig. 3.2. (a) PWM switching scheme 1 and (b) macro view of switching pattern.

In order to optimize the overall efficiency, the power losses should be accurately calculated and compared the results of different PWM control strategies [23]. Losses are separated into transistor losses and diode losses in the inverter. Loss calculations are function of the circuit waveform. Thus, prior to the development of individual loss expressions, the steady-state waveform under operation condition must be determined. This paper uses the full-bridge inverter with constant switching frequency and constant dc-link input voltage, and the motor control is operated at 3000 RPM based on hard-commutation scheme.

For purpose of calculating the transistor losses, it is convenient to divide into conduction losses and switching losses. Fig. 3.3 shows the model of transistor's characteristic. During the interval in which the transistor is conducting, the characteristic is approximated with a resistance. For transistor S2 and S4, the conducting current is shown in Fig. 3.4, so the conduction losses over an electrical cycle can be expressed as

$$\begin{aligned}
 P_{S2,con} &= P_{S4,con} \\
 &= \frac{1}{2T_{com}} \int_0^{T_{com}} i_{S4}^2(t) \cdot R_{DS} \cdot dt
 \end{aligned} \tag{3-1}$$

where T_{com} is commutation cycle and R_{DS} is conducting resistance of transistor. Due to

$$\frac{1}{T_{com}} \int_0^{T_{com}} i_{S4}^2(t) \cdot dt = I_{rms}^2 \tag{3-2}$$

equation (3-1) can be revised to

$$\begin{aligned}
 P_{S2,con} &= P_{S4,con} \\
 &= \frac{1}{2} \cdot R_{DS} \cdot I_{rms}^2
 \end{aligned} \tag{3-3}$$

where I_{rms} is the RMS value of phase current. From (3-3), the conduction loss increases with conducting resistance of transistors.

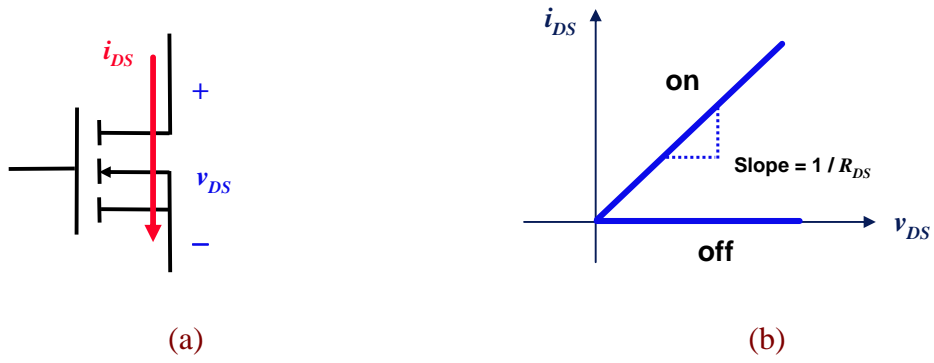


Fig. 3.3. Model of transistor's characteristic.

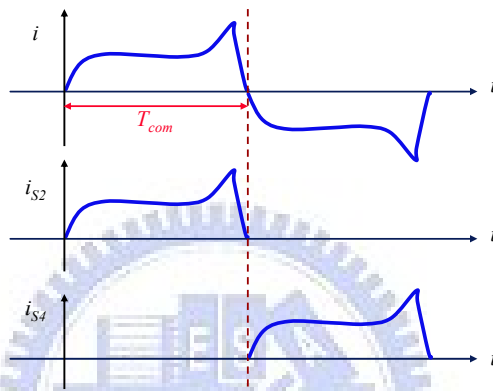


Fig. 3.4. Conducting current of transistor S2 and S4.

For transistor S1 and S3, the conduction losses over an electrical cycle can be expressed as

$$\begin{aligned}
 P_{S1,con} &= P_{S3,con} \\
 &= \frac{1}{2T_{com}} \int_0^{T_{com}} i_{S3}^2(t) \cdot R_{DS} \cdot dt
 \end{aligned} \tag{3-4}$$

However, due to the S1 and S3 is pulse-width modulating, the conducting current is discontinuous as shown in Fig. 3.5. The high winding inductance results in small current ripple, so the conducting current can be approximated as rectangular. This brings about the following result.

$$\begin{aligned}
 \frac{1}{T_{com}} \int_0^{T_{com}} i_{S3}^2(t) \cdot dt &\approx \frac{1}{T_{com}} \sum_{n=1}^k i_{S3}[n]^2 \cdot D \cdot T_{sw} \\
 &\approx D \cdot I_{rms}^2
 \end{aligned} \tag{3-5}$$

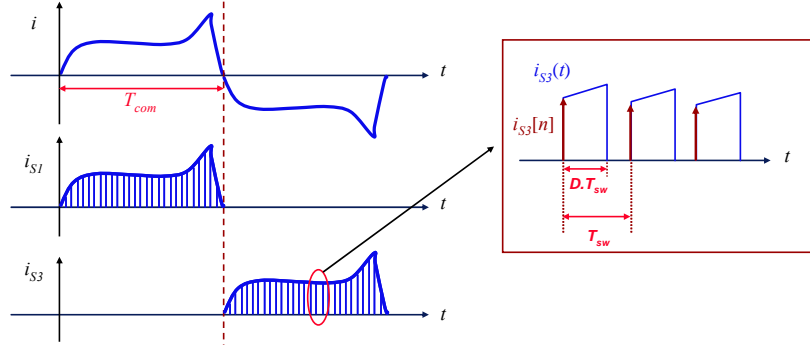


Fig. 3.5. Conducting current of transistor S1 and S3.

where D is the duty ratio when motor is operated at 3000 RPM and

$$k = \frac{T_{com}}{T_{sw}} \quad (3-6)$$

where T_{sw} is the switching period. From (3-6), it means that the conducting current i_{S3} is computed at k discrete times, which are separated by a fixed time interval T_{sw} . Thus, equation (3-4) can be revised as

$$\begin{aligned} P_{S1,con} &= P_{S3,con} \\ &\approx \frac{1}{2} \cdot R_{DS} \cdot D \cdot I_{rms}^2 \end{aligned} \quad (3-7)$$

From (3-7), the duty ratio and conducting resistance are higher, more conduction losses are generated.

Power dissipation during the turning on and turning off transitions are discussed together. Fig. 3.6 shows the simplified version of the switching waveform. When the transistor is on, the drain-source voltage v_{DS} is approximately zero. At the onset of the turning off, v_{DS} is assumed to rise linearly until reaching the steady-state off voltage V_{DC} , then the conducting current decreases to zero. During the turn-on interval, the conducting current increases first, then the drain-source voltage of switch linearly decreases. It is also assumed that the conducting current is constant during switching transition. Therefore, the energy losses during the transistor transition can be formulated as

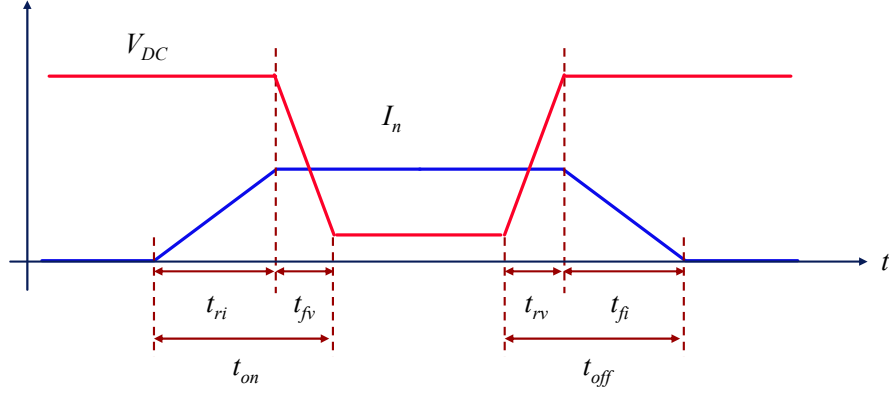


Fig. 3.6. The switching transition during turn-on time and turn-off time.

$$\begin{aligned}
 E_{n,sw} &= \frac{1}{2} \cdot V_{DC} \cdot I_n \cdot (t_{ri} + t_{fi}) + \frac{1}{2} \cdot I_n \cdot V_{DC} \cdot (t_{fv} + t_{rv}) \\
 &= \frac{1}{2} \cdot V_{DC} \cdot I_n \cdot (t_{on} + t_{off})
 \end{aligned} \tag{3-8}$$

where V_{DC} is the voltage across the transistor when switch is turn-off and I_n is the conducting current at n^{th} switching time. t_{ri} and t_{fv} are rise time of conducting current and fall time of voltage drop, respectively. t_{fi} and t_{rv} are fall time of conducting current and rise time of terminal voltage, respectively. t_{on} and t_{off} is the turn-on time and the turn-off time, respectively. From (3-8), the switching losses of S1 and S3 over an electrical cycle can be expressed as

$$\begin{aligned}
 P_{S1,sw} &= P_{S3,sw} \\
 &= \frac{1}{2T_{com}} \sum_{n=1}^k E_{n,sw} \\
 &= \frac{1}{2T_{com}} \sum_{n=1}^k \frac{1}{2} \cdot V_{DC} \cdot I_n \cdot (t_{on} + t_{off}) \\
 &= \frac{1}{2T_{com}} \cdot \frac{1}{2} \cdot V_{DC} \cdot [I_1 + I_2 + \dots + I_k] (t_{on} + t_{off})
 \end{aligned} \tag{3-9}$$

where

$$I_1 + I_2 + \dots + I_n \approx k \cdot I_{av} \tag{3-10}$$

where I_{av} is average current over an commutation cycle, and k is the same with (3-6). Thus, (3-9) can be revised as

$$\begin{aligned}
P_{S1,sw} &= P_{S3,sw} \\
&\approx \frac{1}{2T_{com}} \cdot \frac{1}{2} \cdot V_{DC} \cdot k \cdot I_{av} \cdot (t_{on} + t_{off}) \\
&= \frac{1}{2} \cdot \frac{1}{2} \cdot V_{DC} \cdot I_{av} \cdot f_{sw} \cdot (t_{on} + t_{off})
\end{aligned} \tag{3-11}$$

where f_{sw} is the switching frequency of power inverter. From (3-11), it can be seen that the switching losses are closely related to the switching frequency and switching transition time.

Except the transistor losses, the diode losses also have significant proportion of total power losses. The diode characteristics assumed for this modeling are shown in Fig. 3.7. The diode is modeled as a forward voltage V_D during diode conduction. In the off state, the diode is characterized as an infinite resistance. It is also assumed that the switching time of the diode is much smaller than the switching time of the transistor, so the switching loss of diode is almost zero. Integration of the instantaneous diode power over the electrical cycle provides the conduction losses. The diode conducting current is shown in Fig. 3.8, and it can be seen that the diode conduction time is identical to the transistor off time. Thus, diode conduction losses can be expressed as

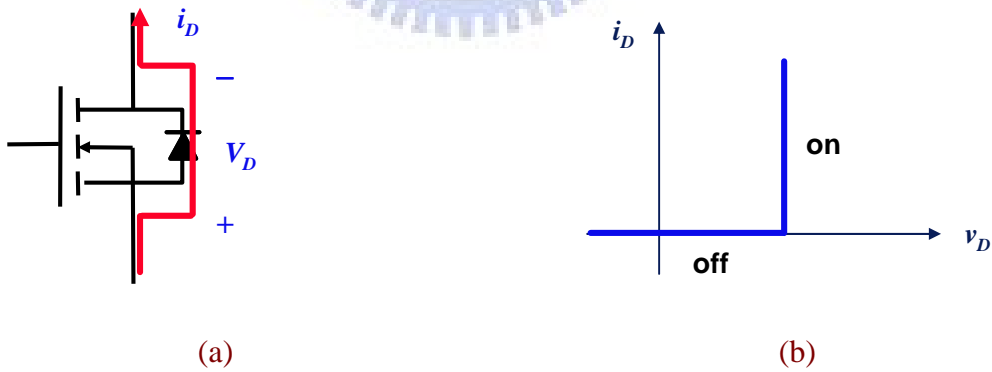


Fig. 3.7. Model of diode's characteristic.

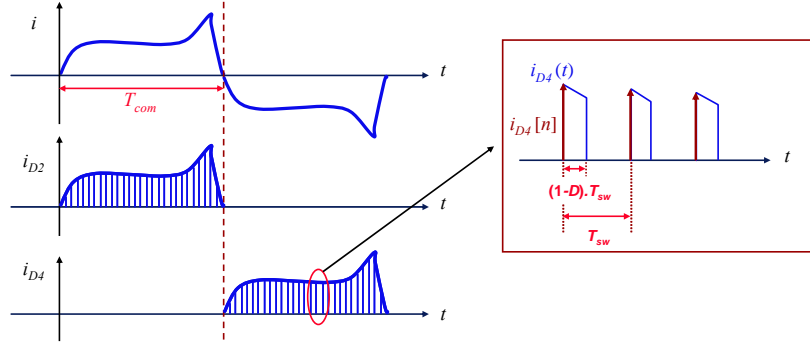


Fig. 3.8. Conducting current of diode D2 and D4.

$$\begin{aligned}
 P_{D2,con} &= P_{D4,con} \\
 &= \frac{1}{2T_{com}} \int_0^{T_{com}} V_D \cdot i_{D4}(t) \cdot dt \\
 &\approx \frac{1}{2T_{com}} \cdot V_D \cdot \sum_{n=1}^k i_{D4}[n] \cdot (1-D) \cdot T_{sw} \\
 &\approx \frac{1}{2} \cdot V_D \cdot (1-D) \cdot I_{av}
 \end{aligned} \tag{3-12}$$

where V_D is diode conducting voltage. From (3-12), the diode forward voltage is higher, more diode conduction losses are generated.

With the above expressions, these losses are combined into the total losses by summing (3-3), (3-7), (3-11), and (3-12) together. The related parameters and the operation conditions list in Table 3.1. So, the total power loss P_{total} in the inverter based on PWM switching scheme 1 is given as

$$\begin{aligned}
 P_{total} &= P_{S2,con} + P_{S4,con} + P_{S1,con} + P_{S3,con} + P_{S1,sw} + P_{S3,sw} + P_{D2,con} + P_{D4,con} \\
 &= R_{DS} \cdot (1+D) \cdot I_{rms}^2 + \frac{1}{2} \cdot V_{DC} \cdot I_{av} \cdot f_{sw} \cdot (t_{on} + t_{off}) + V_D \cdot (1-D) \cdot I_{av} \cdot \\
 &= 48.79 \text{ (mW)}
 \end{aligned} \tag{3-13}$$

Fig. 3.9 is the pie chart of total power losses for PWM switching scheme 1. There is large proportion of diode conduction losses, and transistor switching losses are secondary. Therefore, the advantages of this scheme are small dc-link capacitance requirement and reduction of transistor switching losses. But, it sacrifices the power losses in diode conduction.

TABLE 3.1
Parameters and operation conditions for calculating power losses

Speed	3000 RPM
Control scheme	Hard-commutation
DC-link voltage (V_{DC})	12 V
Conducting resistance (R_{DS})	5.6 $m\Omega$
Conducting voltage (V_D)	1 V
Switch turn-on time (t_{on})	140 ns
Switch turn-off time (t_{off})	150 ns
Switching frequency (f_{sw})	20 kHz

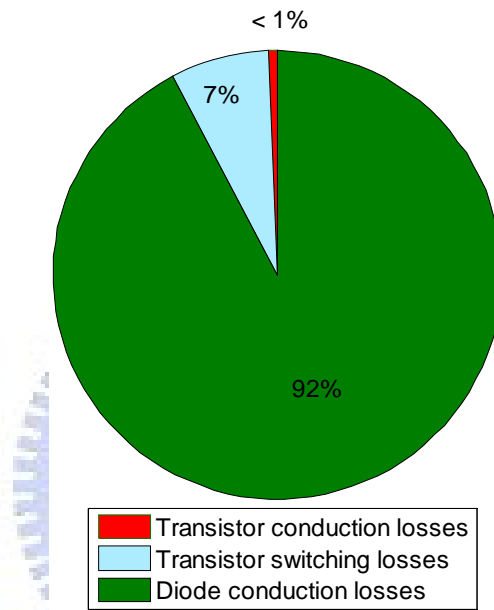


Fig. 3.9. Pie chart of total power losses for PWM switching scheme 1.

3.1.2 PWM Switching Scheme 2

In this scheme, positive voltage is applied by pulse-width modulating S1 and S4 simultaneously as shown in Fig. 3.10. When both S1 and S4 are driving states, phase current will increase as in scheme 1. Motor current during the PWM off period decays rapidly through two anti-parallel diodes of S2 and S3, and reverse application of dc-link voltage (regeneration state). That is, two simultaneous switching of two transistors occur in a PWM period.

Similarly, the following will calculate the power losses over an electrical cycle. The parameters and operation condition is identical to PWM switching scheme 1. Due to the

simultaneous switching, the conduction losses of S1 and S4 equal to (3-7) which can be expressed as

$$\begin{aligned} P_{S1,con} &= P_{S4,con} \\ &\approx \frac{1}{2} \cdot R_{DS} \cdot D \cdot I_{rms}^2 \end{aligned} \quad (3-14)$$

The switching losses of S1 and S4 are identical to (3-8), that is

$$\begin{aligned} P_{S1,sw} &= P_{S4,sw} \\ &\approx \frac{1}{2} \cdot \frac{1}{2} \cdot V_{DC} \cdot I_{av} \cdot f_{sw} \cdot (t_{on} + t_{off}) \end{aligned} \quad (3-15)$$

After current commutation, the conduction losses of S2 and S3 are identical to (3-14), and the switching losses are identical to (3-15). On the other hand, the diode conduction losses equal to (3-12) which can be formulated as

$$\begin{aligned} P_{D1,con} &= P_{D2,con} = P_{D3,con} = P_{D4,con} \\ &\approx \frac{1}{2} \cdot V_D \cdot (1-D) \cdot I_{av} \end{aligned} \quad (3-16)$$

Therefore, based on PWM switching scheme 2, the total losses in the power inverter are

$$\begin{aligned} P_{total} &= 4 \cdot P_{S1,con} + 4 \cdot P_{S1,sw} + 4 \cdot P_{D1,con} \\ &= 2 \cdot R_{DS} \cdot D \cdot I_{rms}^2 + V_{DC} \cdot I_{av} \cdot f_{sw} \cdot (t_{on} + t_{off}) + 2 \cdot V_D \cdot (1-D) \cdot I_{av} \end{aligned} \quad (3-17)$$

= 97.18(mW)

There are twice diode conduction losses and twice transistor switching losses compared to scheme 1. Fig. 3.11 is the pie chart of total power losses for PWM switching scheme 2. In this example, not only the bus capacitance requirement is large, but also the switching losses are increasing. In view of power losses, it is unsuitable for high efficiency motor drives.

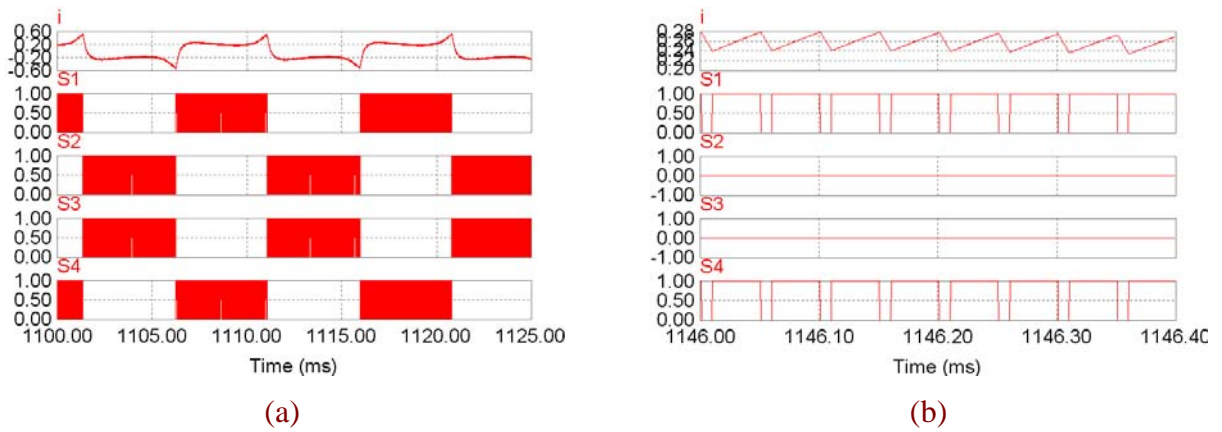


Fig. 3.10. (a) PWM switching scheme 2 and (b) macro view of switching pattern.

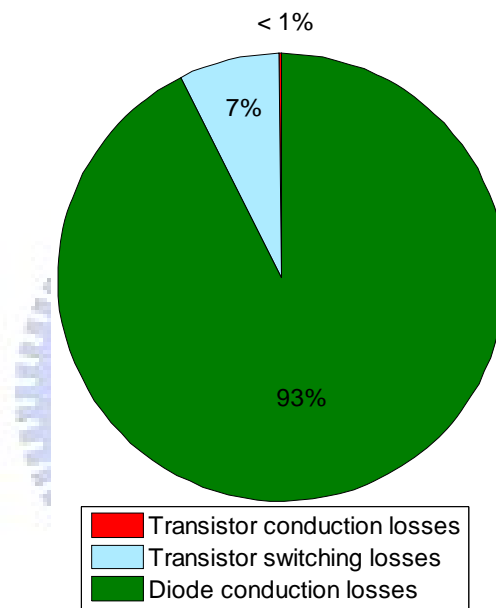


Fig. 3.11. Pie chart of total power losses for PWM switching scheme 2.

3.1.3 PWM Switching Scheme 3

This technique is called synchronous rectification. This mode operates similarly to scheme 2 above, except that the switching states of S3 and S2 are complementary to S1 and S4 as shown in Fig. 3.12. This method has distinct difference over scheme 2 is that the current during regeneration state will flow through transistors instead of the anti-parallel diode, so the conduction losses of diode is zero. By using transistors with low conducting resistance, conduction losses can be reduced to less than that of the diode alone.

When S1 and S4 are driving states, the conduction losses can be expressed as

$$\begin{aligned}
P_{S1,con} &= P_{S4,con} \\
&\approx \frac{1}{2} \cdot R_{DS} \cdot D \cdot I_{rms}^2.
\end{aligned} \tag{3-18}$$

Due to the complementary switching, the conduction losses of S2 and S3 are

$$\begin{aligned}
P_{S2,con} &= P_{S3,con} \\
&\approx \frac{1}{2} \cdot R_{DS} \cdot (1-D) \cdot I_{rms}^2.
\end{aligned} \tag{3-19}$$

After current commutation, the conduction losses of S2 and S3 are identical to (3-18) and the conduction losses of S1 and S4 are identical to (3-19). Thus, the conduction losses of each transistor over an electrical cycle are

$$\begin{aligned}
P_{S1,con} &= P_{S2,con} = P_{S3,con} = P_{S4,con} \\
&\approx \frac{1}{2} \cdot R_{DS} \cdot I_{rms}^2.
\end{aligned} \tag{3-20}$$

For switching losses of complementary PWM scheme, there are twice power losses of PWM scheme 2. That is,

$$\begin{aligned}
P_{S1,sw} &= P_{S2,sw} = P_{S3,sw} = P_{S4,sw} \\
&\approx \frac{1}{2} \cdot V_{DC} \cdot I_{av} \cdot f_{sw} \cdot (t_{on} + t_{off}).
\end{aligned} \tag{3-21}$$

Therefore, based on PWM switching scheme 3, the total losses in the power inverter are

$$\begin{aligned}
P_{total} &= 4 \cdot P_{S1,con} + 4 \cdot P_{S1,sw} \\
&= 2 \cdot R_{DS} \cdot I_{rms}^2 + 2 \cdot V_{DC} \cdot I_{av} \cdot f_{sw} \cdot (t_{on} + t_{off}). \\
&= 14.32 \text{ (mW)}
\end{aligned} \tag{3-22}$$

Due to the absence of diode losses, total power losses have a 70 % reduction compared to scheme 1. Fig. 3.13 is the pie chart for PWM switching scheme 3. In this example, the switching losses of transistors become a major part. The conduction losses of transistors are relatively small for very low conduction resistance. So, in view of power losses, PWM switching scheme 3 is better than scheme 1 and scheme 2.

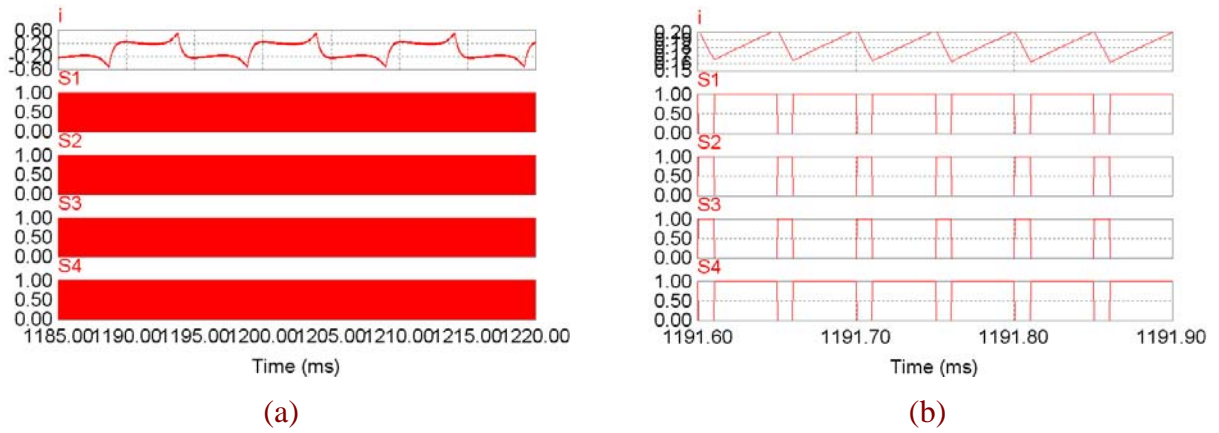


Fig. 3.12. (a) PWM switching scheme 3 and (b) macro view of switching pattern.

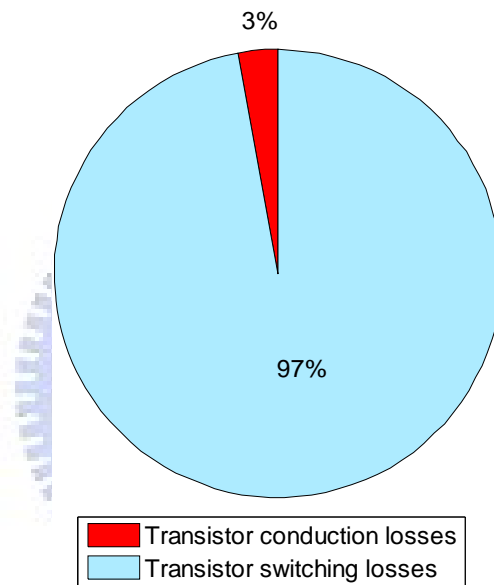


Fig. 3.13. Pie chart of total power losses for PWM switching scheme 3.

3.1.4 PWM Switching Scheme 4

This scheme is similar to PWM switching Scheme 3 except that the switching on each phase occurs at different times. Fig. 3.14 shows that the switching of S4 is that of S1 delayed by one half of a PWM period. For one commutation cycle, there are three states for iteration: driving state, short-to-high state, and short-to-low state. There is no diode conducting time, so conduction losses in diodes can be eliminated, and the total power will be significantly reduced.

When S1 and S4 are driving states, the conduction losses over an electrical cycle can be

expressed as

$$\begin{aligned} P_{S1,con} &= P_{S4,con} \\ &\approx \frac{1}{2} \cdot R_{DS} \cdot D \cdot I_{rms}^2 \end{aligned} \quad (3-23)$$

When S1 and S3 are short-to-high state, the conduction losses of S1 and S3 are

$$\begin{aligned} P_{S1,con} &= P_{S3,con} \\ &\approx \frac{1}{2} \cdot \frac{1}{2} \cdot R_{DS} \cdot (1-D) \cdot I_{rms}^2 \end{aligned} \quad (3-24)$$

When S2 and S4 are short-to-low state, the conduction losses of S2 and S4 are

$$\begin{aligned} P_{S2,con} &= P_{S4,con} \\ &\approx \frac{1}{2} \cdot \frac{1}{2} \cdot R_{DS} \cdot (1-D) \cdot I_{rms}^2 \end{aligned} \quad (3-25)$$

After current commutation, the conduction losses of transistors are identical to (3-23), (3-24), and (3-25). On the other hand, due to the number of time for switching is identical to PWM scheme 3, the switching losses are equal to (3-21). The total power losses over an electrical cycle can be expressed as

$$\begin{aligned} P_{total} &= 2 \cdot R_{DS} \cdot I_{rms}^2 + 2 \cdot V_{DC} \cdot I_{av} \cdot f_{sw} \cdot (t_{on} + t_{off}) \\ &= 14.32 \text{ (mW)} \end{aligned} \quad (3-26)$$

From (3-26), it can be seen that each power loss equals to that of PWM scheme 3 as well as the pie chart as shown in Fig. 3.15. Because the switching pattern of transistor, the current ripple is twice the switching frequency and the magnitude is half of other PWM switching schemes. Moreover, there is no reverse current direction to voltage source, so the requirement of dc-link capacitance is small.

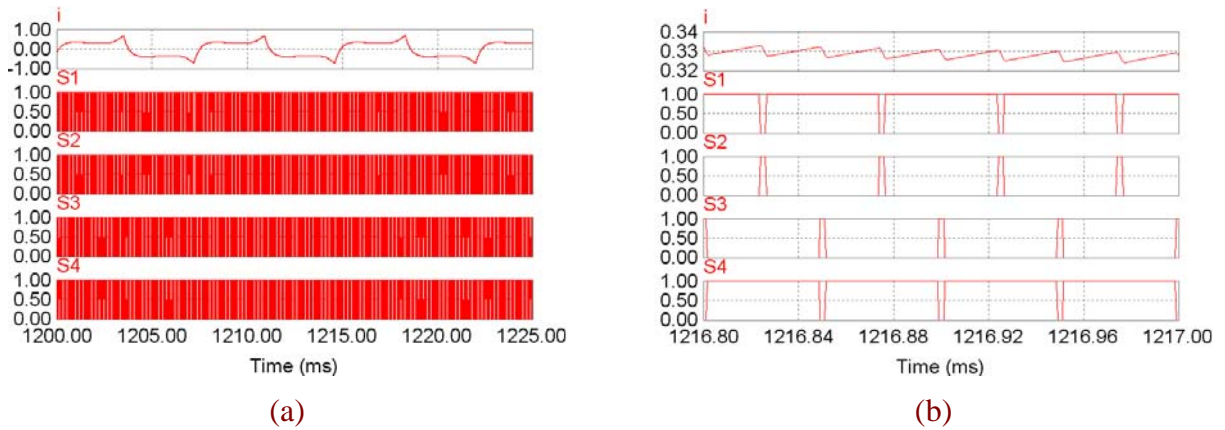


Fig. 3.14. (a) PWM switching scheme 4 and (b) macro view of switching pattern.

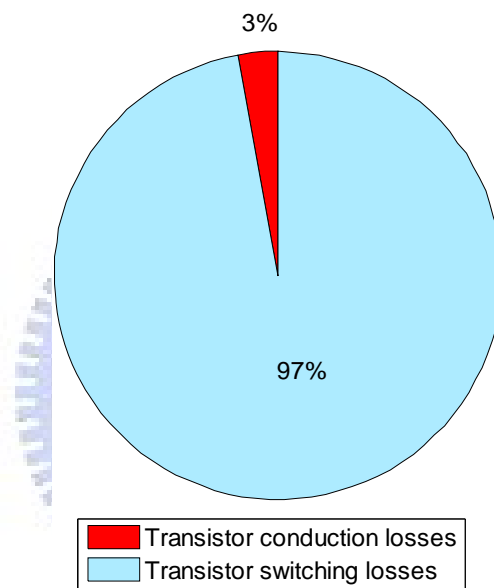


Fig. 3.15. Pie chart of total power losses for PWM switching scheme 4.

From above discussion, it was found that selection of the switching scheme affects performance characteristics such as current ripples in dc-link and power losses in the full-bridge inverter. This research uses the PWM switching scheme 4 to control the single-phase BLDC fan motor, which is advantageous for low power losses. The reason is that conduction losses and switching losses in the MOSFET is well below diode conduction losses, which results in higher efficiency than scheme 1 and 2. Moreover, the reverse current will circulate in high-side or low-side switches, so dc-link capacitance is small and the control at around zero current is superior to scheme 3.

3.2 OPEN-LOOP VOLTAGE-MODE CONTROL OF SOFT-COMMUTATION SCHEME

Except for reducing the power losses in PWM inverter, the motor output power should be paid more attention. The overall efficiency will be improved by increasing the utilization ratio of current which is closely related to current profile. There is a simple drive method called soft-commutation scheme is adopted to reduce the current spike at commutation boundary [5]-[6]. In this working mode, still open-loop control of square-wave voltage is applied to the phase winding, but its switching pattern is modified by adding a proper blanking time into the driving voltage. Fig. 3.16 shows the operation waveform for open-loop voltage-mode control of soft-commutation scheme. It shows that the switches of inverter are turned off before the commutation boundary, so the peak current will be reduced before the back-EMF seriously drops. The blanking time can be controlled to ensure that the driving current decays to zero before the back-EMF changes polarity, and there is no negative torque will be produced at both low and high speed.

Fig. 3.17 shows steady-state response when using soft-commutation scheme with different blanking times at 4000 RPM. There are 10 % reduction of RMS current and 38 % reduction of peak current for comparing phase current between Fig. 3.17(a) and Fig. 3.17(b), while there are 19 % reduction of RMS current and 45 % reduction of peak current for comparing phase current between Fig. 3.17(a) and Fig. 3.17(c). It can be seen that the blanking time of 15 % commutation cycle has the better efficiency than blanking time of 10 % commutation cycle. So, if the blanking time is sufficient, the overall efficiency can be promoted and the peak current can be significant reduced.

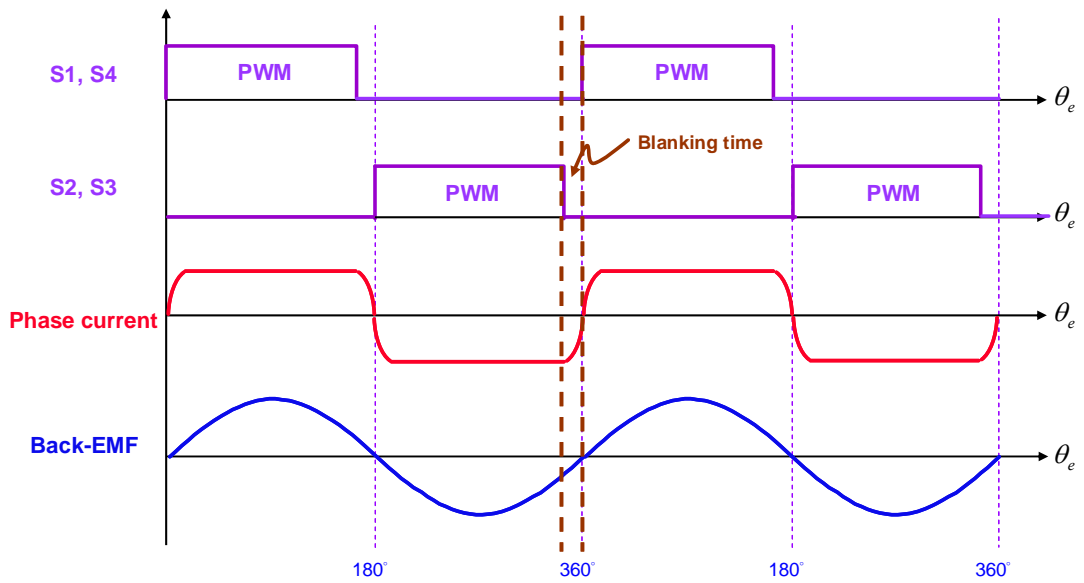
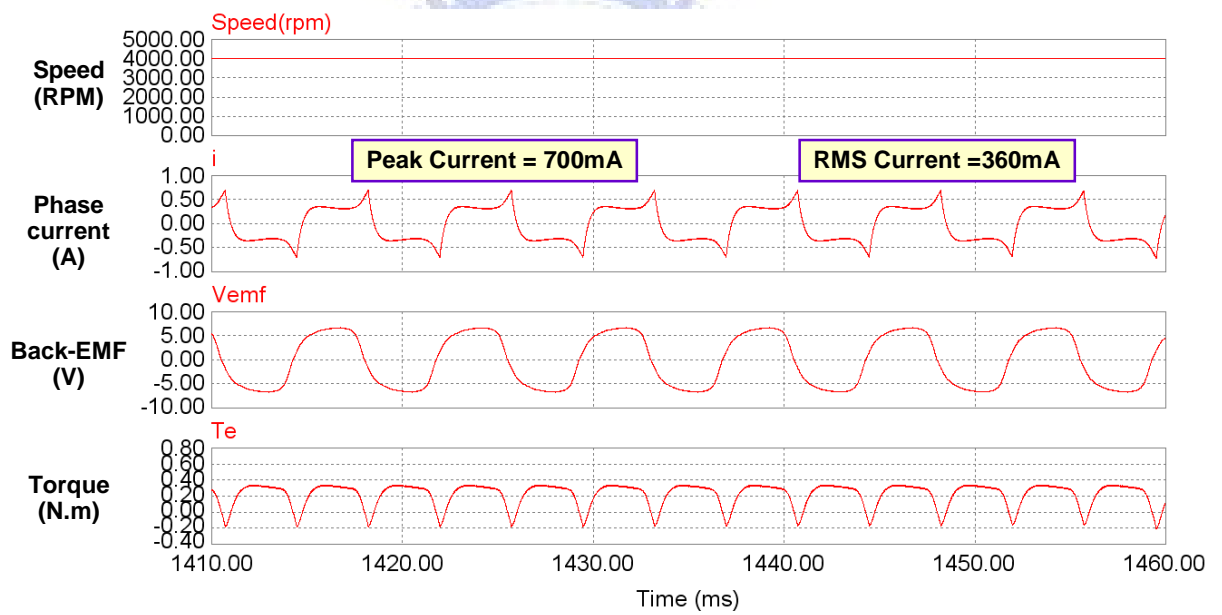
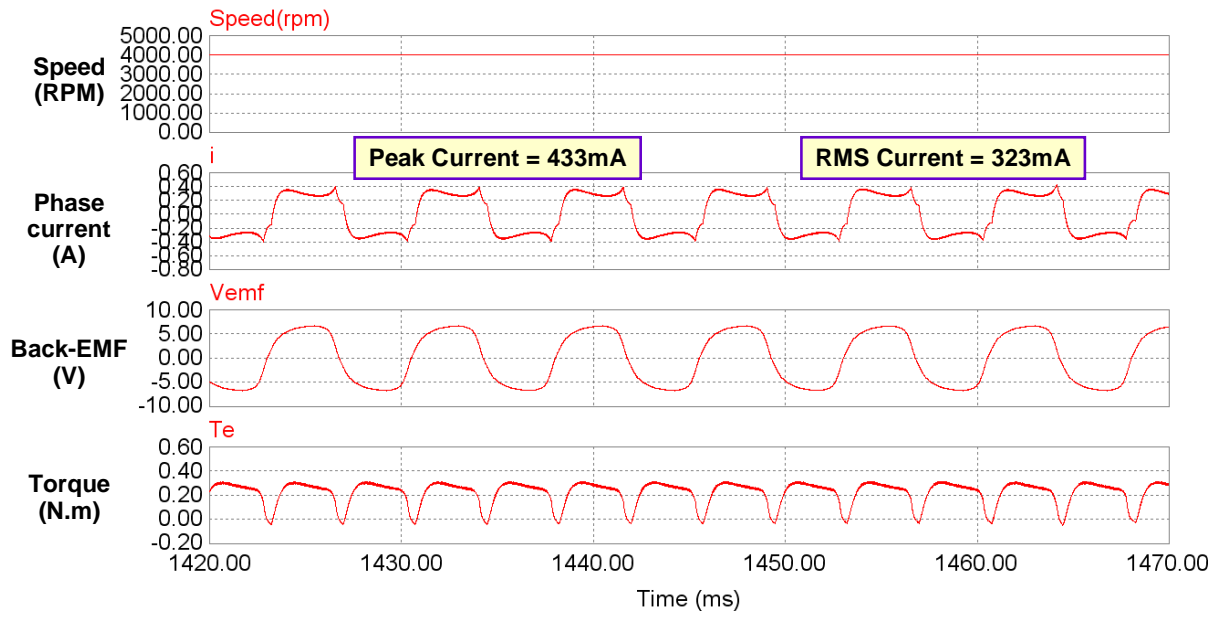


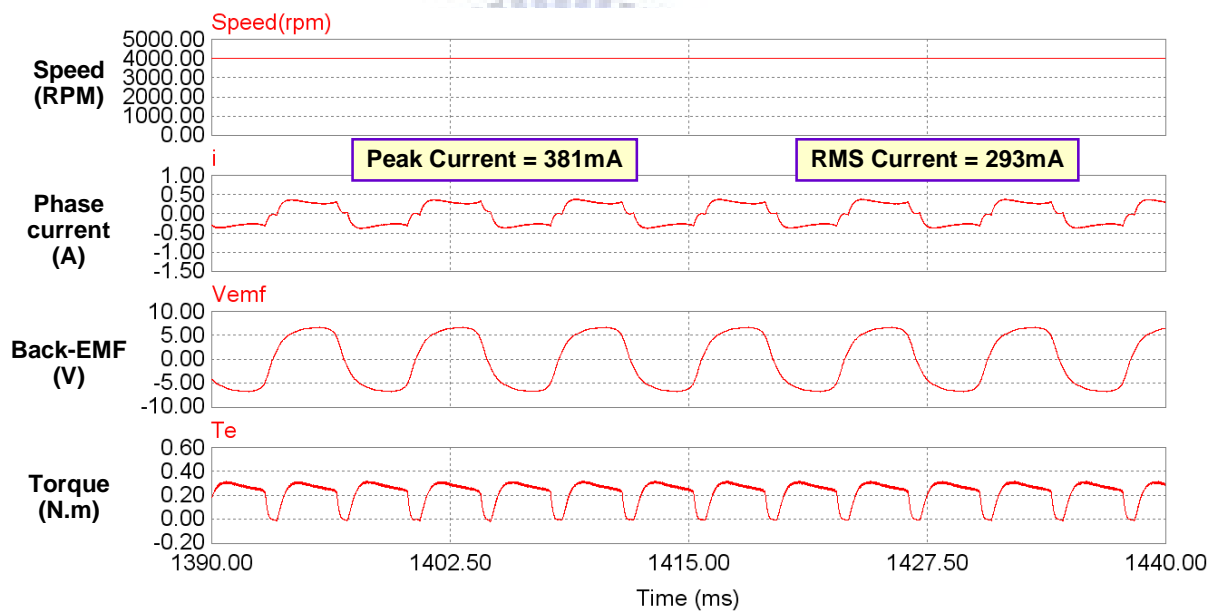
Fig. 3.16. The operation waveform for open-loop voltage-mode control of soft-commutation scheme.



(a)



(b)



(c)

Fig. 3.17. The steady-state waveforms when using soft-commutation scheme with different blanking times at 4000 RPM (a) no blanking time, (b) blanking time of 10 % commutation cycle, and (c) blanking time of 15 % commutation cycle.

However, if the blanking time is too short, the developed torque will be reduced, which is disadvantage for wide speed control applications of single-phase BLDC fan motor. Therefore, the key to this method is the proportion of blanking time. Due to the motor inductance, the driving current will pass through the anti-parallel diode and decrease to zero if the switches are turned off during the blanking time. Fig. 3.18 shows the equivalent circuit after turning off the switches. The current response can be formulated as

$$i(t) = i_0 e^{-\frac{R_s t}{L_s}} - \frac{V_{DC} + 2V_D + v_{emf}}{R_s} \quad (3-27)$$

where i_0 is initial current passes through the anti-parallel diode after turning off the switches, and V_D is the diode conducting voltage. Generally, the larger initial current is, the longer blanking time is necessary to decay the current to zero. Fig. 3.19 shows the simulation results of steady-state waveform when using soft-commutation scheme under different speed operations. It can be seen that the current spike is reduced and there is no negative torque is produced. As shown in Fig. 3.19(a), it needs the blanking time of 10 % commutation cycle to operate under 3000 RPM. In Fig. 3.19(b), the blanking time shortens to 5 % to operate under 1000 RPM because of smaller current, and the corresponding result is almost the same to hard-commutation scheme. That is to say, the soft-commutation scheme is not suitable for low speed operation.

According to above description, when using the soft-commutation scheme, there exists an optimal blanking time for the given speed. However, it is a complicated process to find the optimal solution for wide speed control range of fan motor. Furthermore, the overall efficiency has significant improvement only for high speed operation. For low speed operation, the system performance is almost the same to the result of using the hard-commutation scheme. Therefore, the soft-commutation scheme is disadvantage for promoting efficiency over entire speed control range of single-phase BLDC fan motor.

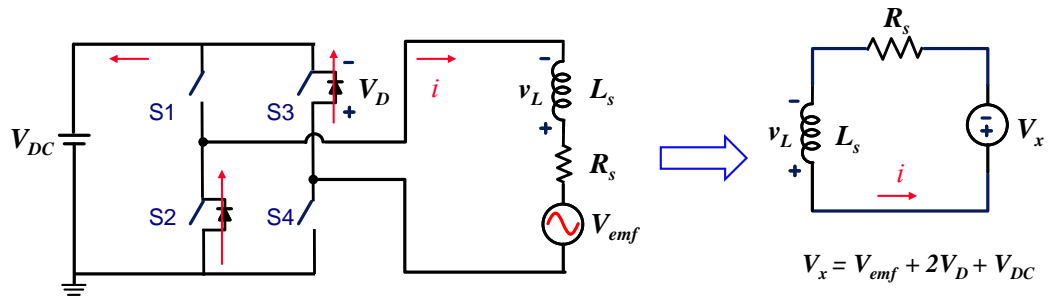


Fig. 3.18. The equivalent circuit when turning off the switches.

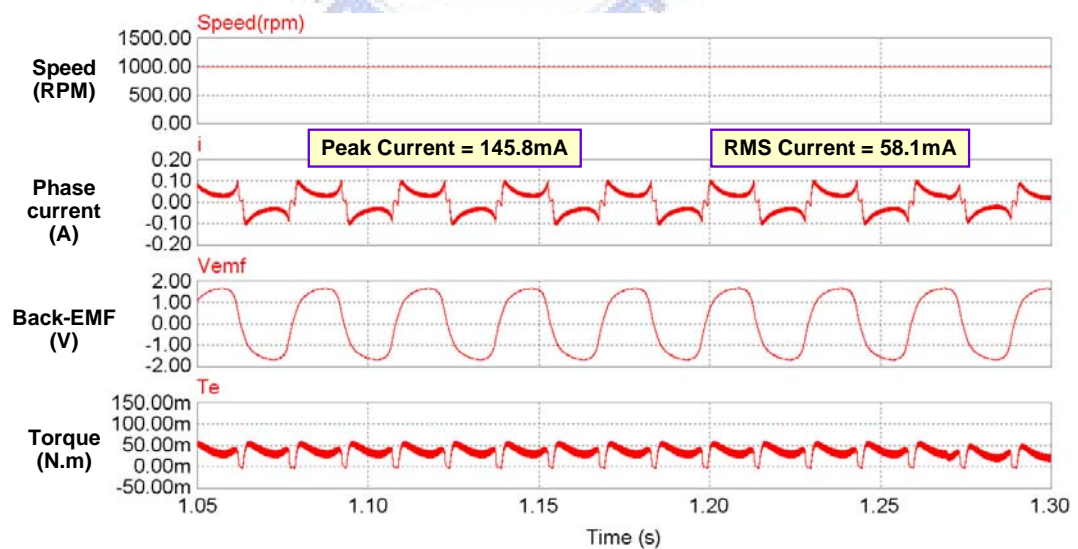
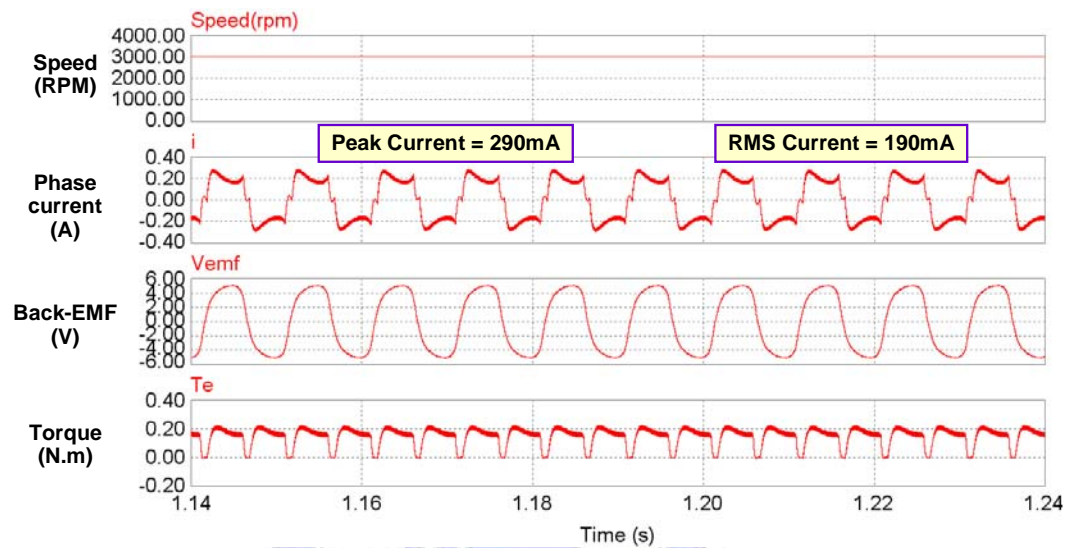


Fig. 3.19. The steady-state waveforms when using soft-commutation scheme (a) 3000 RPM with blanking time of 10 % commutation cycle and (b) 1000 RPM with blanking time of 5 % commutation cycle.

3.3 EFFICIENCY OPTIMIZATION CONTROL SCHEME

From previous section, both of hard-commutation and soft-commutation scheme are still sensitive to the rotor flux distribution, so the overall efficiency will be seriously degraded in wide speed control applications. This research develops the efficiency optimization control scheme based on closed-loop current-mode control scheme for single-phase BLDC fan motors. Moreover, the advantage of soft-commutation control at high speed operation will be adopted to widen the speed control range and to reduce the current spike.

3.3.1 Principle of Efficiency Optimization

Due to the machine design and structure, the induced back-EMF in the single-phase BLDC fan motor is highly nonlinear and contains harmonics. The product of back-EMF and phase current produces the electrical output power. Therefore, it has to consider all the harmonics when calculating output power. The average output power is presented as

$$P_{av} = \frac{1}{T} \int_0^T e(t) \cdot i(t) dt \quad (3-28)$$

and each back-EMF and phase current is described as

$$\begin{aligned} e(t) &= E_1 \sin \omega t + E_3 \sin 3\omega t + E_5 \sin 5\omega t + \dots \\ i(t) &= I_1 \sin(\omega t - \phi_1) + I_3 \sin 3(\omega t - \phi_3) + I_5 \sin 5(\omega t - \phi_5) + \dots \end{aligned} \quad (3-29)$$

where E_n and I_n represent the peak magnitude of each harmonic of back-EMF and phase current. ϕ_n is the phase difference between each back-EMF and phase current. For maximum output power, each back-EMF and current harmonics should be in phase [24]. Otherwise, the output power has a negative value during every cycle and average power can not be the maximum possible. The maximum output power is given as

$$P_{av,max} = \frac{1}{2} (E_1 I_1 + E_3 I_3 + E_5 I_5 + \dots). \quad (3-30)$$

Under this condition, there are many current waveforms may produce the maximum output power. However, there is an optimal current waveform to achieve the maximum efficiency for single-phase BLDC fan motor drives. If each harmonic of phase current is same to the back-EMF, the RMS value of phase current is minimum and the corresponding power loss in passive element is minimum. Therefore, in order to realize the maximum efficiency, the phase current waveform should be identical and in phase with the back-EMF.

3.3.2 System Configuration

The digital control offers advantages over analog control such as re-programmability, better noise immunity, and low susceptibility to age and environmental factors. With the rapidly development of integrated circuit, DSPs and the analog-to-digital (A/D) converters have improved their performances in speed and functionality, and their cost-prohibitive problem has begun to fade. Therefore, these approaches provide flexibility and are suitable for many applications, among them, the digital motor control systems have been widely implemented with software based on microcontrollers or DSPs [28]-[30].

To reach the purposes mentioned in previous section, the closed-loop current-mode control scheme is employed with linear Hall sensor feedback [25]-[27]. Fig. 3.20 shows the block diagram of closed-loop current-mode control system. The system uses voltage source inverter topologies, so the addition of closed-loop current-mode control yields a configuration referred to as a current-regulated voltage source inverter. The closed-loop system behaves like a very fast current source inverter, depending on the internal motor phase inductances combined with closed-loop control to provide the desired current source characteristics. The system consists of a digital PWM generator and a current-loop controller. Moreover, there is an A/D converter to sample the phase current and Hall sensor. The current controller determines the value of the switch duty ratio based on error between the reference and actual current, and then the PWM generator outputs corresponding waveform to control the switches.

The linear Hall sensor produces an output signal which is proportional to the intensity of the induced rotor field. That is to say, the waveform of Hall sensor output voltage is identical with the back-EMF. Fig. 3.21 shows the current multiplier control (CMC) scheme with linear Hall sensor feedback. The Hall sensor signals can be regarded as a unit amplitude reference for the corresponding phase current. The torque command is multiplied by the reference Hall sensor signals to produce phase current command.

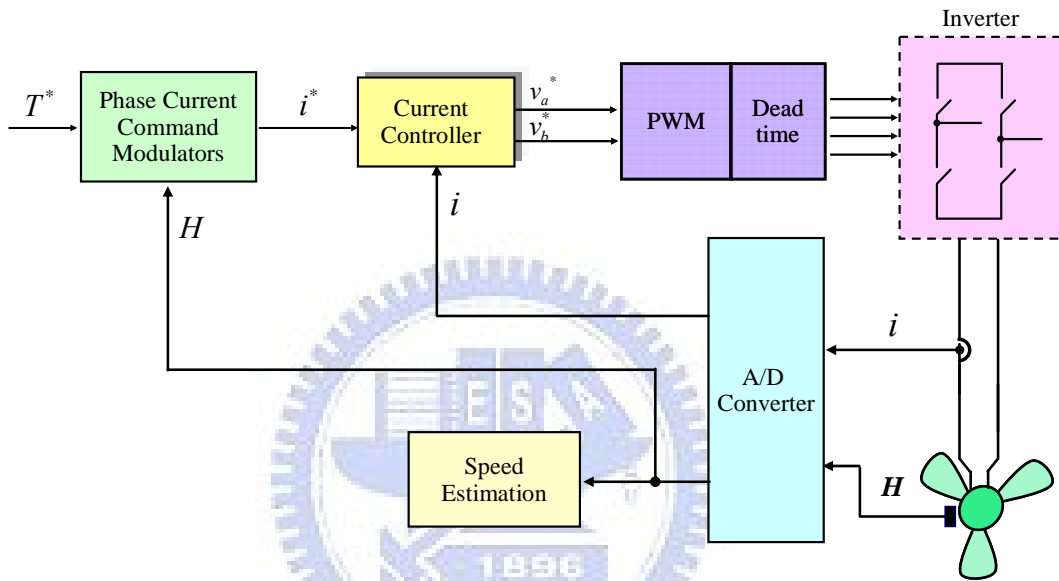


Fig. 3.20. Architecture of closed-loop current-mode control system.

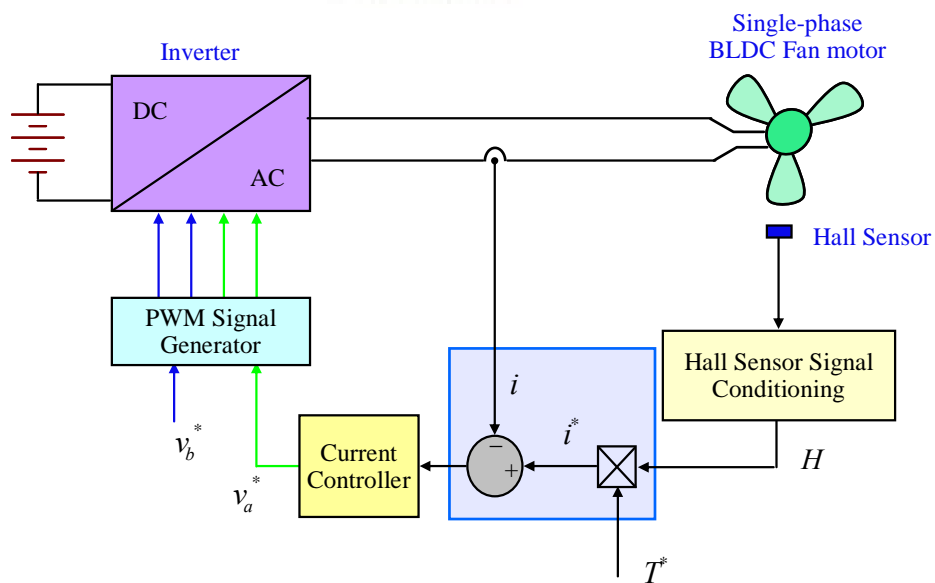


Fig. 3.21. Current multiplier control scheme with linear Hall sensor feedback.

3.3.3 Digital Current-Loop Controller Design and Consideration

The operation of the single-phase BLDC fan motor drives has been shown in Fig. 2.4. If a suitable control circuit regulates the average voltage across the motor winding between two extremes $\pm V_{DC}$, it is clearly possible to make the current follow any desired trajectory, provided that this is consistent with the physical limitations imposed by the topology. Obviously, there is a limitation of fixed dc-link voltage for full-bridge inverter, and the current will be limited in its variations. Fig. 3.22 is the current step response when fan motor keeps standstill, and it shows that the different operation points have different slew rates. From (2-17), there is a maximum slew rate occurs at starting instant, which can be expressed as

$$\left. \frac{di(t)}{dt} \right|_{t=0} = \frac{V_{DC}}{L_s} \quad (3-31)$$

It can be seen that the maximum slew rate is limited in dc-link voltage. In practice, the maximum current absolute value will be limited as well, because of the limited current handling capability of the power devices. This limitation, different from the previous one, is not inherent to the circuit topology and will need to be enforced by a current-loop controller, in order to prevent accidental damage to the switches.

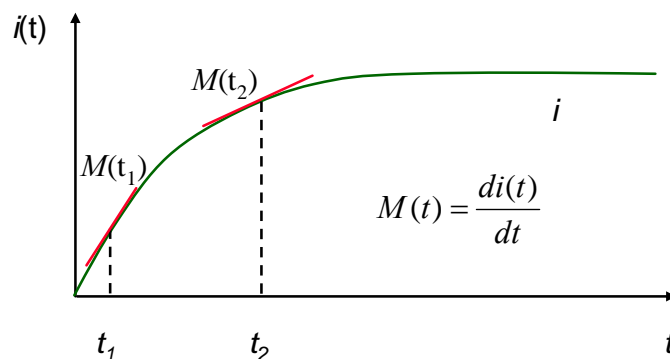
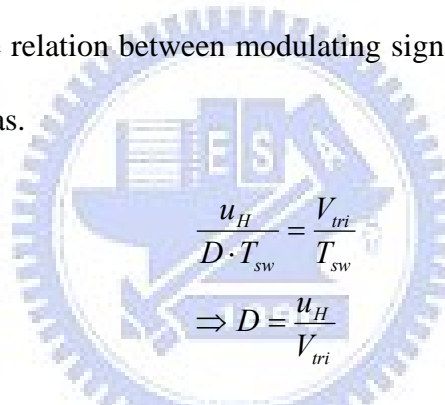


Fig. 3.22. The current response when motor is standstill.

The current-loop controller outputs the appropriate value to the digital PWM generator for generating corresponding waveform to control the switches. So, the design of digital current controller should take the digital PWM effect into account [31]. This research uses the single-update-mode triangular-carrier modulator as shown in Fig. 3.23, and it's also called a symmetric-on-time modulator. The counter is incremented at every clock pulse; any time the binary counter value is equal to the programmed duty ratio, the binary comparator triggers an interrupt to the DSP and, at the same time, sets the gate signal low. The gate signal is set high at the beginning of each counting period, where another interrupt is typically generated for synchronization purposes. The modulating signal update is performed only at the beginning of each modulation period. Such mode of operation can be served as a sample and hold effect. In one switching period, the relation between modulating signal u_s and the resulting PWM duty ratio D can be described as.



$$\frac{u_H}{D \cdot T_{sw}} = \frac{V_{tri}}{T_{sw}}$$

$$\Rightarrow D = \frac{u_H}{V_{tri}} \tag{3-32}$$

where V_{tri} is the peak value of the triangular carrier and T_{sw} is the switching period.

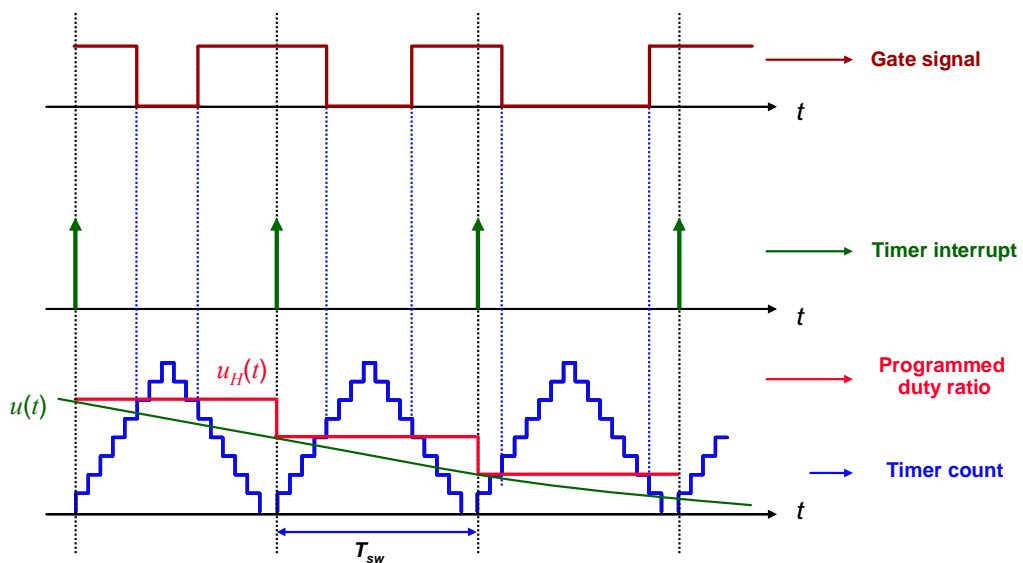


Fig. 3.23. The operation principle of single-update-mode triangular-carrier modulator.

An equivalent model of the digital PWM is represented in Fig. 3.24. As can be seen, the schematic diagram adopts the typical continuous time model of a sampled data system, where an ideal sampler is followed by a zero-order hold (ZOH). After the modulating signal $u(t)$ is processed by the ZOH, the PWM waveform is generated by an digital comparator, which compares the ZOH output signal $u_s(t)$ and the carrier waveform $v_{tri}(t)$. From reference [31], the transfer function for symmetric-on-time modulator can be expressed as

$$\begin{aligned}
 G_{PWM}(s) &= \frac{Y(s)}{U(s)} \\
 &= \frac{1}{2 \cdot V_{tri}} \left(e^{-s \frac{(1-D)T_{sw}}{2}} + e^{-s \frac{(1+D)T_{sw}}{2}} \right). \\
 &= \frac{1}{V_{tri}} e^{-s \frac{T_{sw}}{2}} \cos(\omega \frac{T_{sw}}{2} D)
 \end{aligned} \tag{3-33}$$

Considering the typical current controller bandwidth to be well below the modulation frequency, (3-33) can be revised as

$$G_{PWM}(s) \approx \frac{1}{V_{tri}} e^{-s \frac{T_{sw}}{2}}. \tag{3-34}$$

By first-order Pade approximation of (3-34), a rational and continuous time transfer function can be obtained

$$G_{PWM}(s) \approx \frac{1}{V_{tri}} \cdot \frac{1 - s \frac{T_{sw}}{4}}{1 + s \frac{T_{sw}}{4}}. \tag{3-35}$$

Fig. 3.25 shows the frequency response of $G_{PWM}(s)$. The first-order Pade approximation of (3-35) is close to the exponential term of (3-34). It also shows that the digital PWM implementation implies an increase in the system response delay. This will seriously influence the performance of the bandwidth and the phase margin of the control loop, as well as the current transient response.

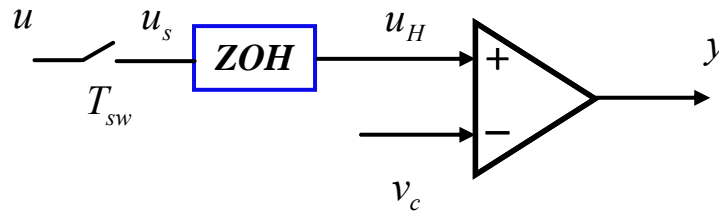


Fig. 3.24. The general digital PWM modulator.

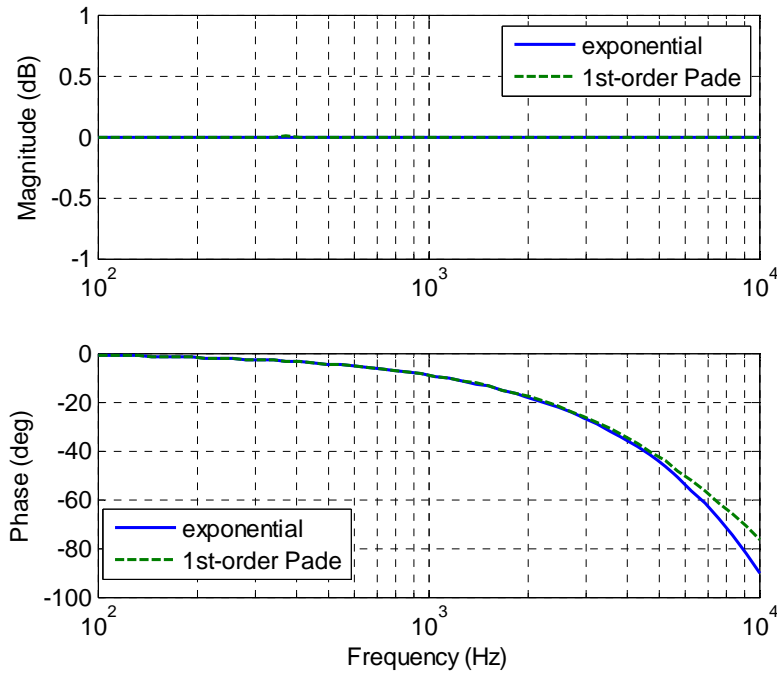


Fig. 3.25. Frequency response of $G_{PWM}(s)$.

On the other hand, the implementation of a suitable signal acquisition path is also the key for the digital current-loop controller design. Therefore, current feedback has to be converted from the continuous to the discrete time domain. Fig. 3.26 shows the control loop block diagram, where all the components are represented by their respective transfer functions or gains. The signal acquisition path for current controller can be represented by the cascade connection of a properly designed signal conditioning circuit and the A/D converter. The signal conditioning circuit should guarantee that the feedback signal is amplified to fully exploit the input voltage range of the A/D converter and be filtered to avoid aliasing effects.

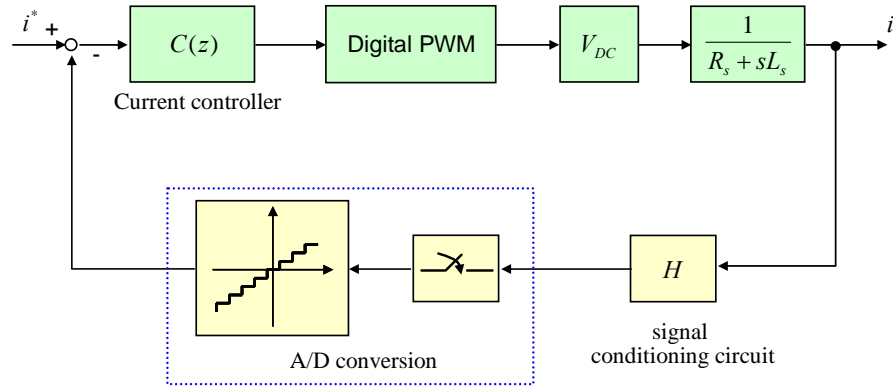


Fig. 3.26. Block diagram of current-loop control.

This research uses the digital PI controller to realize the current-regulation which ensures that the measured stator current tracks the required values accurately and to shorten the transient interval as much as possible. For simplicity, this research uses the digital redesign approach, which determines an equivalent continuous time model of overall system, to use it in the design of a continuous time controller stabilizing the feedback loop and, finally, to turn the continuous time controller into an equivalent discrete time one. The digital redesign has advantage for using some of the well known controller design methods developed for continuous-time analog implementation.

Fig. 3.27 shows the continuous time equivalent of current-loop control system, where the controller block is represented by typical PI regulator structure. The controller design is typically based on specifications concerning the required closed loop bandwidth and phase margin. In our application, we suppose that the system bandwidth f_{CL} equals to about one tenth of the switching frequency and at least a 45 degree phase margin PM. So, parameters K_P and K_I have to determine to guarantee these requirements. At first, the open loop gain of Fig. 3.27 is given as

$$G_{OL}(s) = \left(K_P + \frac{K_I}{s}\right) \cdot \frac{V_{DC}}{V_{tri}} \cdot \frac{1 - s \frac{T_{sw}}{4}}{1 + s \frac{T_{sw}}{4}} \cdot \frac{1}{R_s + sL_s} \cdot H \cdot K_{ADC}. \quad (3-36)$$

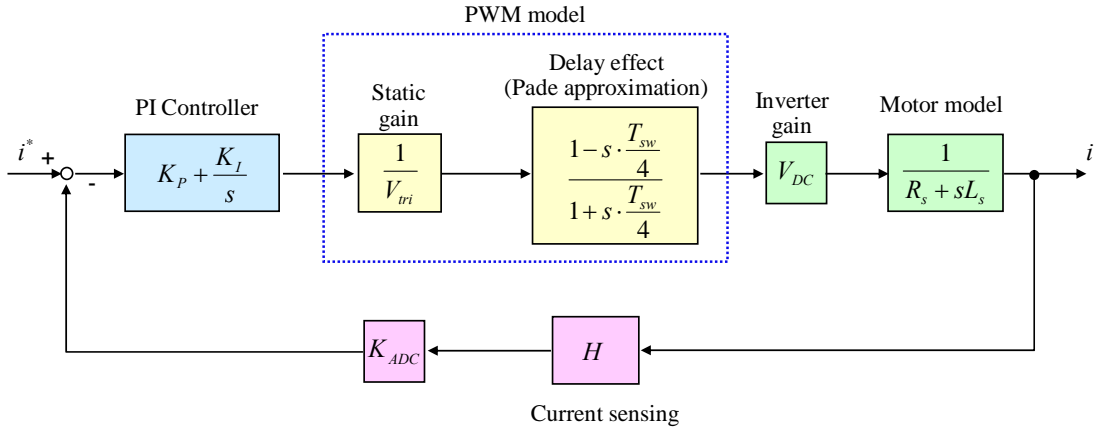


Fig. 3.27. The continuous time equivalent of current-loop control system.

Supposes that

$$K_I \ll \omega_{CL} \cdot K_P \quad (3-37)$$

where ω_{CL} is the gain crossover angular frequency. So, the open loop gain can be approximated with the following expression

$$G_{OL}(j\omega_{CL}) \approx K_P \cdot \frac{V_{DC}}{V_{tri}} \cdot \frac{1 - j\omega_{CL} \cdot \frac{T_{sw}}{4}}{1 + j\omega_{CL} \cdot \frac{T_{sw}}{4}} \cdot \frac{1}{R_s + j\omega_{CL} \cdot L_s} \cdot H \cdot K_{ADC} \quad (3-38)$$

which is equal to unity at desired crossover frequency. So,

$$K_P = \frac{V_{DC}}{V_{tri}} \cdot \frac{R_s}{K_{ADC}} \cdot \frac{1}{H} \cdot \sqrt{1 + \left(\omega_{CL} \cdot \frac{L_s}{R_s} \right)^2} \quad (3-39)$$

Then, the parameter K_I can be calculated from phase margin and can be expressed as

$$-180^\circ + PM = -90 - 2 \tan^{-1} \left(\omega_{CL} \cdot \frac{T_{sw}}{4} \right) - \tan^{-1} \left(\omega_{CL} \cdot \frac{L_s}{R_s} \right) + \tan^{-1} \left(\omega_{CL} \cdot \frac{K_P}{K_I} \right) \quad (3-40)$$

which yields

$$K_I = \frac{\omega_{CL} \cdot K_P}{\tan \left(-90 + PM + 2 \tan^{-1} \left(\omega_{CL} \cdot \frac{T_{sw}}{4} \right) + \tan^{-1} \left(\omega_{CL} \cdot \frac{L_s}{R_s} \right) \right)} \quad (3-41)$$

If the continuous time of current controller had been designed, the discretization strategy is used to transform the current controller into the Z-forms. There are several possible strategies, such as backward Euler, forward Euler, and Bilinear, which are based on numeral integration methods. This research uses backward Euler method, and the transformation is expressed as

$$s = \frac{1 - z^{-1}}{T_{sw}} \quad (3-42)$$

which is the substitution of s variable in the current controller transfer function with the indicated function of the z variable. So, the s -domain of PI controller can be transformed into

$$PI(z) = K_{P_dig} + \frac{K_{I_dig}}{1 - z^{-1}} \quad (3-43)$$

The parameters of digital current controller are given as

$$\begin{cases} K_{P_dig} = K_P \\ K_{I_dig} = K_I \cdot T_{sw} \end{cases} \quad (3-44)$$

Fig. 3.28 shows the block diagram of digital PI controller. It represents the parallel realization which is formulated as

$$D[k] = P[k] + I[k] \quad (3-45)$$

where the proportional term is

$$P[k] = K_{P_dig} \cdot e[k] \quad (3-46)$$

and the integral term is

$$I[k] = K_{I_dig} \cdot e[k] + I[k - 1]. \quad (3-47)$$

response closely follows current command. That is to say, the current is in phase with back-EMF and the overall efficiency is optimized. Besides, there are a 6 % reduction of RMS current and a 9 % reduction of peak current for comparing current-loop control with soft-commutation control at 4000 RPM. For 3000 RPM, there are a 8 % reduction of RMS current and a 17 % reduction of peak current. Obviously, the closed-loop current-mode control scheme has better efficiency than the soft-commutation control scheme.

However, due to the limitation of dc-link voltage, the current controller output will enter the non-linear region if the current command is too high. As shown in Fig. 3.32, when the fan motor accelerates over the 4000RPM, the controller output is limit by voltage source inverter, that is, closed-loop current control cannot provide the desired current response. Again, the current spike shows up at commutation boundary and the overall efficiency is reduced.

As mentioned before, when using the soft-commutation control scheme, the overall efficiency has significant improvement especially for high speed operation. Therefore, this research uses such advantage for reducing the current spike at high speed operation. In other words, once the fan motor accelerates over 4000RPM, the system will change its working mode from closed-loop current-mode control to open-loop voltage-mode soft-commutation control. Fig. 3.33 shows the improvement for introducing the soft-commutation control for high speed operation, the current spike has been reduced and the overall efficiency is promoted.

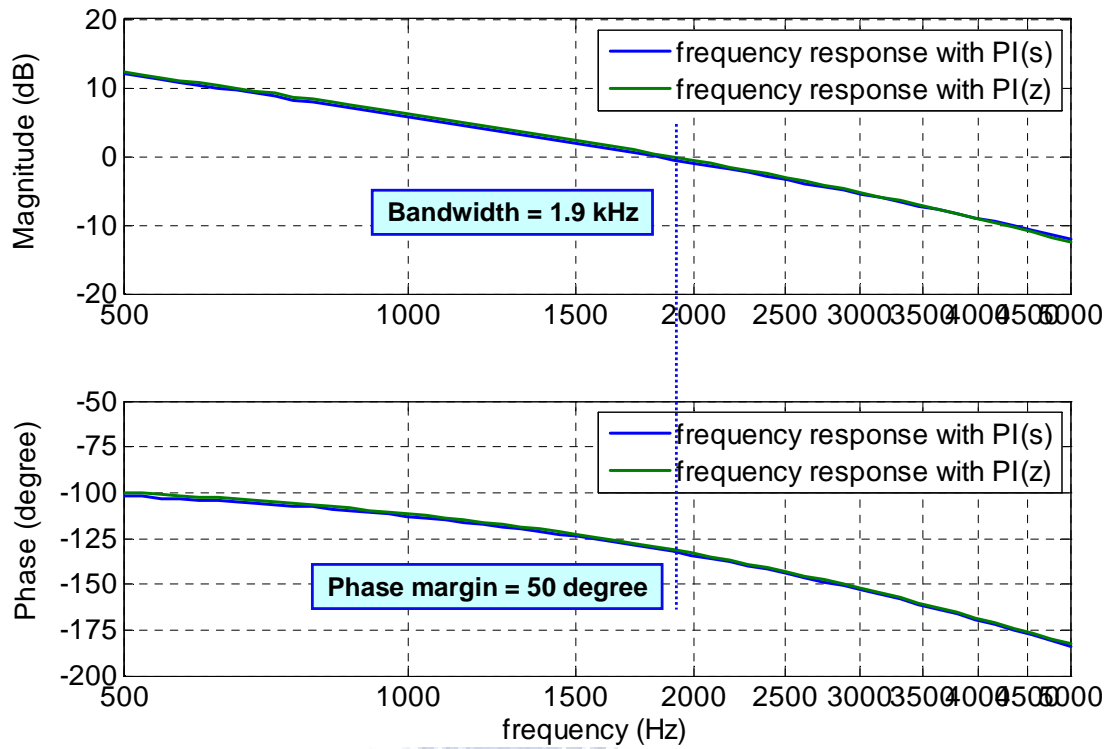


Fig. 3.29. Loop gain frequency response with PI(s) and PI(z).

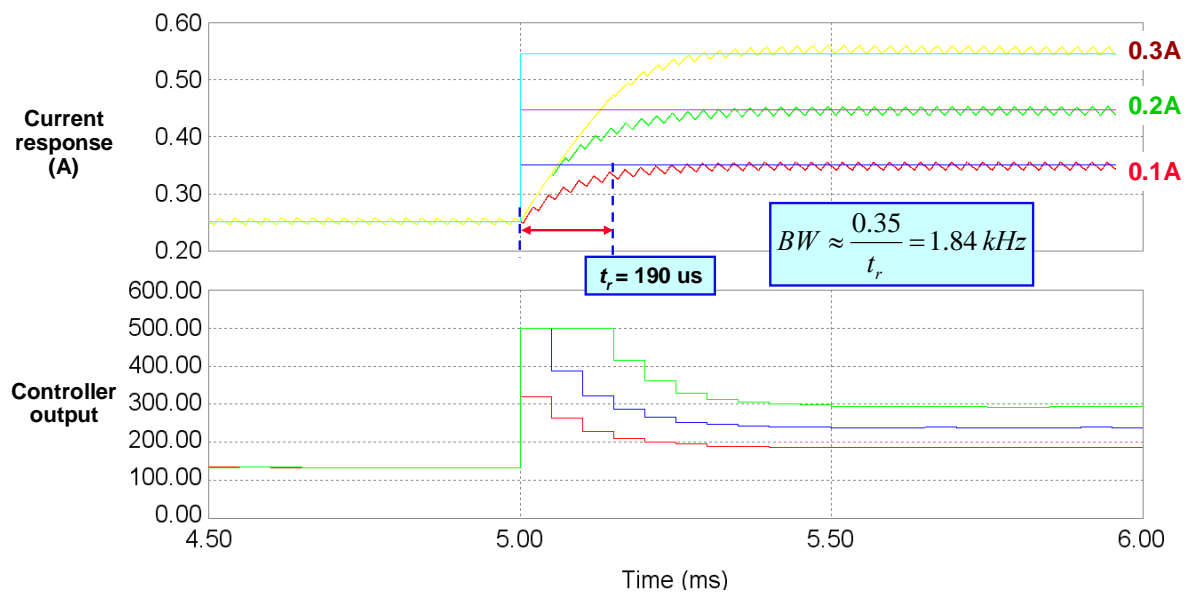
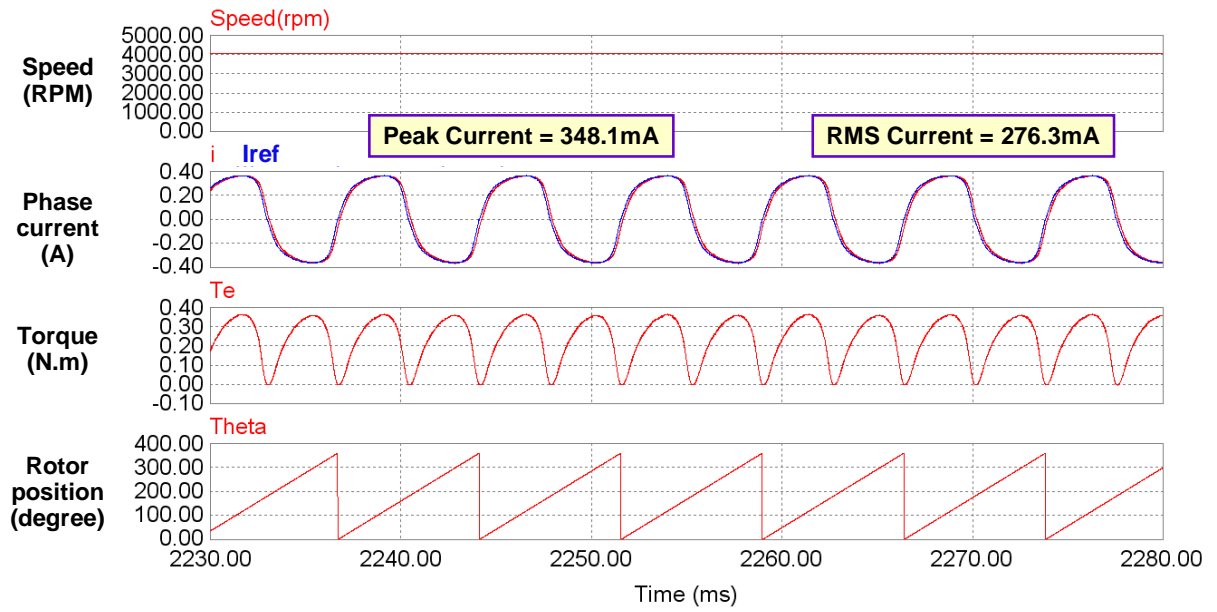
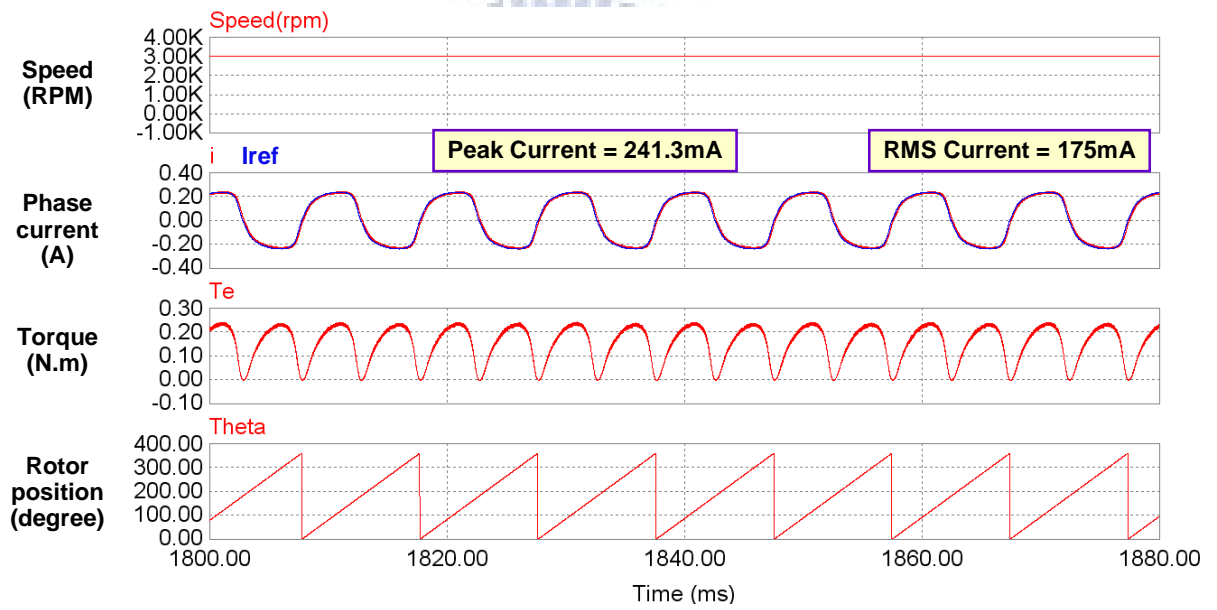


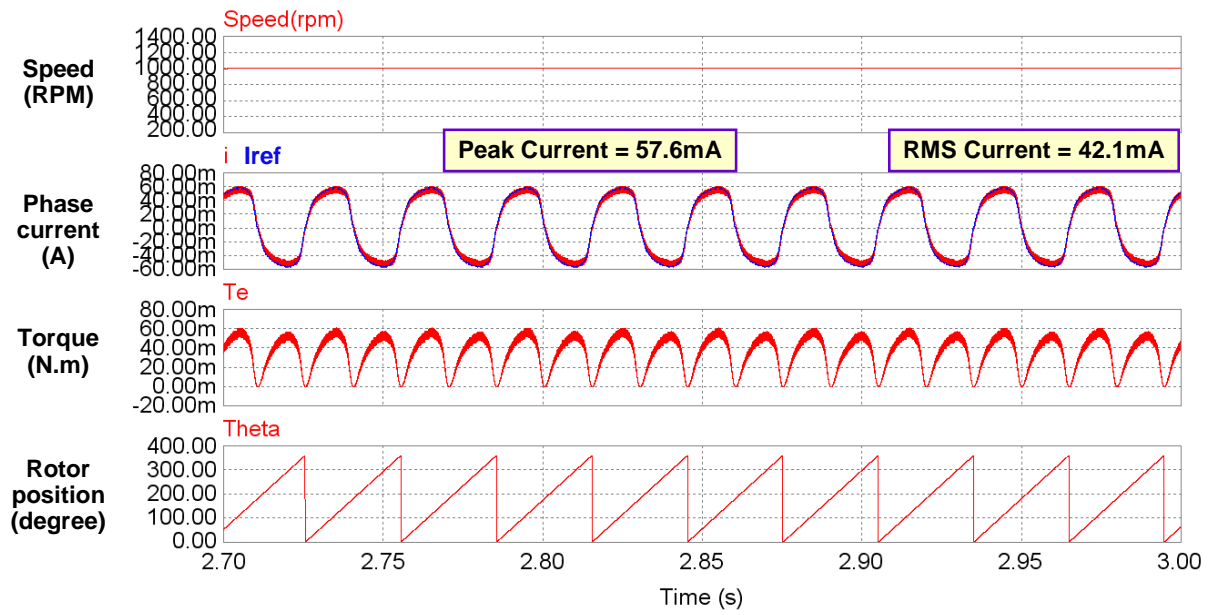
Fig. 3.30. Simulation result of step response at operation point of 250 mA.



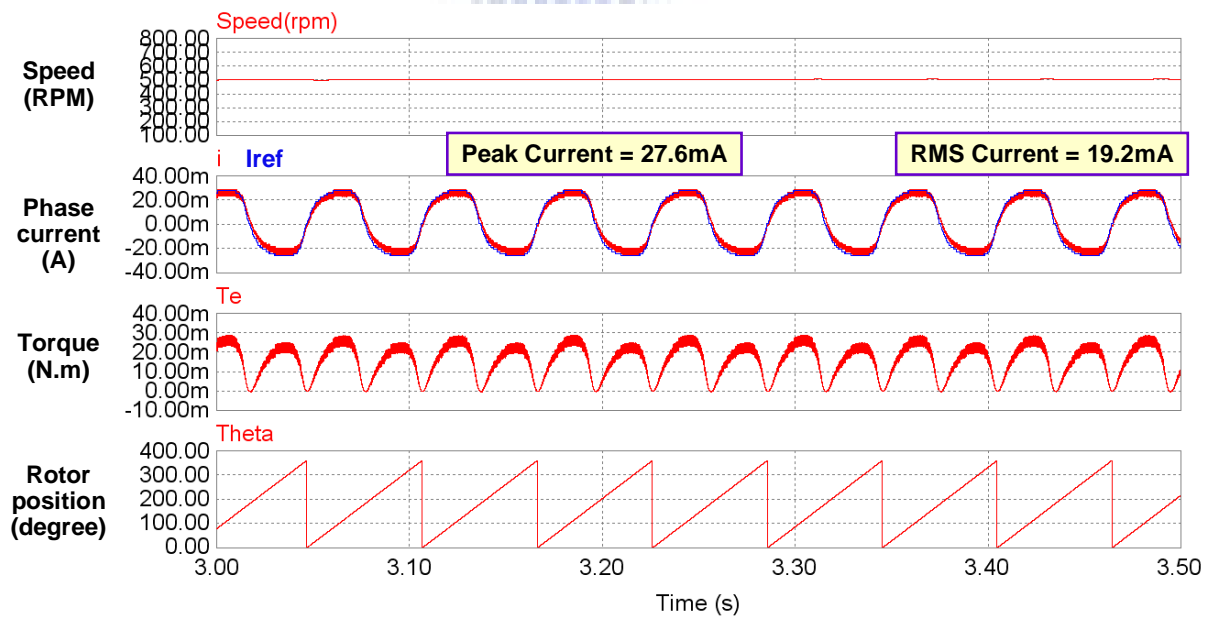
(a)



(b)



(c)



(d)

Fig. 3.31. Simulation results of steady-state response based on closed-loop current-mode control scheme (a) 4000 RPM, (b) 3000 RPM, (c) 1000 RPM, and (d) 500 RPM.

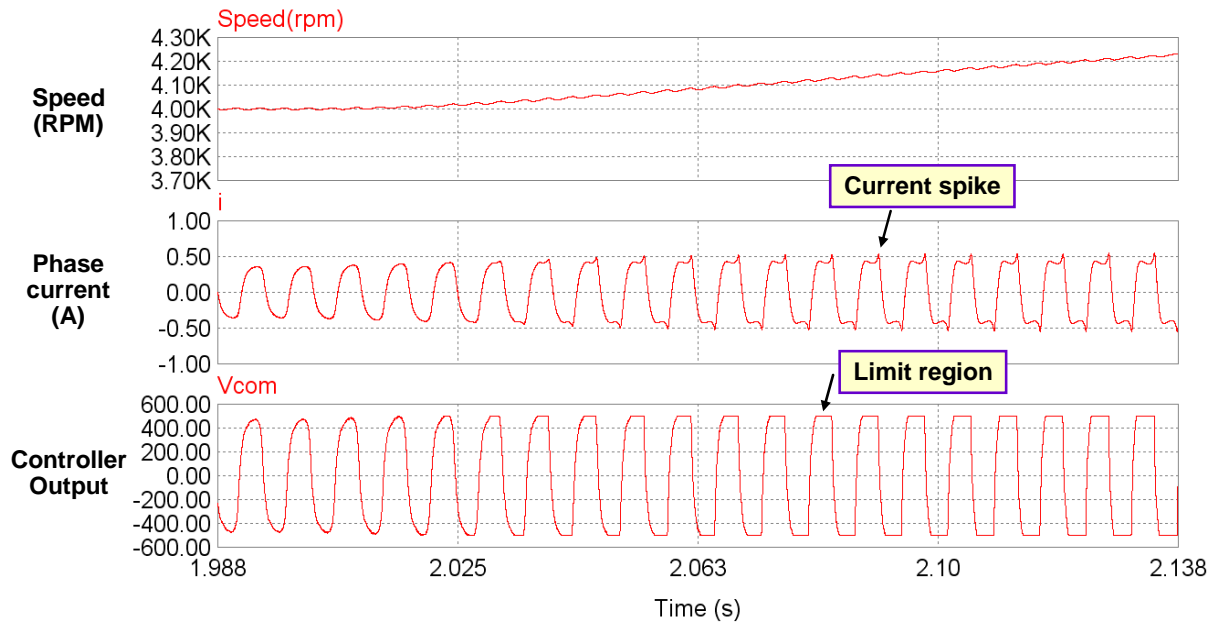


Fig. 3.32 The current-loop controller enters the limit region if the fan motor is over 4000 RPM.

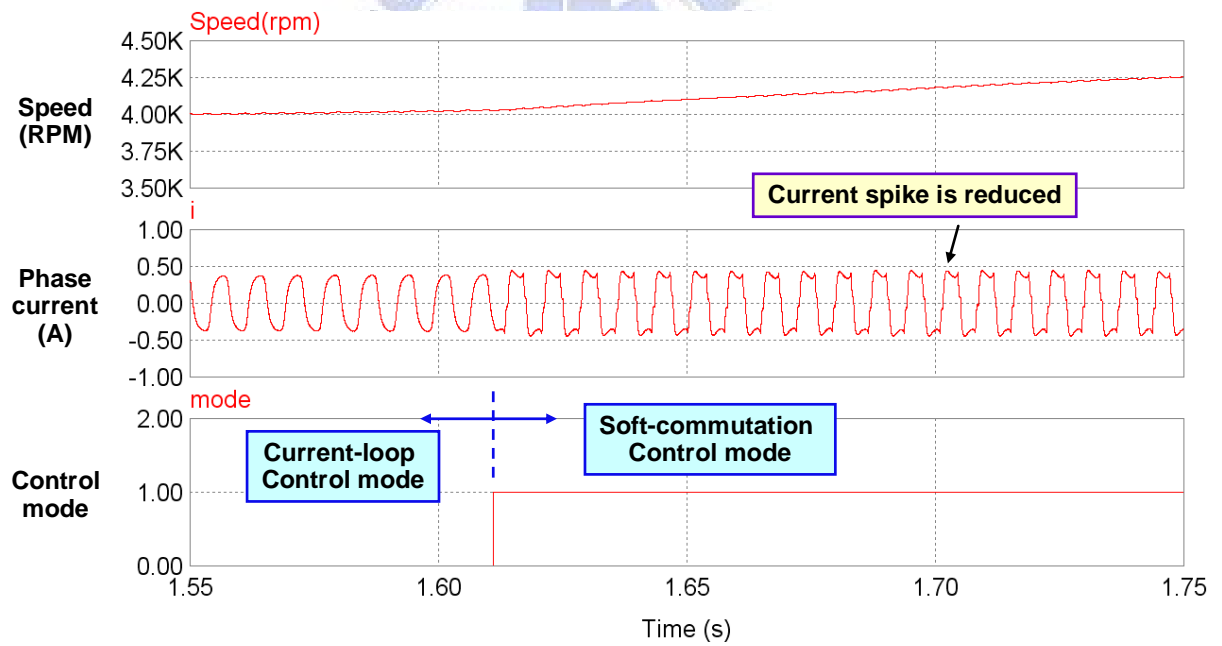


Fig. 3.33 If the fan motor accelerates over 4000RPM, the control system switches the control mode.

Chapter 4

Sensorless Control for Single-Phase BLDC Fan Motor Drives

The conventional BLDCM drive system requires Hall sensors or encoders to provide necessary information on rotor position and velocity. However, the Hall sensor is subjected to temperature variations, sensitive to magnetic noise, additional installation of the sensor and signal conditioning circuit, and unfitted for slim type fan motors. Therefore, in recently year, many sensorless techniques are presented to develop reliable and low cost control strategies for BLDCMs. However, the sensorless methods which are commonly used in three-phase BLDCM may be not suitable to drive single-phase BLDC fan motor due to the absence of floating phase, which can provide the information of back-EMF for current commutation. In this chapter, a sensorless control scheme called winding time-sharing is developed to drive the single-phase BLDC fan motor without Hall sensor.

4.1 SENSORLESS CONTROL SCHEME

4.1.1 Basic Operation Principle

For single-phase BLDC fan motors, the driving current should commute every 180 electrical angles to synchronize with the back-EMF. However, depending on previous chapter, in order to increase the utilization ratio of current, the soft-commutation control scheme with adjustable blanking time is introduced when the rotor is going to cross the commutation boundary. The sensorless control method is just based on this idea [32]-[33].

When the switches are turned off before the commutation boundary, the driving current will decrease to zero. The non-excited winding is not used to drive the motor, but it is served as a sensing component instead. The principle can be described as follow

$$v = L_s \frac{di}{dt} + iR_s + v_{emf} \quad (4-1)$$

where v is the terminal voltage of winding, R_s is the series resistance, L_s is the series inductance, v_{emf} is the back-EMF voltage. Once the driving current decreases to zero, the terminal voltage of winding is just the back-EMF. By detecting the winding terminal voltage, the control system can get the information of back-EMF easily, which will determine the direction of driving current in the next commutation.

Fig. 4.1 illustrates the operation waveforms of sensorless control method. It can be seen that the commutation cycle is divided to four intervals include T_1 , T_2 , T_3 and T_4 . During the period of T_1 , the power voltage is supplied to the motor, and the conducting time is just a little smaller than commutation cycle. At the end of T_1 , all the switches in the full-bridge inverter are turned off. Due to the motor inductance, the current will pass through the anti-parallel diode and decrease to zero little by little during the period of T_2 . During the period of T_3 , the current in the winding is zero and the motor rotates because of its inertia, and the terminal voltage of winding provides the information of back-EMF. If the back-EMF crosses zero-cross point (ZCP), and then system controls the switches of inverter for current commutation. However, in order to ensure the correct detection of the back-EMF ZCP, a short time T_4 is introduced to delay the current commutation.

During the period of T_3 , the system can get the information of the back-EMF by detecting the terminal voltage of the winding. It may find three possible relationships between the current and the back-EMF, as shown in Fig. 4.2, respectively. After current becomes zero, the system starts to detect the ZCP of back-EMF. If finding that the back-EMF has already

crossed ZCP, as shown in Fig. 4.2(a), the system considers that blanking time be too short and decreases T_1 for next commutation cycle. If the ZCP of back-EMF appears too late in the period of T_3 , as shown in Fig. 4.2(b), the system considers that blanking time is too long and increases conducting time for the following cycle. And if the ZCP of back-EMF occurs in proper period of T_3 , as shown in Fig. 4.2(c), controller considers that blanking time just be the right value and keeps unchanged for the following control. In other words, introducing the adjustable blanking time can improve the performance of sensorless technique and increase the utilization ratio of current.

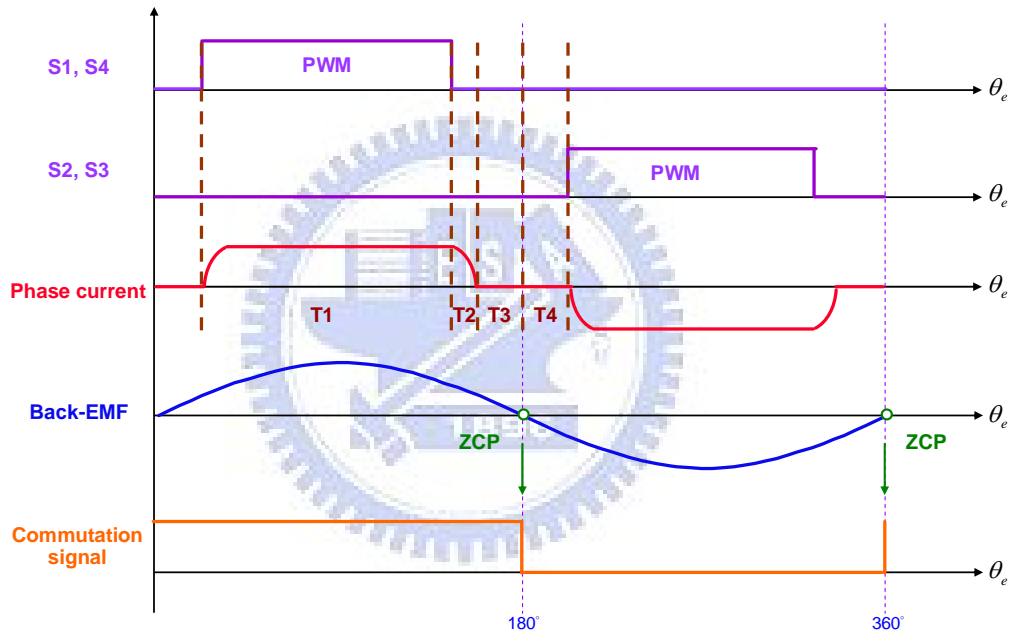


Fig. 4.1. Operation waveform of sensorless control method.

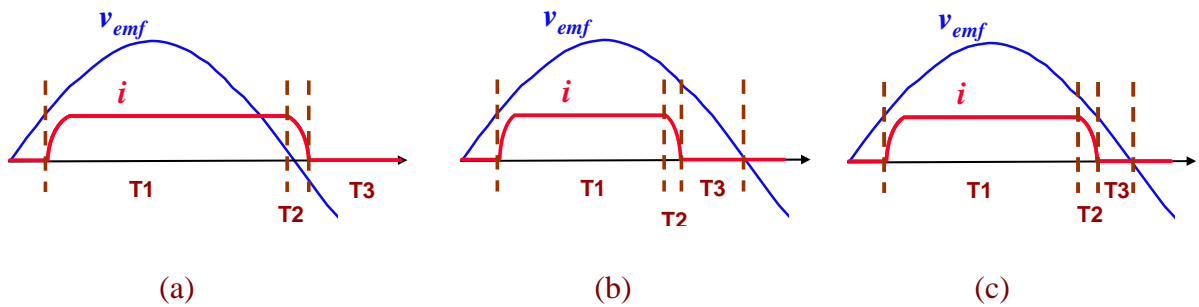


Fig. 4.2. Three possible relationships between the phase current and the back EMF.

4.1.2 Zero-Crossing Point of Back-EMF Detection

Based on sensorless control method, the system can get the information of the back-EMF directly and give its control strategy of the next commutation cycle. So, the key to sensorless control method is detecting zero-crossing point (ZCP) of back-EMF. Because of the winding inductance, the polarity of the phase current cannot be changed instantaneously, so the current will pass through the anti-parallel diode. This will cause to a level shift of phase voltage which is an error signal for sensing phase voltage to detect ZCP of back-EMF. Therefore, the control system should not detect the ZCP until the current decrease to zero. In this research, a time-delay process is used to mask such undesirable signal. From chapter 3, the larger diode current is, the longer masking time is necessary. Fig. 4.3 shows the operation waveform for back-EMF ZCP detection. Because the diode is conducting, the phase voltage becomes level shift. There is a sufficient masking time is utilized to prevent such error signal, and then sampling the non-excited voltage for ZCP detection.

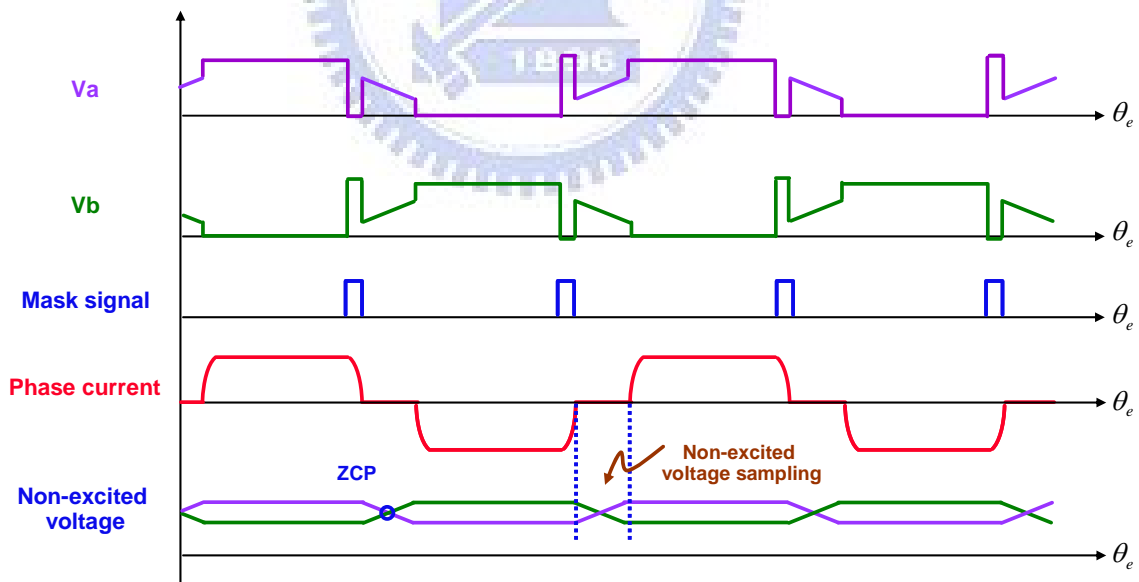


Fig. 4.3. Operation waveform for back-EMF ZCP detection.

4.2 SENSORLESS START-UP STRATEGY

The common problem associated with the sensorless motor drive is the start-up performance. Most sensorless control methods are based on back-EMF, however, when motor is at standstill or low speed, the back-EMF is too small to make precise rotor position estimation. Moreover, especially for single-phase BLDC fan motor, it has only one phase winding, so the induced stator field is just two opposite directions which is different to three-phase BLDCM. So, the other critical problem is the rotor initial position is unknown without Hall sensor, and it is difficult to rotate in the predefined direction when the fan motor is starting. To solve these problems, this research develops the specific strategy to realize start-up in predefined direction no matter where the initial rotor position is. After the motor is running in the required direction, the system adopts open-loop control called kick-off to speed up the fan motor. Once the motor reaches a speed at which back-EMF is sufficiently accurate, and then the control system is switched to the sensorless mode.

4.2.1 Starting Method Based on Asymmetric Air Gap

As mentioned before, the single-phase BLDC fan motor with asymmetric air gap can avoid starting dead point. This research develops the starting method based on such feature to ensure the motor run in one direction [36]-[38]. In this fan motor model, the right air gap is made larger than the left air gap. So, when motor keeps standstill, the rotor position has two possibilities as shown in Fig. 4.4. Here, the starting method illustration is based on the simplest motor model just with two stator slots and two permanent magnet poles. Besides, it is supposed that the slot A1 is south polarity and the other of A2 is north polarity while supplying a positive current pulse to the motor winding. Conversely, when a negative current pulse is supplied to the winding, the polarity of A1 and A2 will exchange each other.

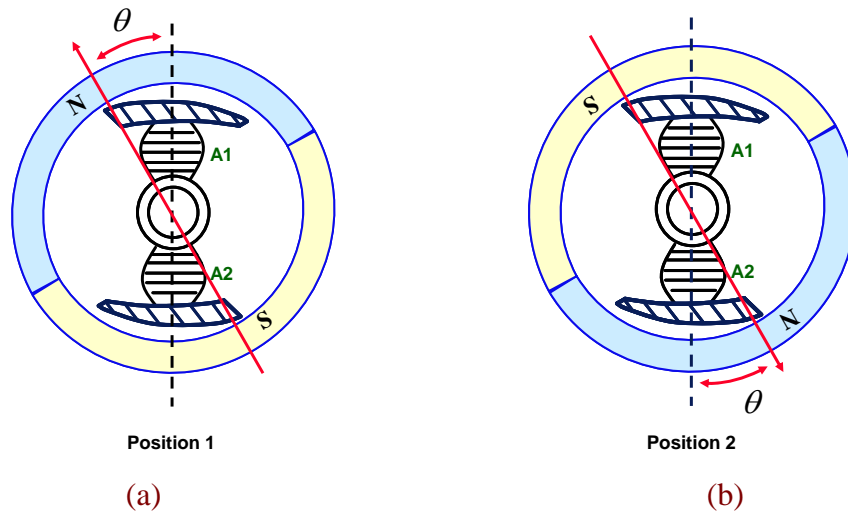


Fig. 4.4. Two possible rotor positions when motor is standstill.

If the rotor initial position is Position 1, as shown in Fig. 4.4(a), it will rotate in counterclockwise direction when a positive current pulse is supplied to the winding, as shown in Fig. 4.5(a). Once the current pulse keeps on, the rotor will rotate an electrical angle of $\pi - \theta$ degrees, and then stop after vibrating for a moment. Fig. 4.5(b) illustrates the rotor position during this procedure. It shows that the rotor stops at zero position after t_1 , then the control system lets the current decrease to zero immediately at t_2 , the rotor yields a counterclockwise rotation, and eventually offsets an electrical angle of θ degrees and stops at Position 2 due to asymmetric air gap. However, if the rotor initial position is Position 2, it will rotate in clockwise direction for an electrical angle of θ degrees, and stops at zero position when a positive current pulse is supplied to the winding, as shown in Fig. 4.6(a). Fig. 4.6(b) shows that the rotor stops at zero position after t_1 , then the control system lets the current decrease to zero immediately at t_2 . The asymmetric air gap leads the rotor in counterclockwise rotation, and eventually offsets an electrical angle of θ degree and stops at Position 2. In other words, the rotor will stop at Position 2 in spite of initial position when positive current pulse is supplied. Similarly, if control system uses a negative current pulse to excite the winding, the rotor will stop at Position 1 in spite of the rotor initial position, as shown in Fig. 4.7 and Fig. 4.8.

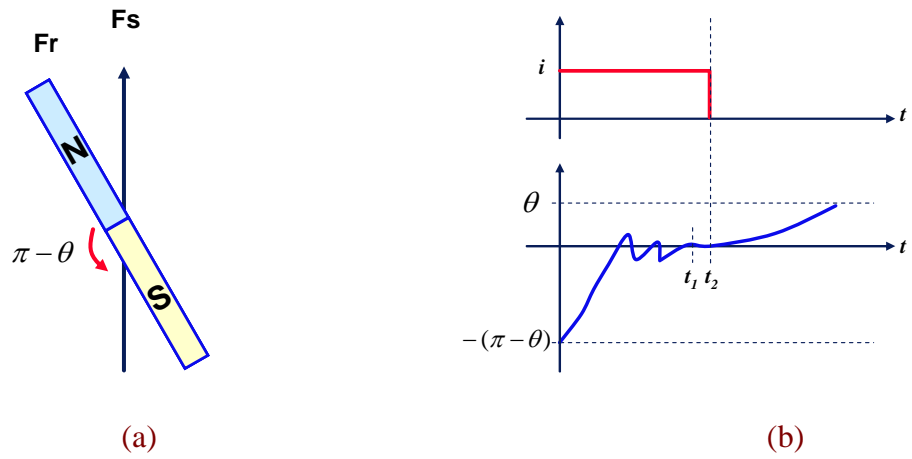


Fig. 4.5. Motor state while positive current pulse is supplied at Position 1.

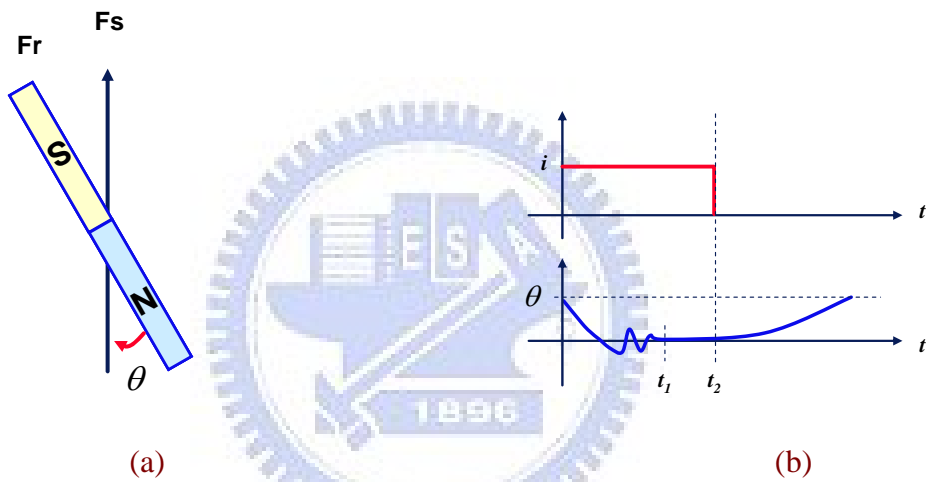


Fig. 4.6. Motor state while positive current pulse is supplied at Position 2.

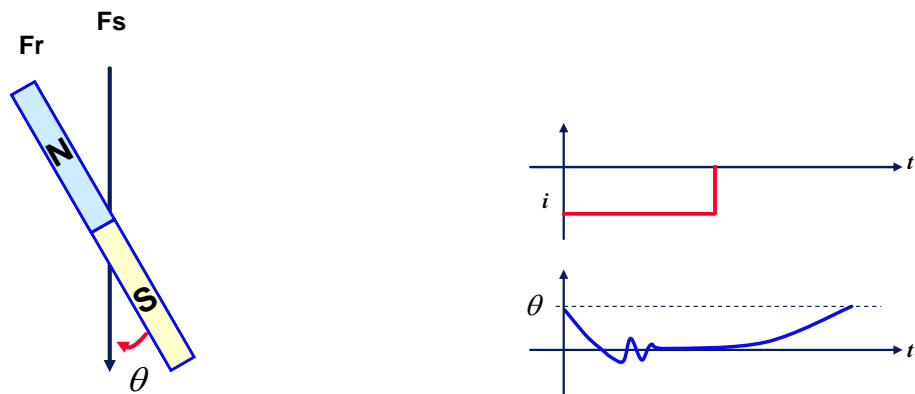


Fig. 4.7. Motor state while negative current pulse is supplied at Position 1.

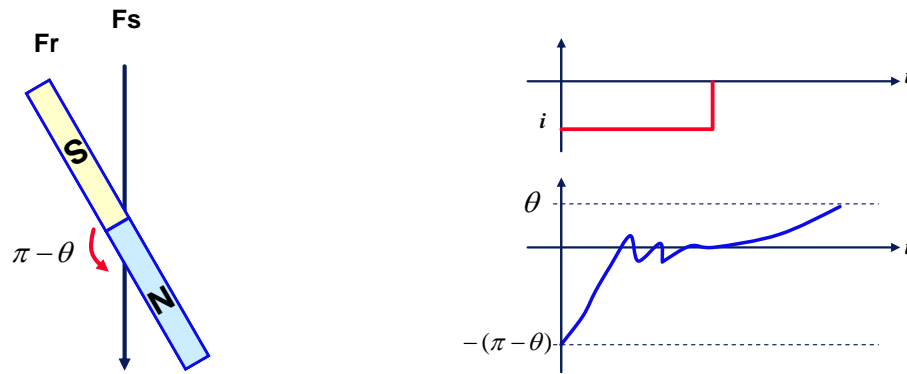


Fig. 4.8. Motor state while negative current pulse is supplied at Position 2.

So far, the above tells that the rotor stops at the special position determined by the polarity of the current pulse. After such rotor alignment process, it ensures that the motor rotates in counterclockwise direction if opposite polarity of the current pulse is applied in next control step. For example, if control system uses a positive current pulse to align the rotor at Position 2 in spite of the rotor initial position, then a negative current pulse excites the winding to let rotor yield counterclockwise rotation. Therefore, the key of this method is the time length of the current pulse. The criterion is that time of effective current should be long enough to align the rotor toward zero position, and time of zero current is also long enough to offsets the rotor position due to asymmetric air gap.

4.2.2 Start-Up Procedure

The sensorless control scheme based on the back-EMF detection can work properly when operating at medium to high speed. However, the measured signal is too small to make precise position estimation when the motor is at standstill or low speed. Therefore, after the rotor alignment process, next control step should accelerate the motor to a certain speed which sensorless algorithms can work reasonably.

Fig. 4.9 shows the control steps to start-up the single-phase BLDC fan motor without Hall sensor. The first step is called align which ensures the rotor to rotate in predefined direction. That is, the positive current pulse is supplied to the winding while switch S1 and S4

are conducting, and the rotor will align toward zero position. After turning off the switches let the current decreases to zero, the rotor will offset a specific electric angle which is related to asymmetric air gap. The next control step is called kick-off, it means that a short but strong current pulse excited the winding to push the motor from stop to rotate. If the current pulse is strong enough, the motor will speed up to a certain speed which back-EMF is sufficiently accurate for sensorless algorithm. So, the terminal voltage can serve as sensing component to detect the back-EMF during the resting time of kick-off, and then the control system is switched to the sensorless mode. The speed response during sensorless start-up procedure is shown in Fig. 4.10. However, it should be noted that the different motor needs different magnitude of current pulse to start the motor. Fortunately, the single-phase BLDC fan motor has small inertia, and it is easy to accelerate the motor to a desired speed. Also, thanks to the programmability of the microcontroller, the control system is convenient to adjust the parameters for different applications.

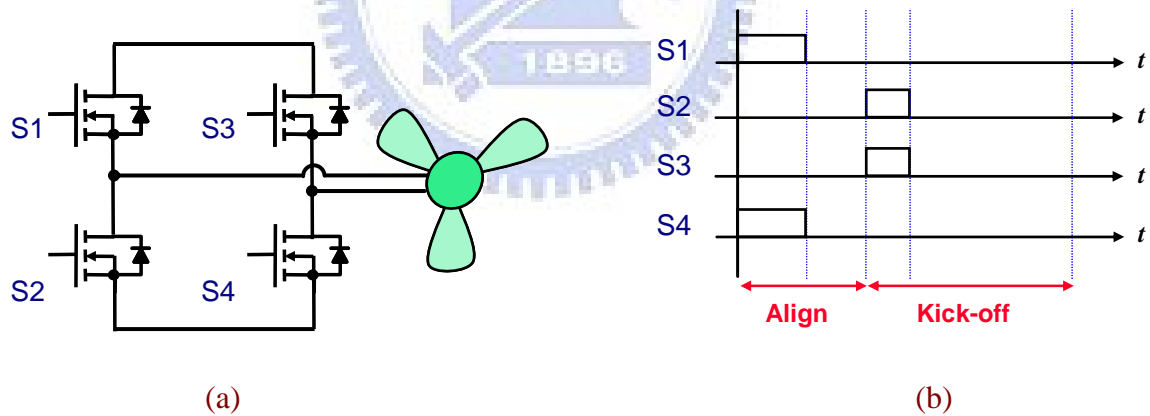


Fig. 4.9. Sensorless start-up control steps for single-phase BLDC fan motors (a) inverter circuit and (b) control steps.

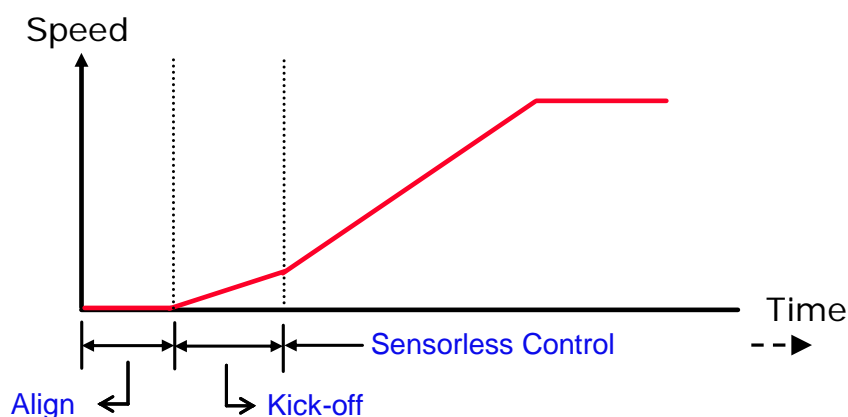


Fig. 4.10. Speed response during sensorless start-up procedure.

4.2.3 Open-Loop Voltage-Mode Control without Hall sensor

According to the above description, the block diagram of open-loop voltage-mode sensorless control for single-phase BLDC fan motor is shown in Fig. 4.11. The phase voltage is sampled for detecting the ZCP of back-EMF to produce a sequence of commutation signal. There is a mode selector to switch the start-up mode and sensorless mode. These commutation signals are used to estimate the motor speed and to determine the conducting time and the direction of driving current. Fig. 4.12 shows the fan motor smoothly starts without Hall sensor, and the start-up time is approximately 0.3 seconds. Then, the fan motor is switched to the sensorless mode, and eventually accelerates to 4000 RPM. Fig. 4.13 shows the steady state waveform of sensorless control at 4000 RPM. When the current decreases to zero, the non-excited voltage is equivalent to back-EMF voltage, and ZCP detection produces the commutation signal for controlling the next commutation cycle. Similarly, Fig. 4.14 shows the simulation result of start-up procedure from standstill to 1000 RPM, and Fig. 4.15 shows the steady state waveform when the fan motor is operated at 1000 RPM.

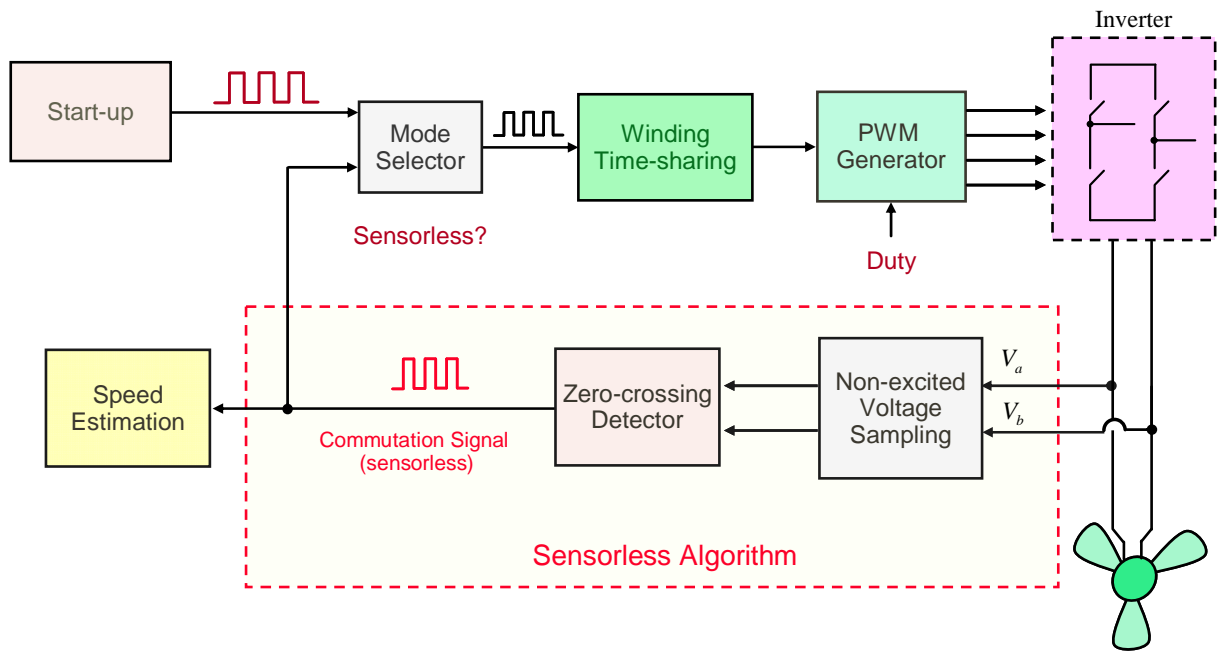


Fig. 4.11. Block diagram of open-loop voltage-mode sensorless control for single-phase BLDC fan motor.

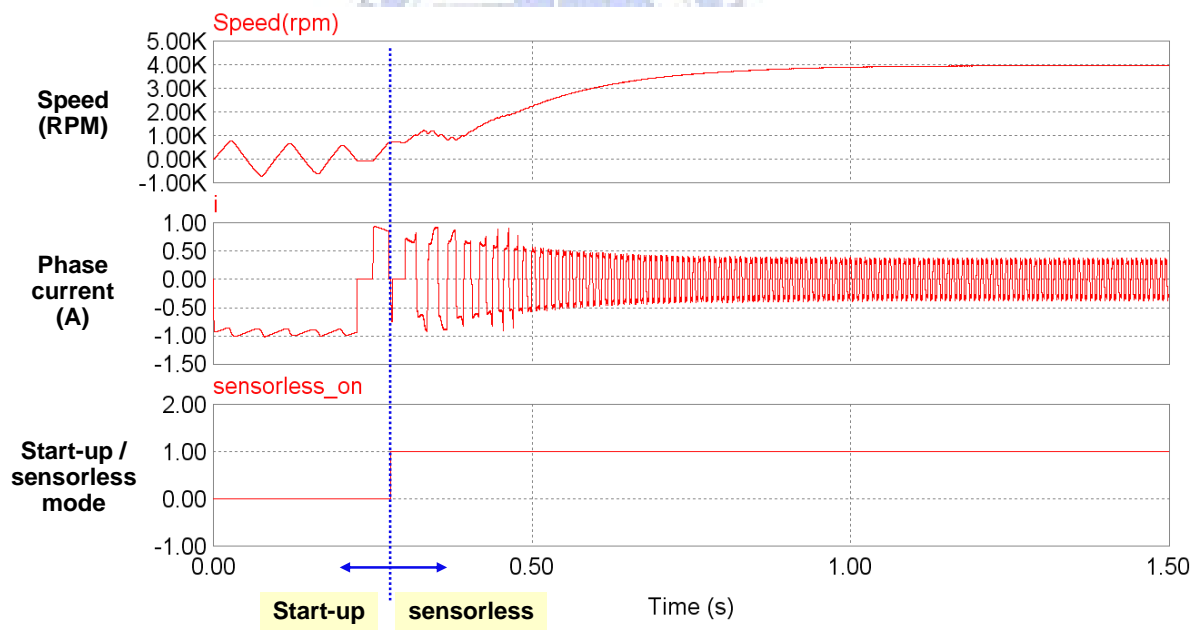
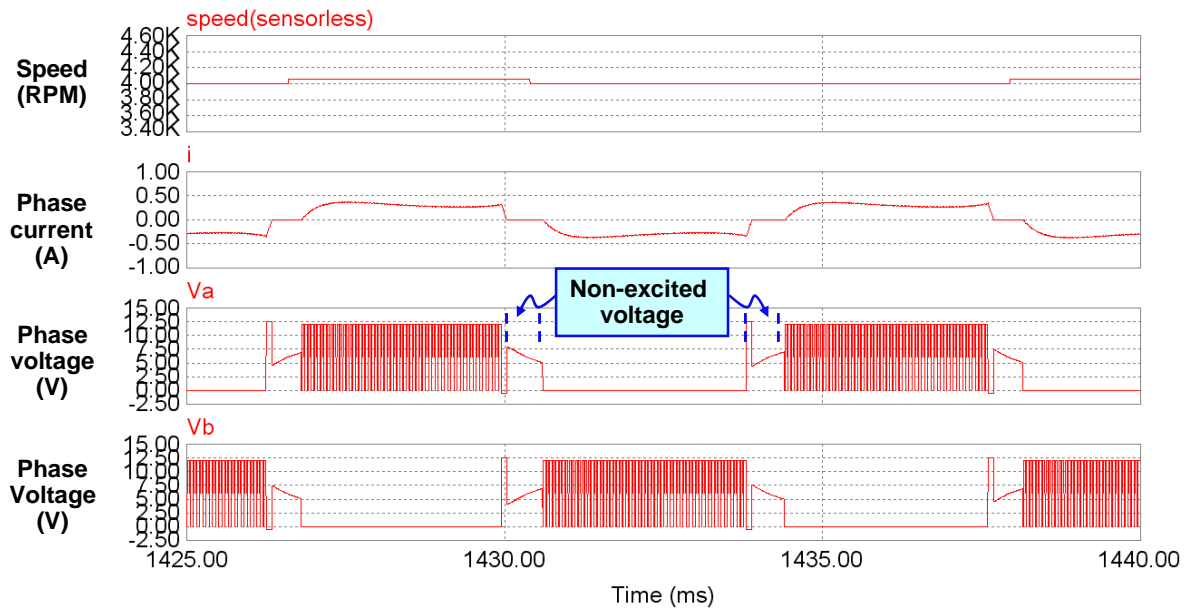
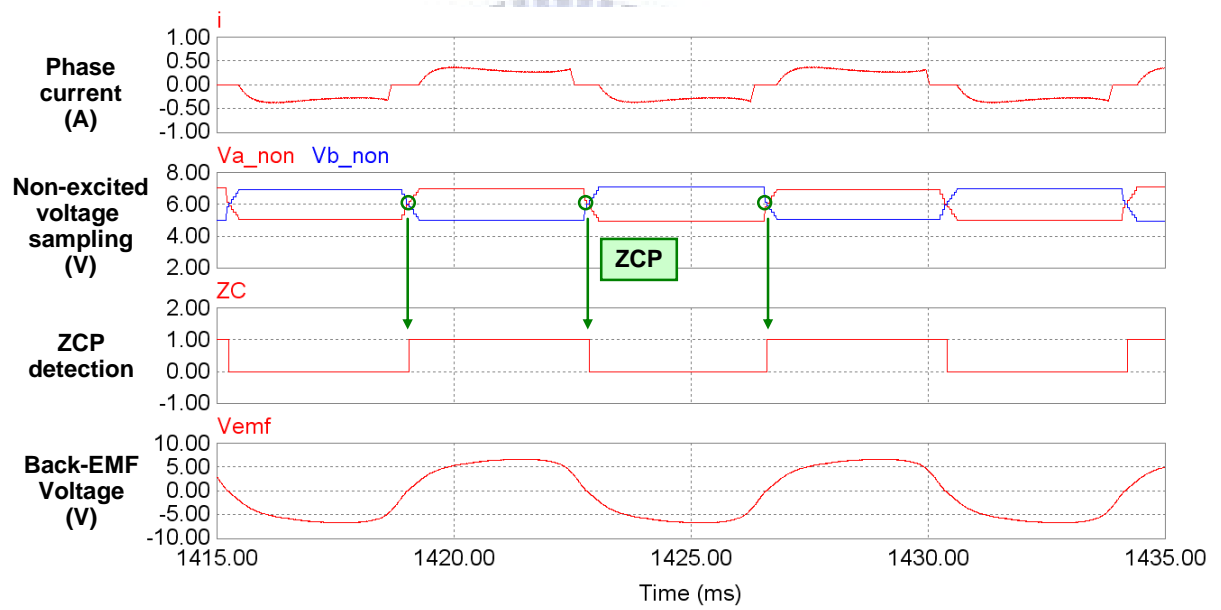


Fig. 4.12. Sensorless start-up control from standstill to 4000 RPM.



(a)



(b)

Fig. 4.13. Simulation results of sensorless control at 4000 RPM (a) steady state waveforms of phase current and phase voltage and (b) Non-excited voltage sampling and ZCP detection.

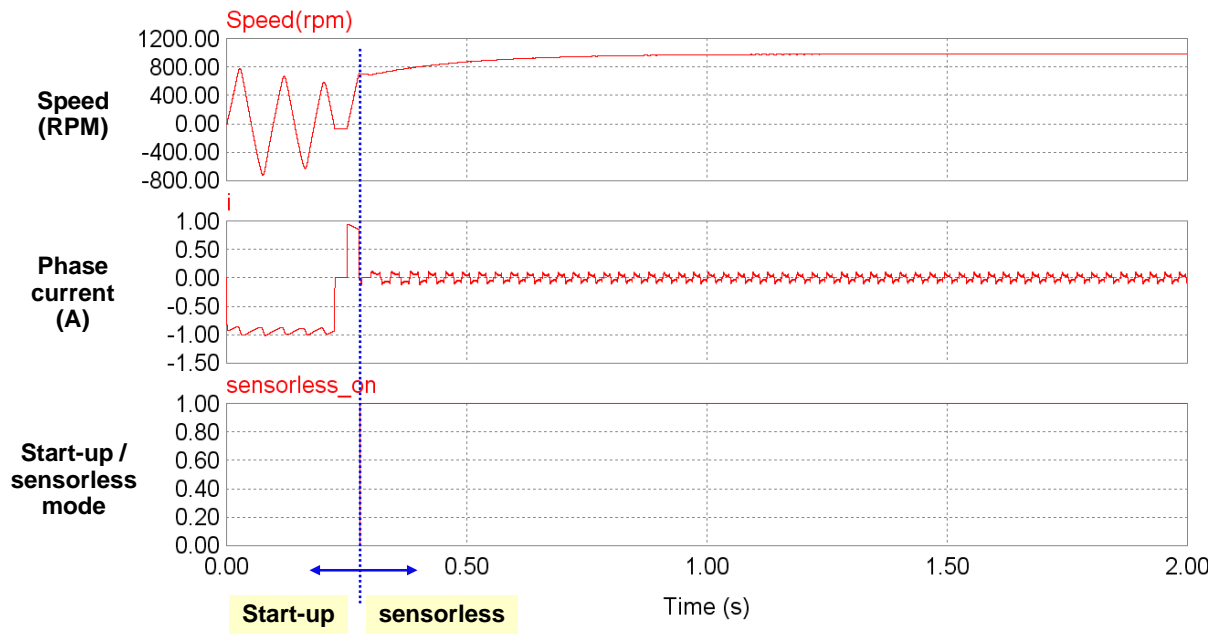
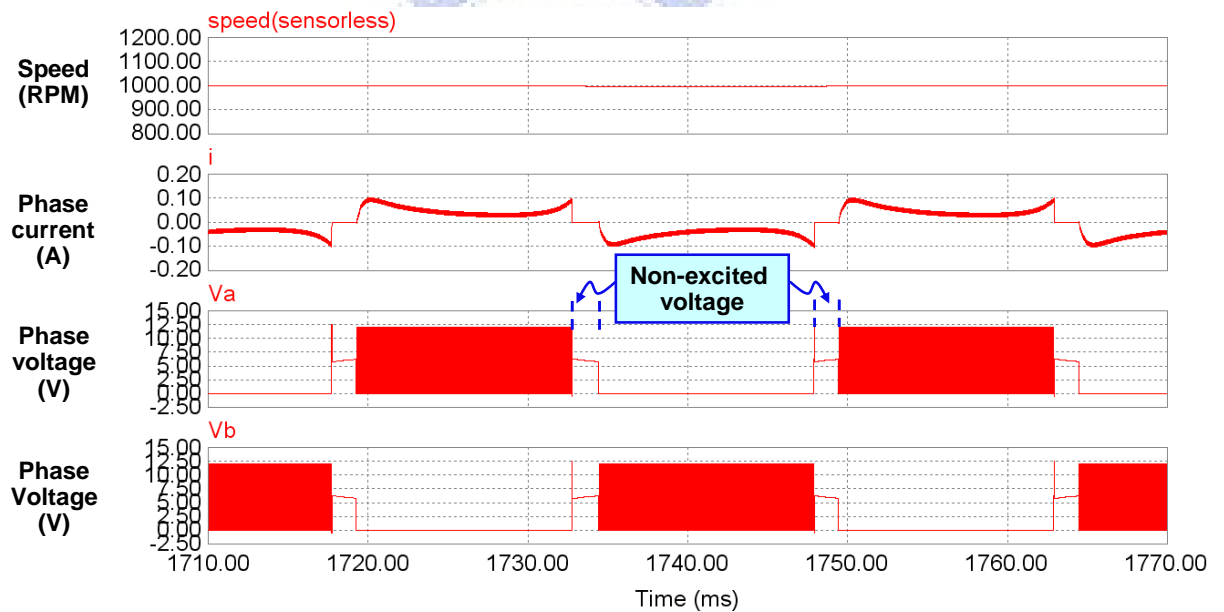
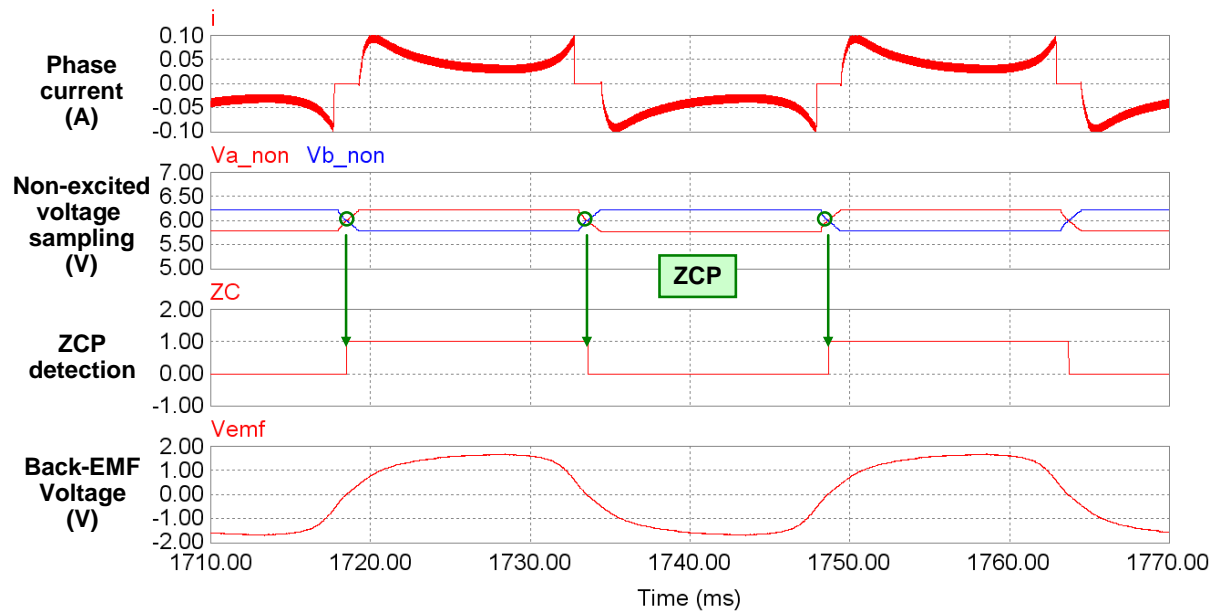


Fig. 4.14. Sensorless start-up control from standstill to 1000 RPM.



(a)



(b)

Fig. 4.15. Simulation results of sensorless control at 1000 RPM (a) steady state waveforms of phase current and phase voltage and (b) Non-excited voltage sampling and ZCP detection.

4.3 CLOSED-LOOP CURRENT-MODE CONTROL OF SENSORLESS MOTOR DRIVE

4.3.1 System Configuration

The research goal of this section is to design a high efficiency and low cost of sensorless control system for single-phase BLDC fan motors. Fig. 4.16 shows block diagram for closed-loop current-mode control of sensorless driving system, it contains all the blocks, such as PWM modulation, sensorless algorithm, current-loop controller and start-up control scheme. The system has an analog-to-digital (A/D) converter to sample the phase voltage and phase current, the former is used for sensorless algorithm and speed estimation, and the later is used for current-loop control. The torque command is multiplied by the estimated Hall sensor signal to produce phase current reference. The current controller determines the value of the switch duty ratio based on error between the reference and actual current, and then, the PWM generator outputs corresponding waveform to control the switches.

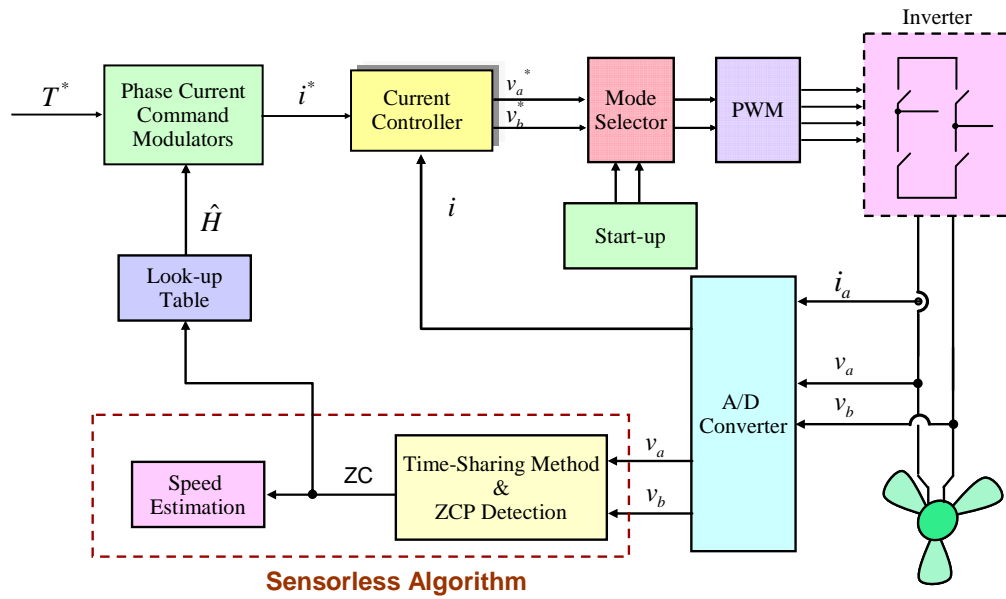


Fig. 4.16. Block diagram of sensorless control system with closed-loop current-mode control.

It should be noted that the estimated Hall sensor signal is an approximate back-EMF waveform which is produced from a table. Due to absence of linear Hall sensor feedback, the current multiplier control scheme needs a predefined current waveform to produce current command. In order to promote the overall efficiency, the predefined waveform should be identical with back-EMF. Therefore, building up the table in term of flux distribution is necessary for closed-loop current-mode control scheme without linear Hall sensor, as shown in Fig. 4.17.

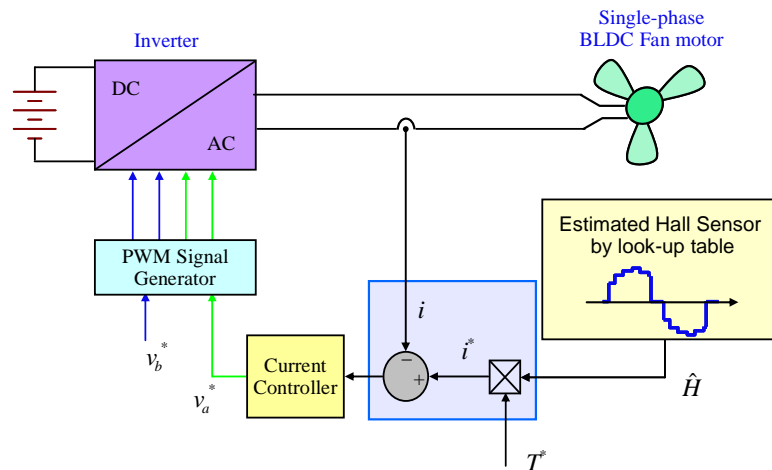
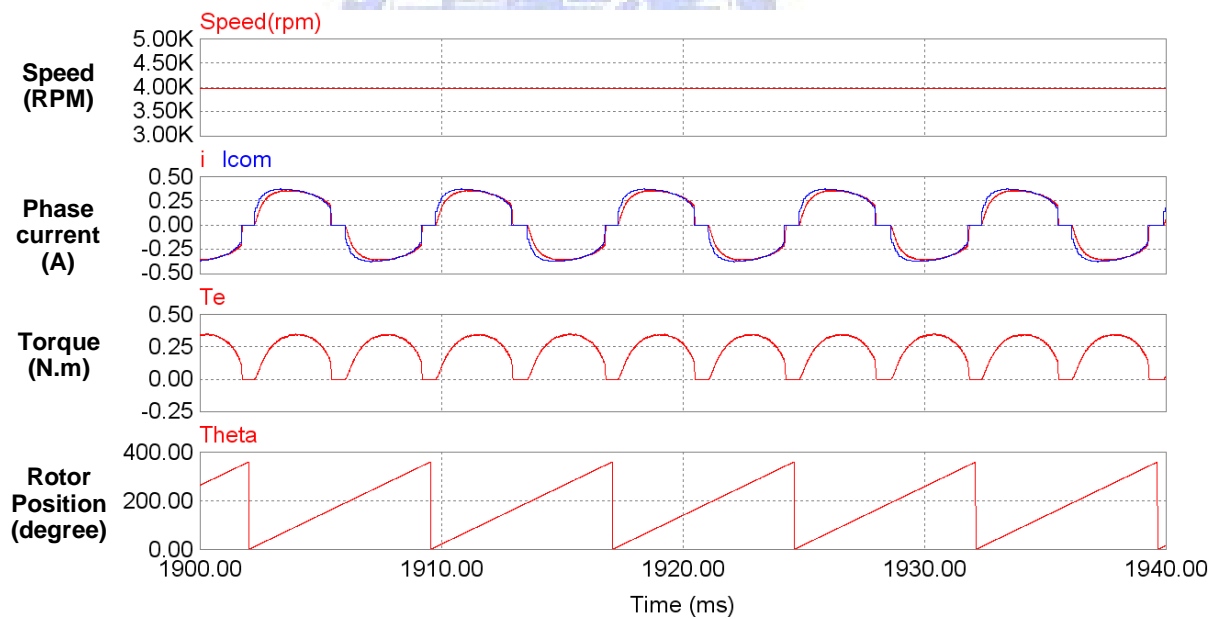


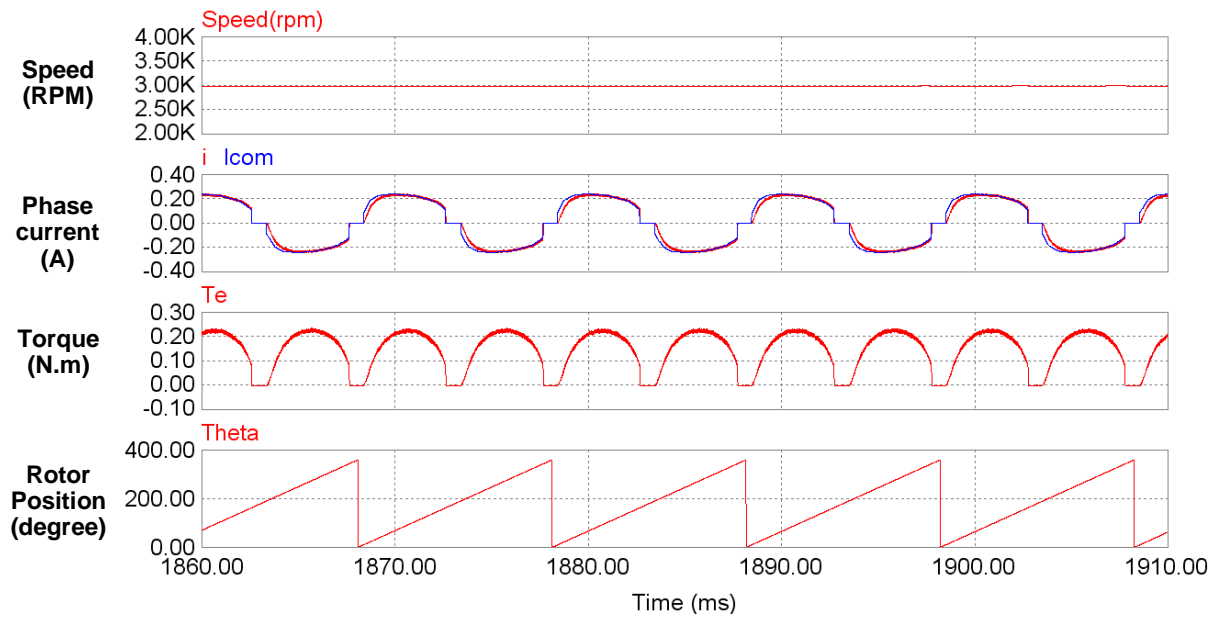
Fig. 4.17. Current multiplier control scheme with estimated Hall sensor by look-up table.

4.3.2 Analyses of Simulation Results

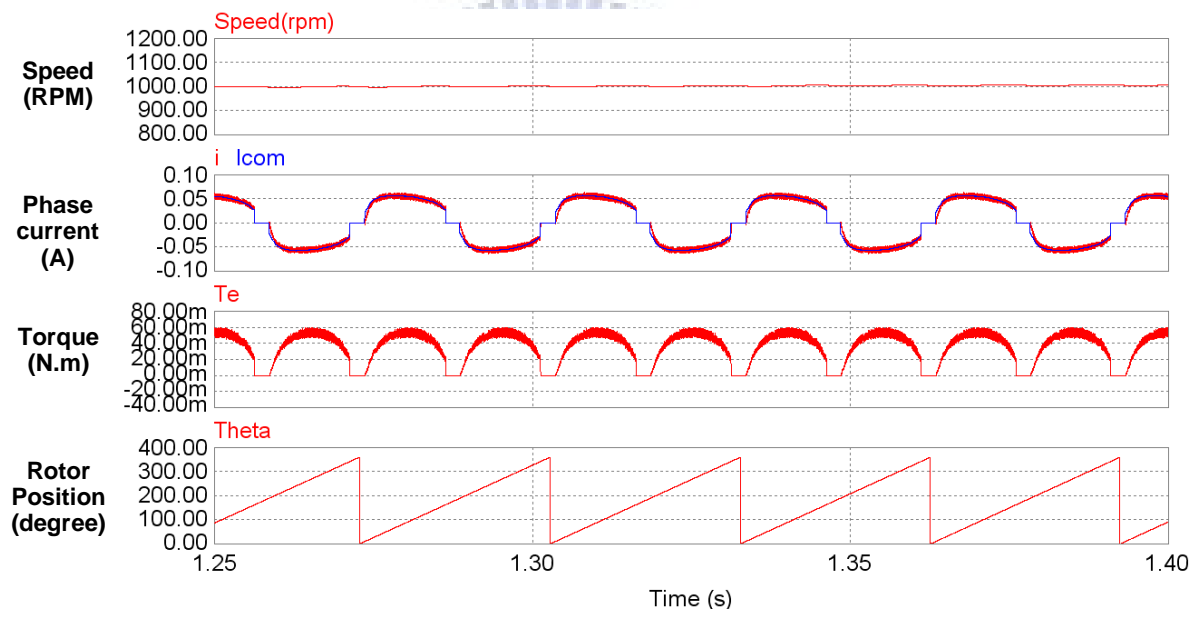
The current-loop sensorless control scheme can be verified by computer simulation with proposed model. Fig. 4.18 shows the simulation results of current-loop control at different speed operation. It can be seen that the current spike at commutation boundary has been removed, and the current response closely follows current command. Besides, by look-up table of back-EMF, the current waveform retains the characteristic of corresponding back-EMF. From the theory in Chapter 3, this will significantly improve the overall efficiency. Fig. 4.19 shows the statistics curves for RMS value and peak value of phase current with different control schemes. For entire speed control range, both of RMS value and peak value is lower when using closed-loop current-mode control. That is to say, the closed-loop current-mode control of sensorless motor drive is a low cost and high efficiency solution for single-phase BLDC fan motors.



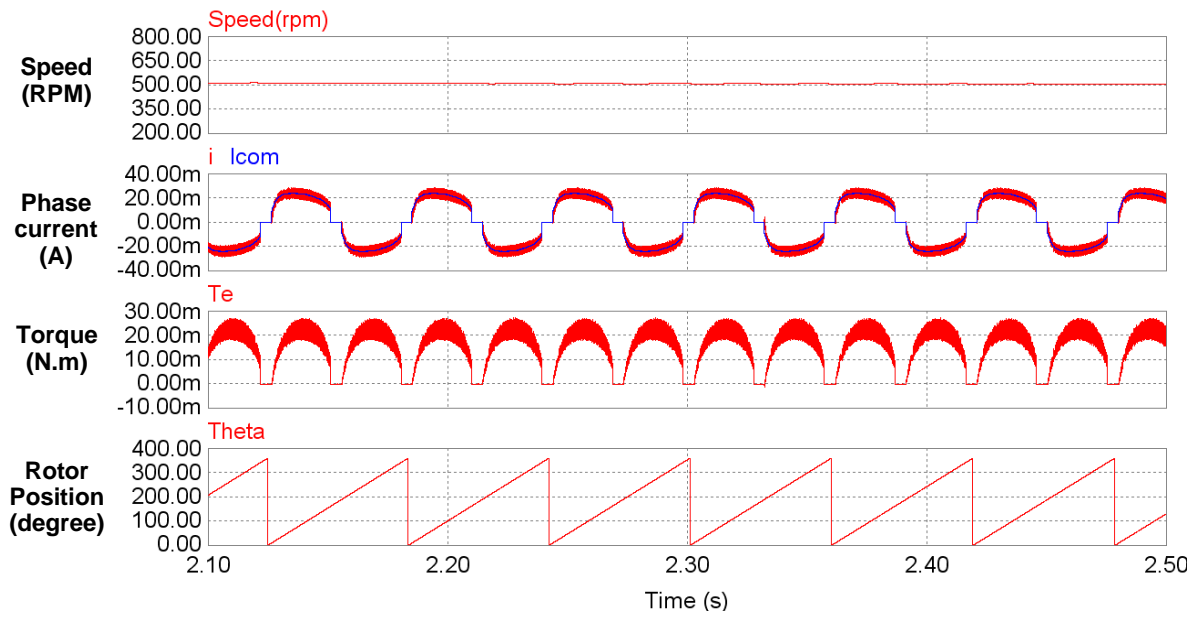
(a)



(b)

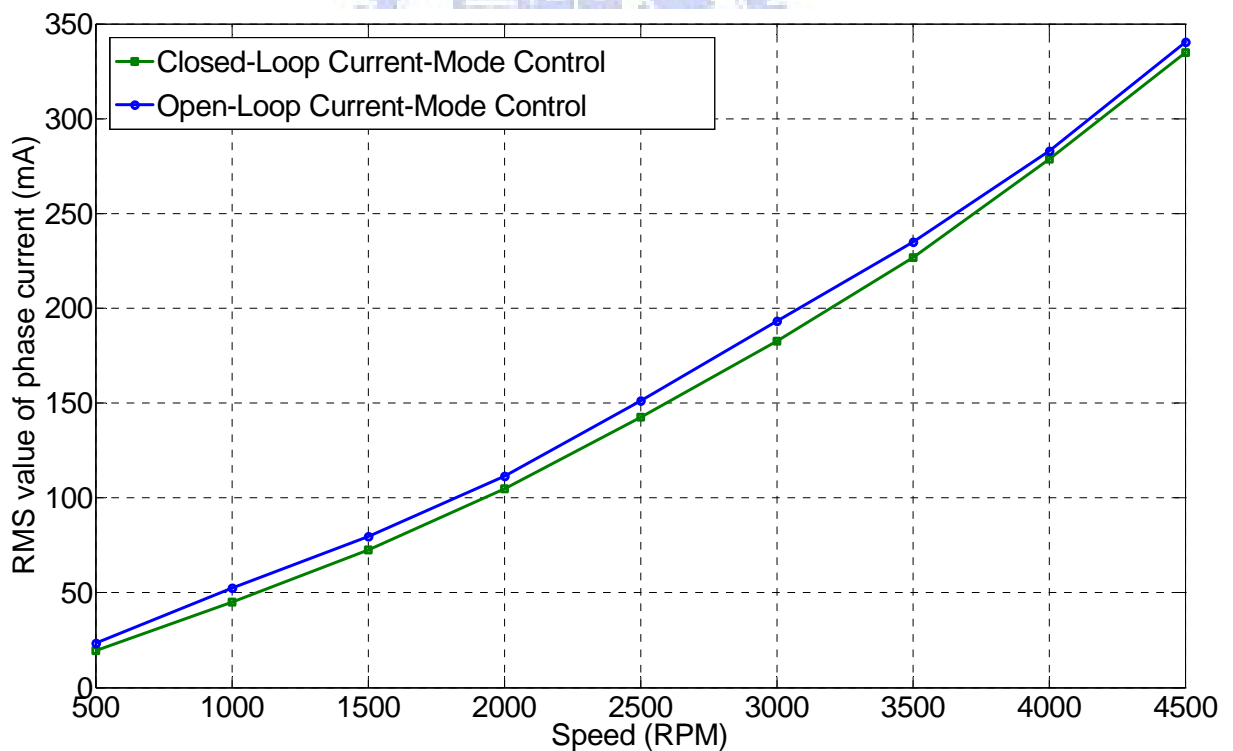


(c)

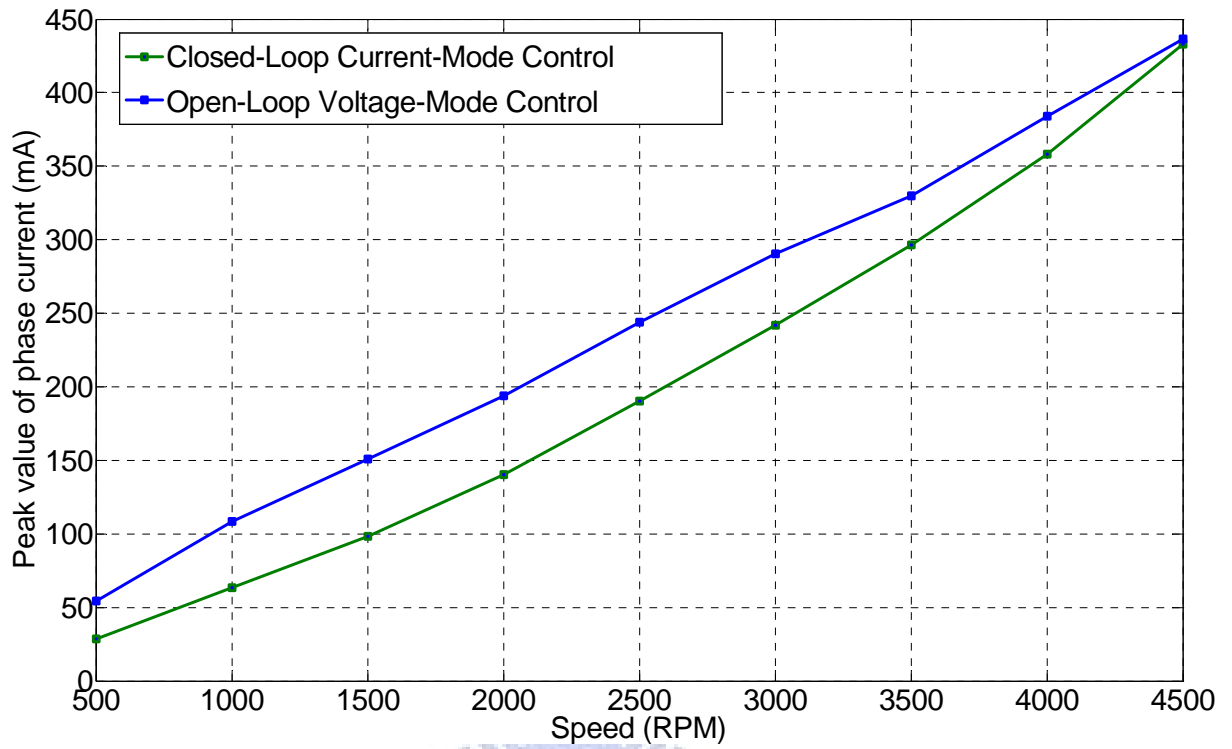


(d)

Fig. 4.18. Simulation results of current-loop control at different speed operation (a) 4000 RPM, (b) 3000 RPM, (c) 1000 RPM, and (d) 500 RPM.



(a)



(b)

Fig. 4.19. Statistics curves for different control schemes (a) RMS value of phase current and (b) peak value of phase current.

Chapter 5

Laboratory Setup and Implementation of Single-Phase BLDC Fan Motor Control System

Owing to the rapid progress in motor control, the microelectronics technologies have become a major trend. The digital control scheme has the advantages of simple circuitry, software control and flexibility in various applications. In order to verify the validity of the developed control strategies with or without linear Hall sensor, a DSP-based control system is setup for the experiments. In this chapter, the laboratory setup is first introduced. Then, the practical realization issues and analyses of experimental results are presented in detail.

5.1 LABORATORY SETUP

Fig. 5.1 shows the architecture for the implementation of the prototype control system, which consists of a four-pole single-phase BLDC fan motor, a full-bridge inverter with 12V DC-link voltage, signal conditioning circuits, a fixed-point DSP (Texas Instrument, TMS320LF2407A), and a personal computer [39]-[41]. The parameters of the single-phase BLDC fan motor are listed in Table 5.1. The DSP controller performs the real-time control algorithms, including the sensorless algorithm, start-up control and closed-loop current-mode control. The rotor speed is estimated by linear Hall sensor signal or zero-crossing signal. The Hall sensor signal is obtained by differential amplifier with filter component, and the phase current is measured by a current sensing resistor. All variables in the DSP controller can be tuned and monitored by the personal computer via the external RS-232 interface. The experimental setup of the control system is shown in Fig. 5.2.

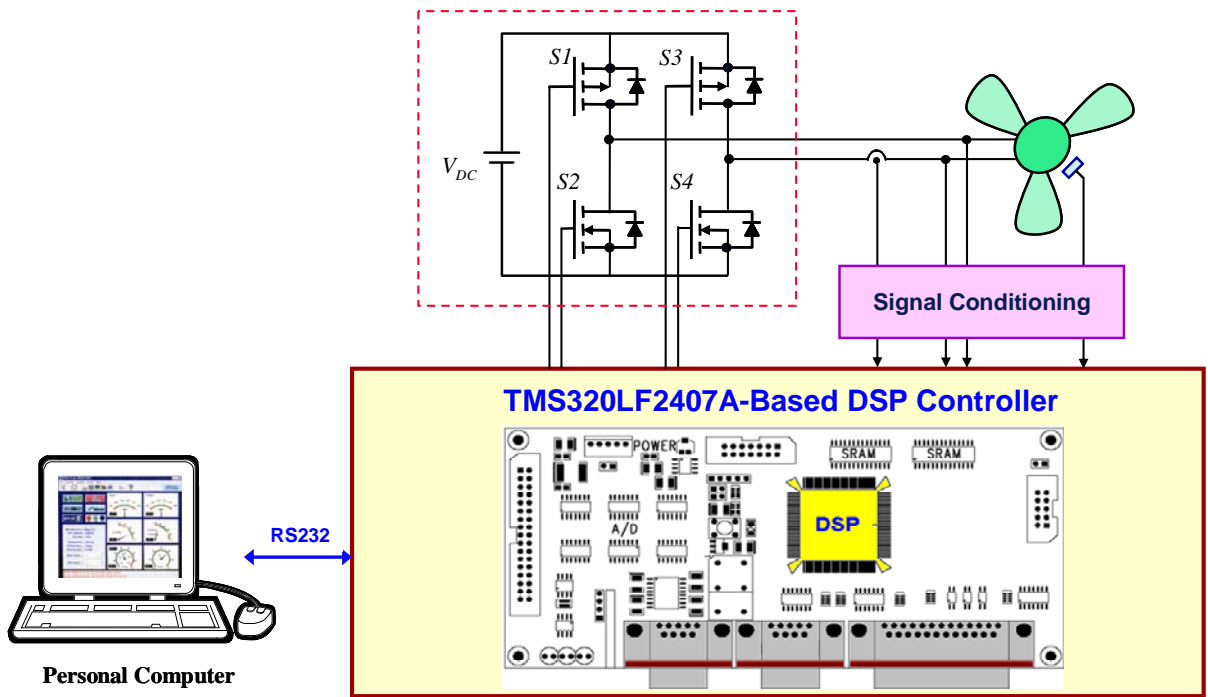


Fig. 5.1. Schematic of the prototype control system for single-phase BLDC fan motor.

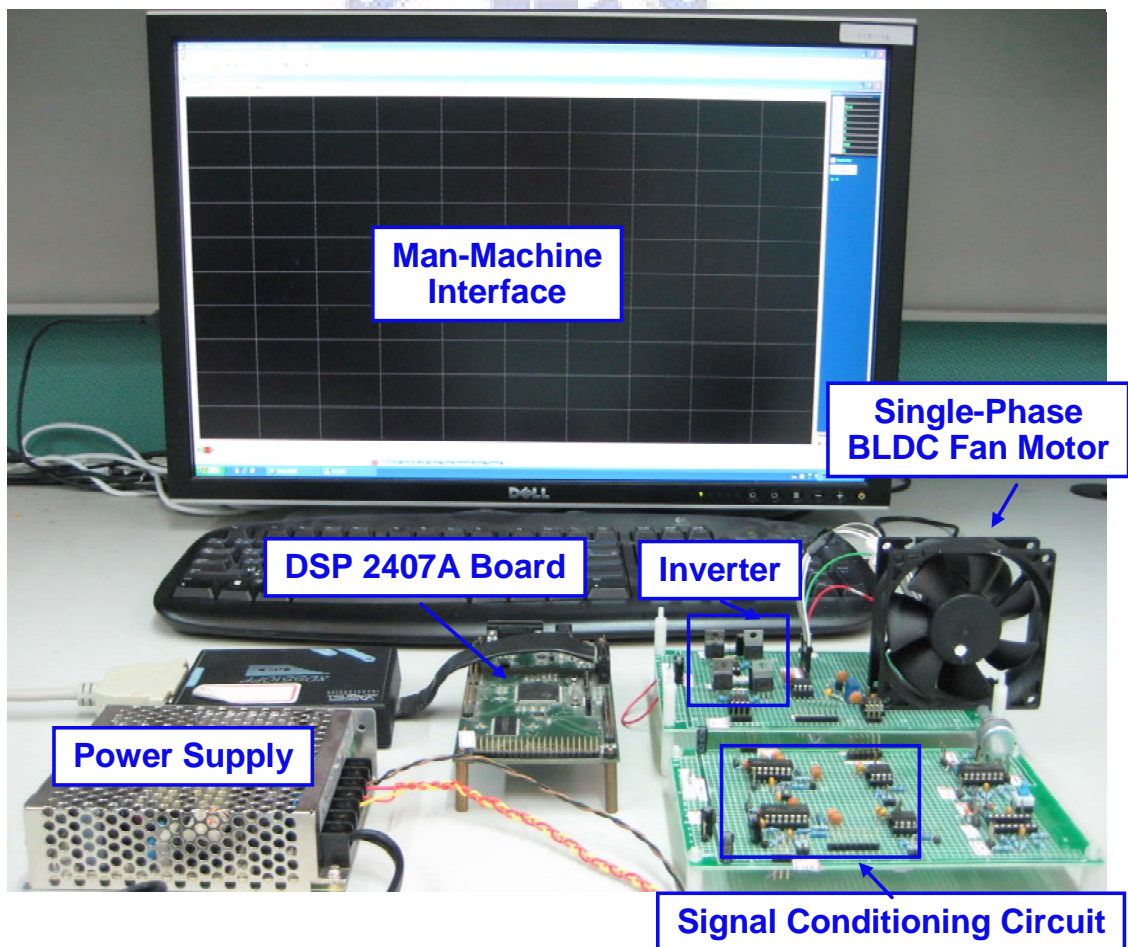


Fig. 5.2. Experimental setup for single-phase BLDC fan motor control system.

TABLE 5.1
Specifications of the Tested Motor

Single-phase brushless dc fan motor	
Type	4 poles
Rated voltage	12 V
Rated power	6.6 W
Rated speed	4200 RPM
Hall sensor	Linear

5.2 SOFTWARE IMPLEMENTATION

For the real-time control algorithms, three periodic interrupts for control and one aperiodic interrupt for communication are set in the DSP as shown in Fig. 5.3. Two fast periodic interrupts with 20 kHz performs the A/D converter synchronization, PWM generation, sensorless algorithm, start-up control and current-loop control. The flow chart of the interrupt service routine (ISR) is shown in Fig. 5.4. It should be noted that both the control algorithm with or without Hall sensor, introduced in chapter 3 and 4, are realized in this ISR. The synchronous sampling technique is adopted to sense the phase current. Another periodic interrupt with 200 Hz performs the rotor speed estimation and rotor locked protection. Fig. 5.5 shows the overall functional block diagram of single-phase BLDC fan motor drive in this research.

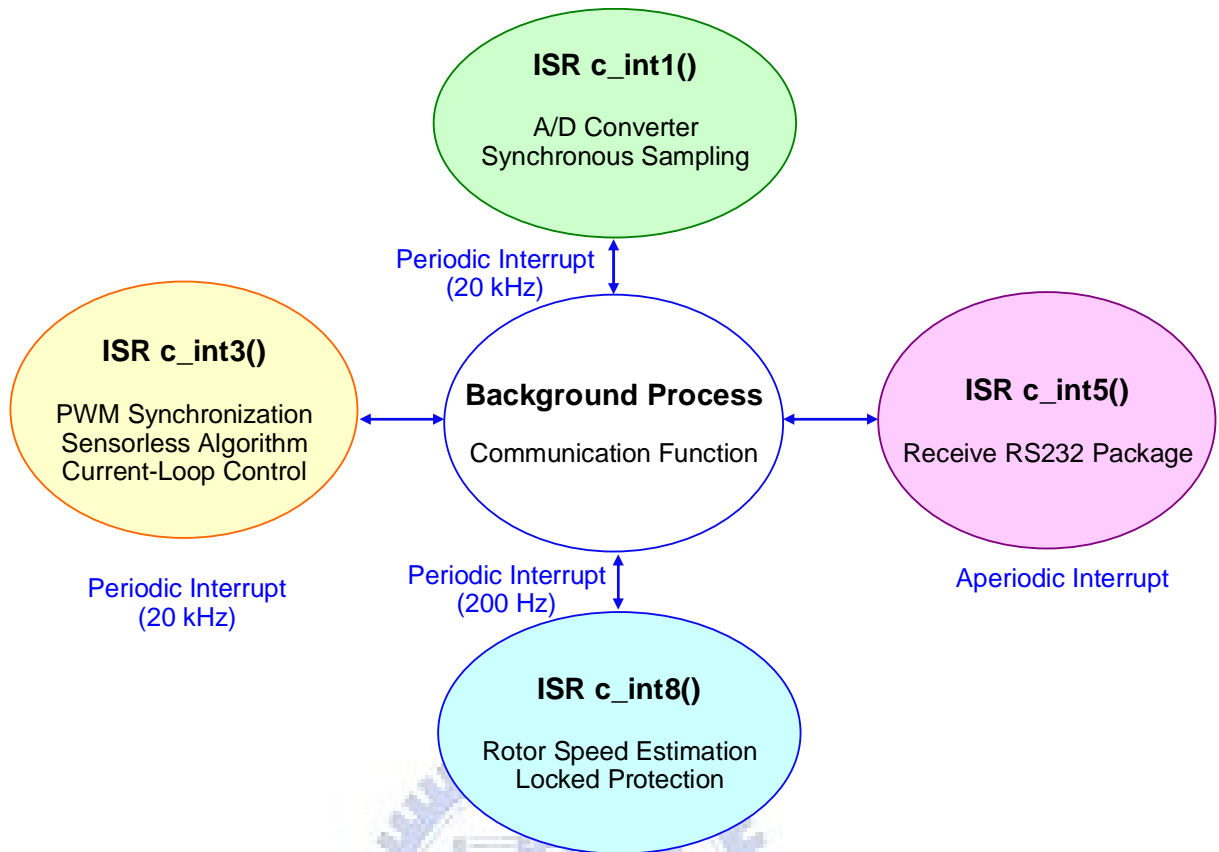
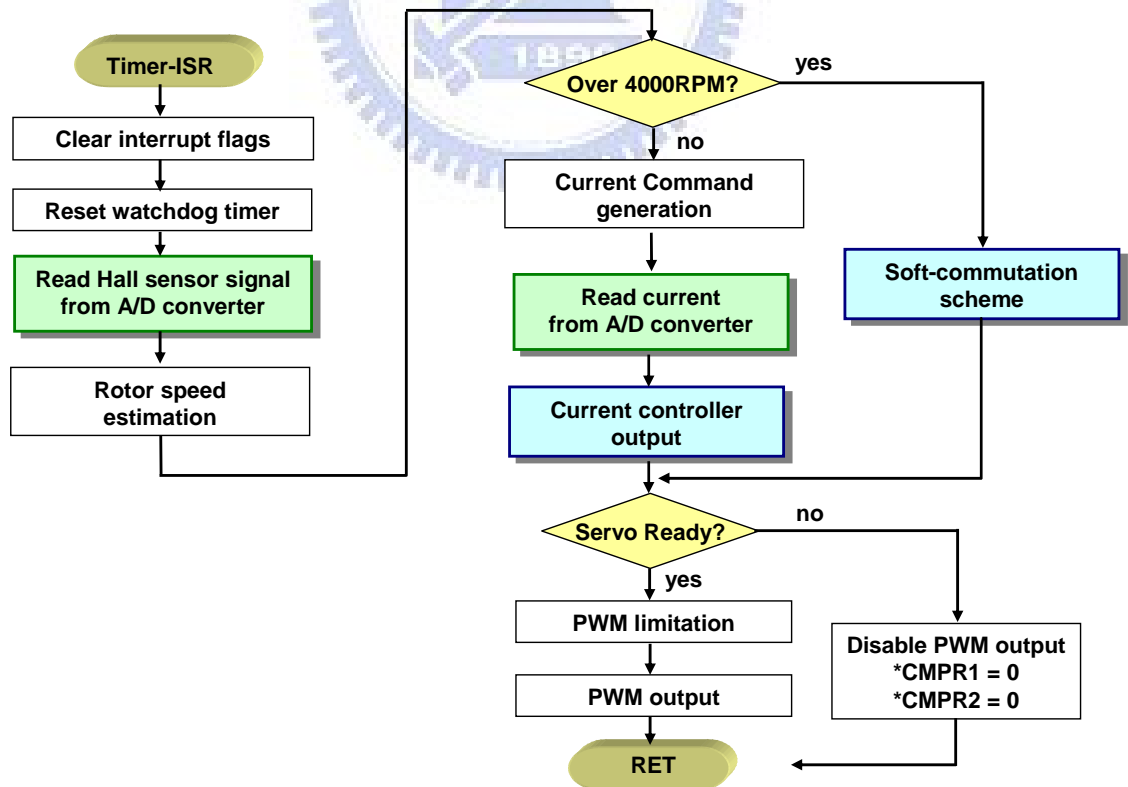
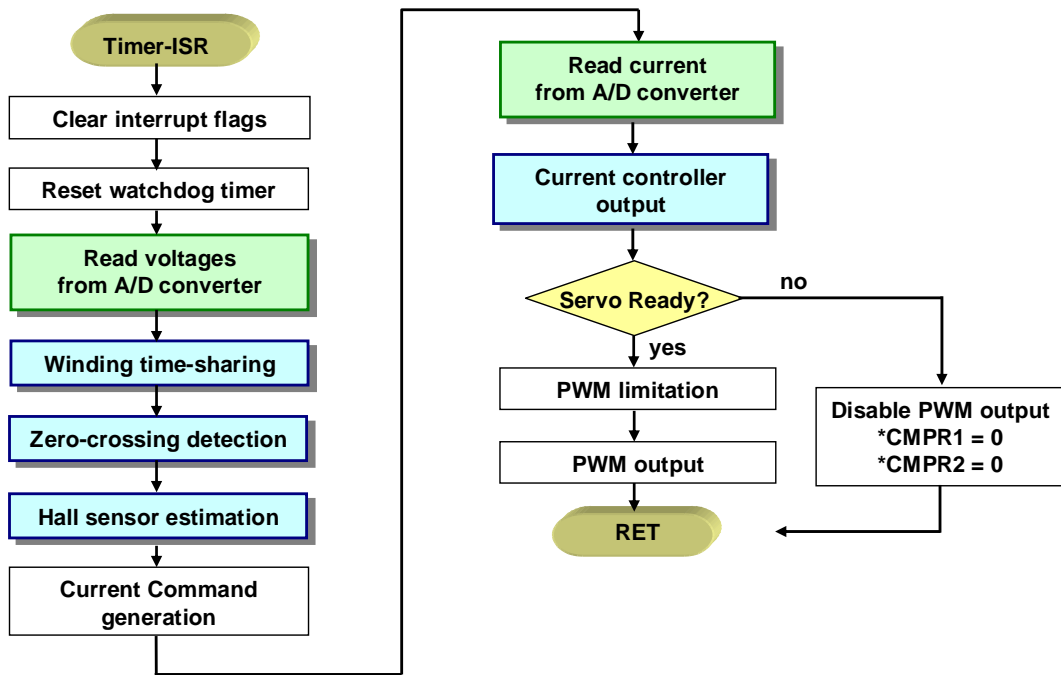


Fig. 5.3. Interrupt configuration in the DSP controller.



(a)



(b)

Fig. 5.4. Program flow chart for control algorithms (a) drive with Hall sensor (b) drive without Hall sensor.

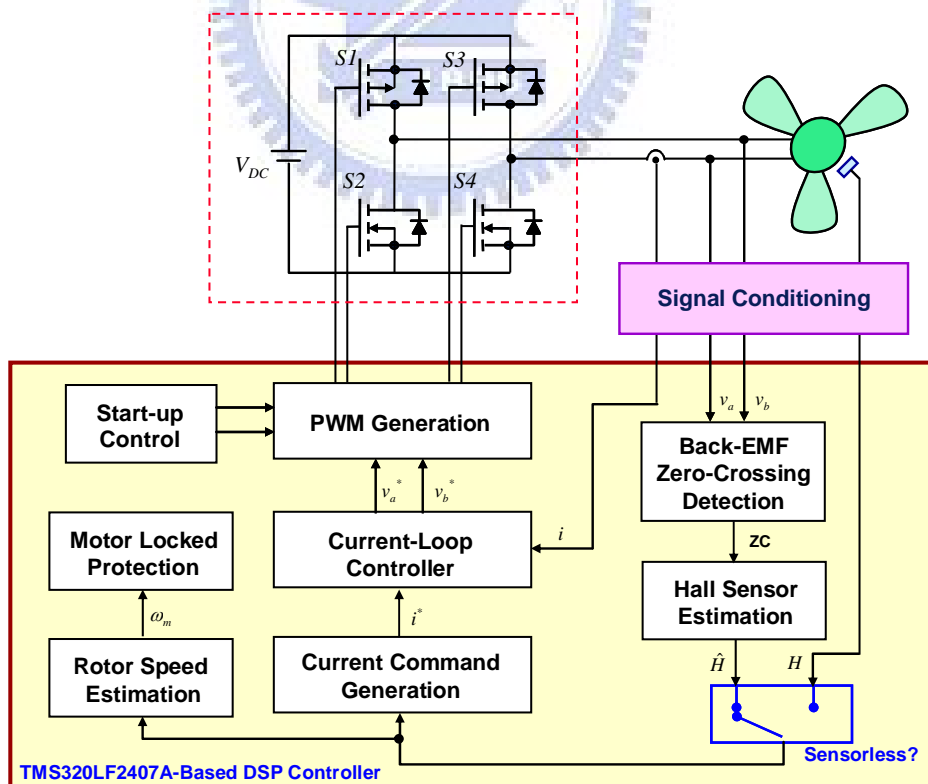


Fig. 5.5. Overall functional block diagram of the single-phase BLDC fan motor control system.

5.3 ANALYSES OF EXPERIMENTAL RESULTS

In this section, experiments on the developed control strategies with or without Hall sensor are carried out. Using the single-phase BLDC fan motor drive setup described in the previous section, the system performance are evaluated for various steady-state and transient operating conditions.

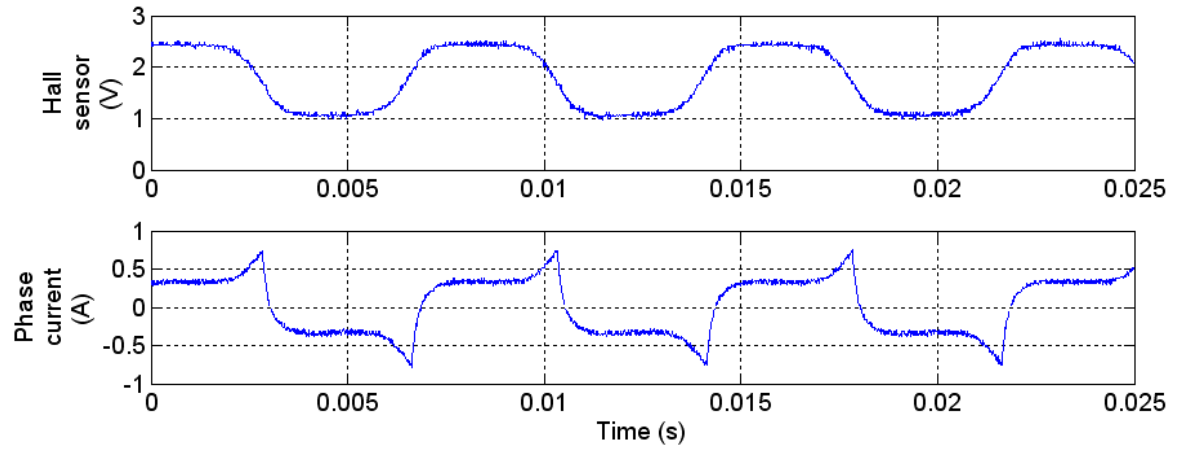
5.3.1 Commutation Control with Hall Sensor

Fig. 5.6 shows the steady-state response when using the open-loop voltage-mode control of hard-commutation scheme at 4000 RPM, 3000 RPM and 1000 RPM, respectively. There are significant current spikes at commutation boundary. To solve this problem, the modification of switching pattern for full-bridge inverter is used. Fig. 5.7 shows the steady-state response when using the open-loop voltage-mode control of soft-commutation scheme at 4000 RPM, 3000 RPM and 1000 RPM, respectively. In Fig. 5.7(a), the phase voltage waveform exists a blanking time of 15 % commutation cycle. Besides, from phase current waveform, there are a 40 % reduction of peak value and a 10 % reduction of RMS value. However, In Fig. 5.7(c), the blanking time is shorten to 5 % commutation cycle, and the improvements of peak current is only 5 % and RMS current is only 2 %. As expected, the soft-commutation control is only suitable for high speed operation.

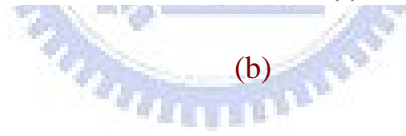
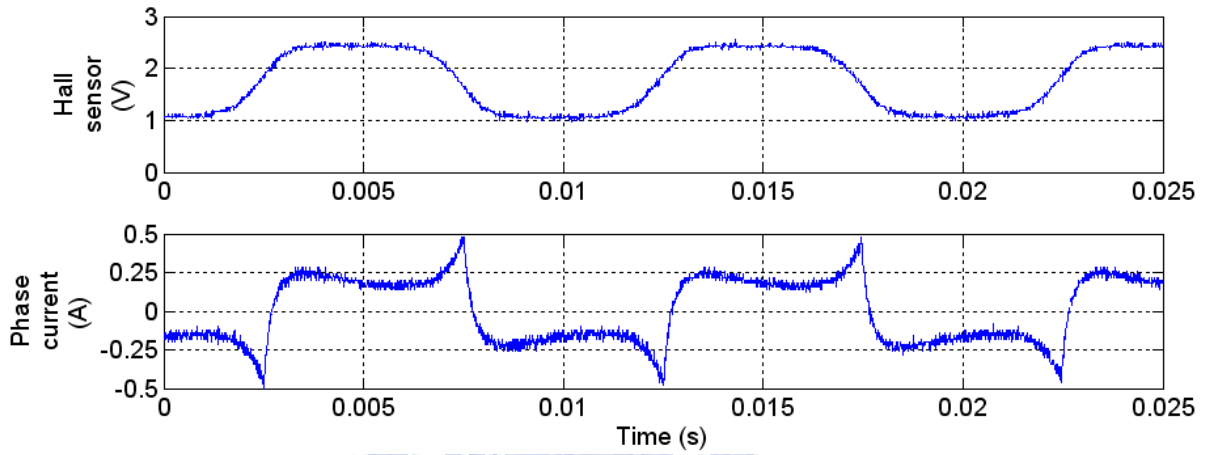
From Chapter 3, the efficiency optimization control scheme is the combination of closed-loop current-mode control for low and middle speed operation and open-loop voltage-mode control of soft-commutation scheme for high speed operation. Fig. 5.8 shows the step response of current-loop control system at zero current by 400 mA step input and 240 mA step input. Both can be seen that the simulation result is close to experiment result. Fig. 5.9, Fig. 5.10 and Fig. 5.11 show the steady-state response at 3000 RPM, 1000 RPM and 500 RPM. For these speed regions, their working mode belongs to current-loop control mode. It

can be seen that the current spike has been removed and the current response is closely followed with current command. Once the fan motor is operated over 4000 RPM, the working mode will switch from current-loop control to soft-commutation control to reduce the current spike, as shown in Fig. 5.12.

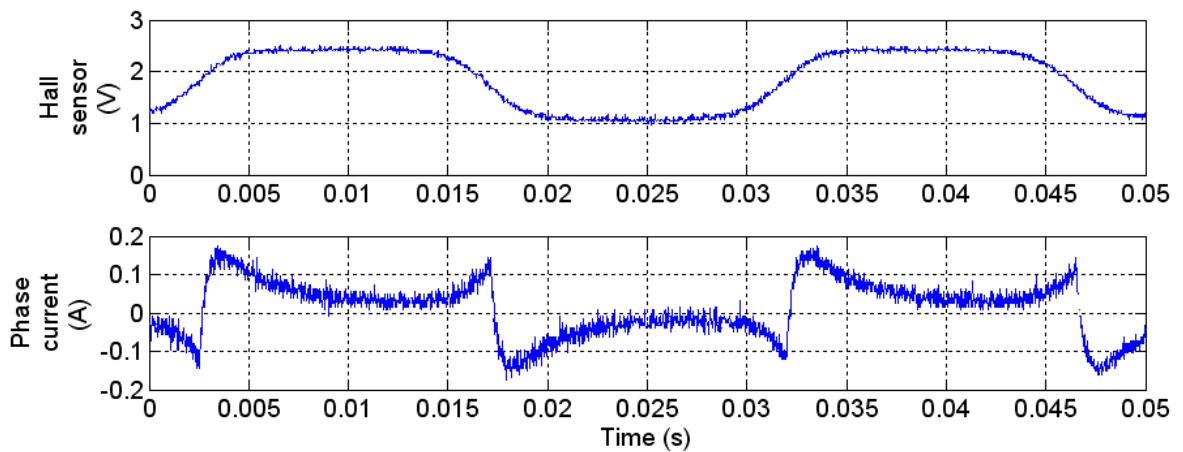
In order to verify the proposed control strategy, the overall efficiency is compared by various control schemes. Fig. 5.13(a) shows the average value of dc-link current versus rotor speed. For entire speed range, the curve of hard-commutation control scheme has higher value than other control methods, which means that it needs more input power to drive the fan motor at the same speed. On the contrary, the curve of developed efficiency optimization control scheme has lower value than other methods. That is to say, the combination of current-loop control and soft-commutation control scheme has maximum efficiency. Fig. 5.13(b) shows the RMS value of phase current versus rotor speed. Similarly, the developed control scheme has relatively lower value for four methods, which means that it has higher utility ratio of current and so as to electrical output power for fan motor. Fig. 5.13(c) shows the peak value of phase current versus rotor speed. Obviously, the peak value has significant reduction for entire speed range, and this will reduce the acoustic noise and power circuit rating. Fig. 5.14 shows the percentage improvement for comparing between worst efficiency case and best efficiency case. It can be seen that there are at least 15 % reduction for average value of dc-link current, at least 17 % reduction for RMS value of phase current and at least 40 % reduction for peak value of phase current. Fig. 5.15 shows the comparison between commercial IC and proposed control scheme, and there is also significantly improvement on RSM value and peak value of phase current.



(a)

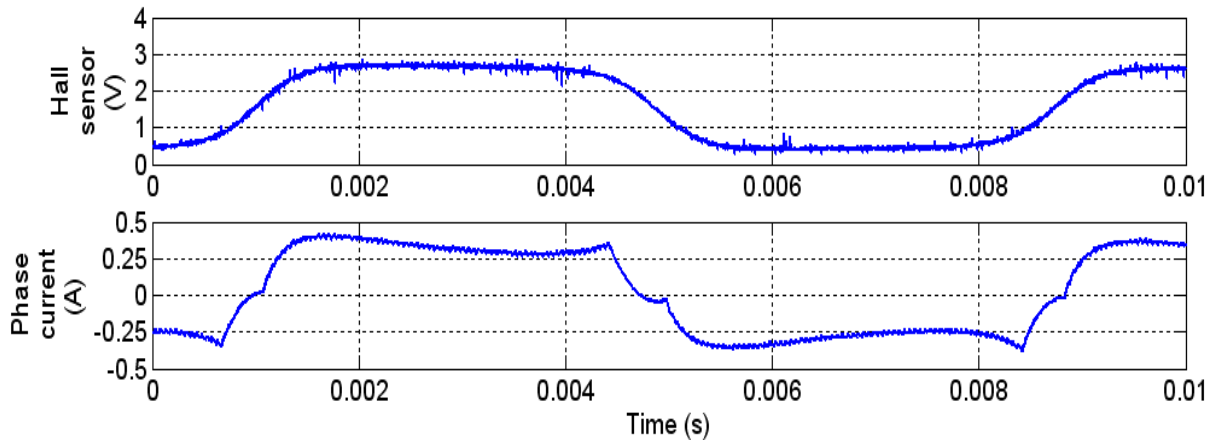


(b)

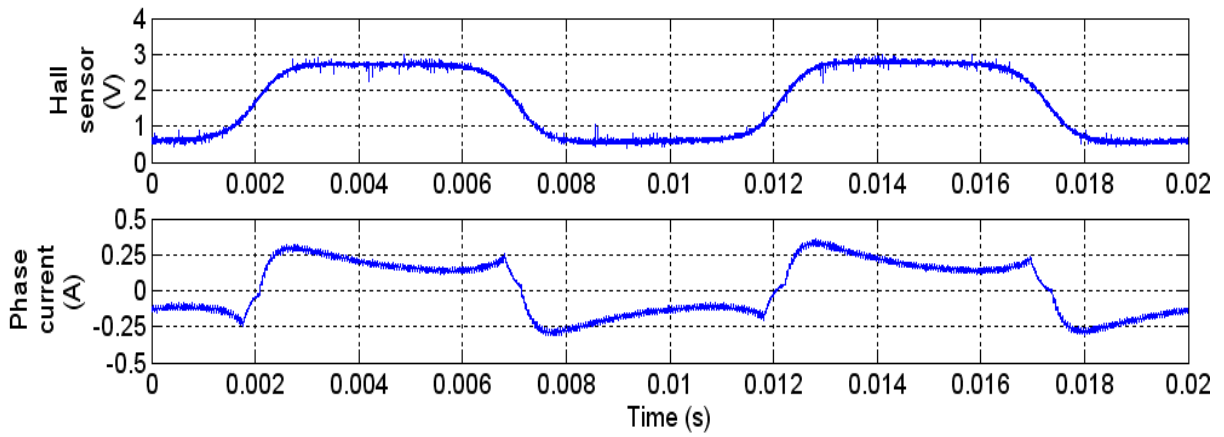


(c)

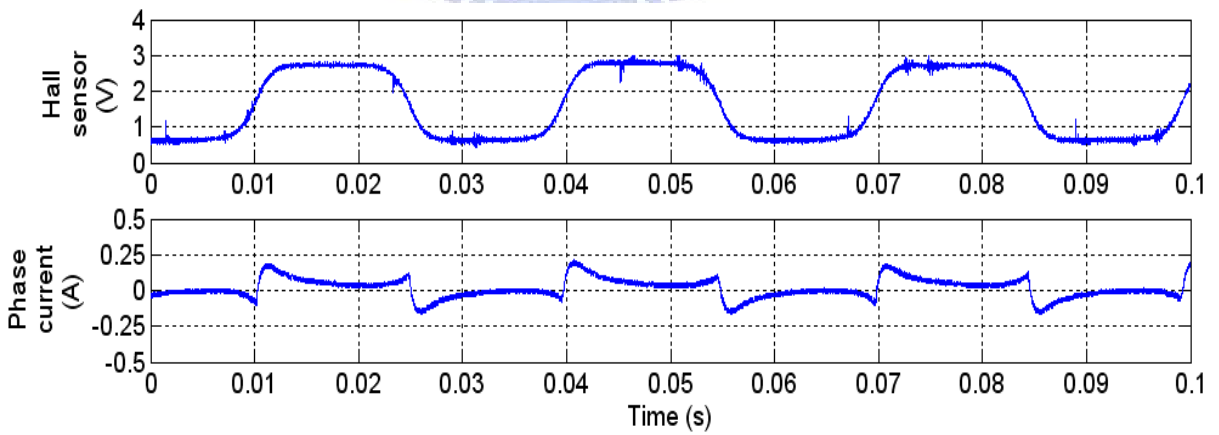
Fig. 5.6. Steady-state response when using the open-loop voltage-mode control of hard-commutation scheme (a) 4000 RPM, (b) 3000 RPM, and (c) 1000 RPM.



(a)

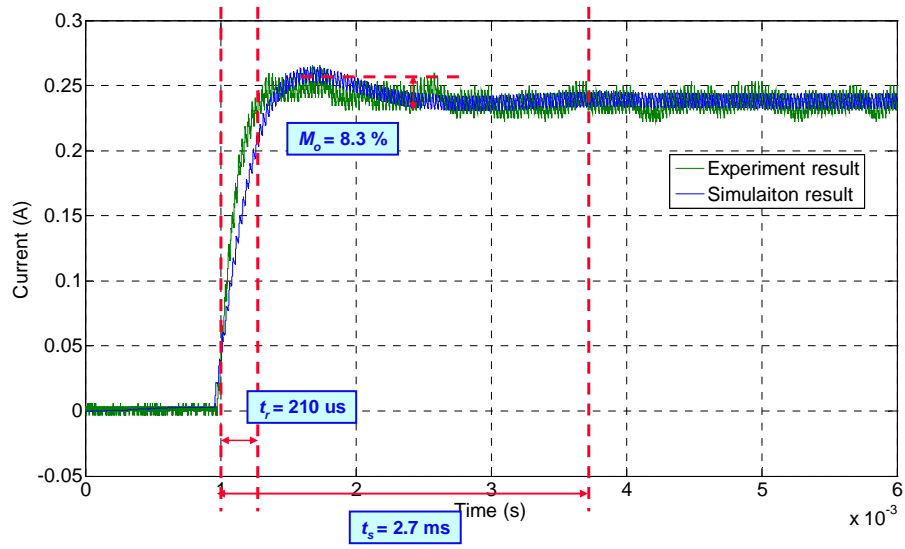


(b)

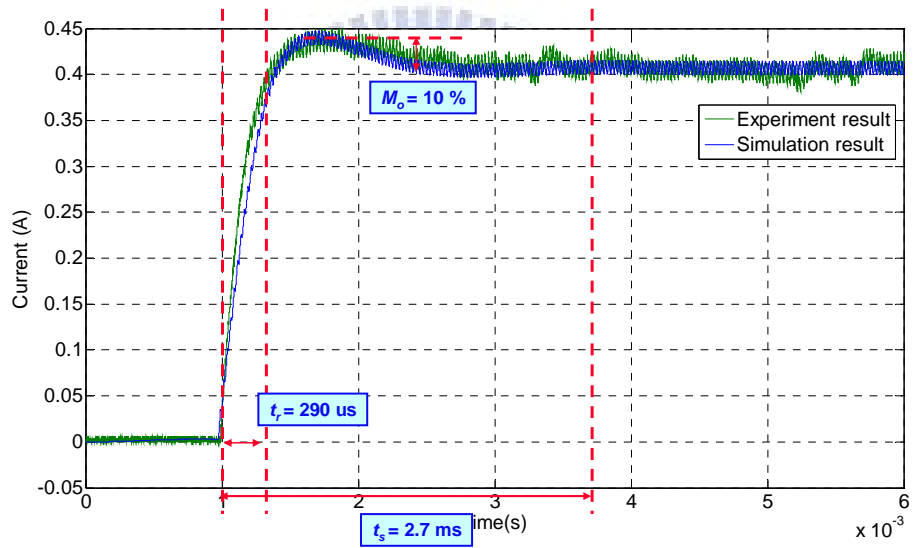


(c)

Fig. 5.7. Steady-state response when using the soft-commutation control scheme (a) 4000 RPM, (b) 3000RPM, and (c) 1000 RPM.

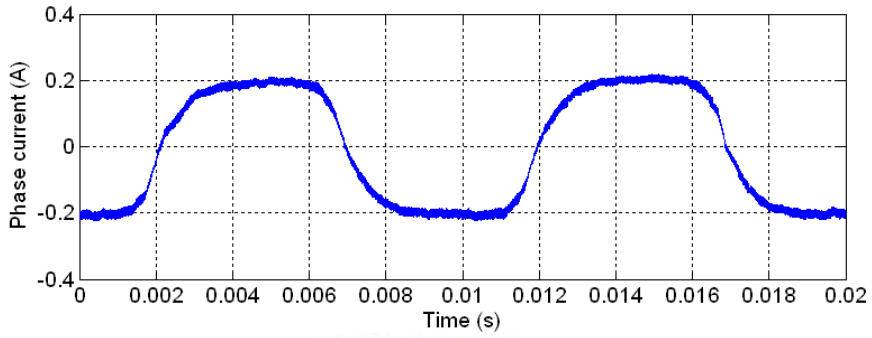
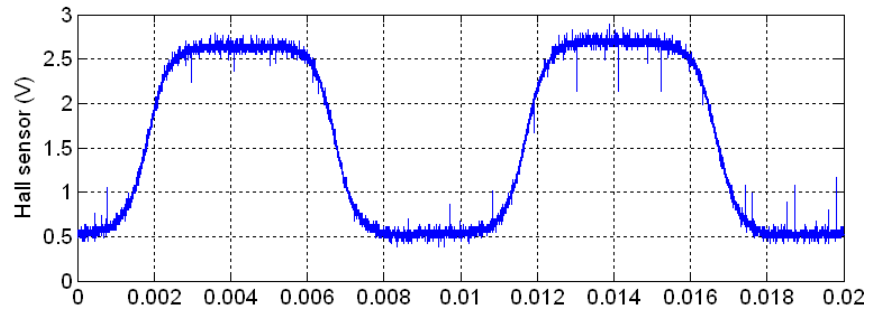


(a)

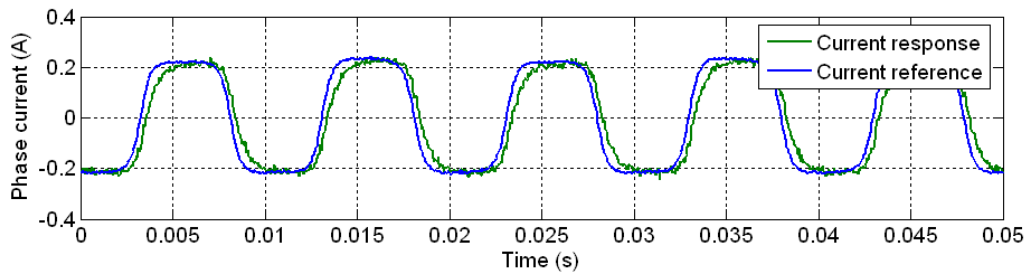
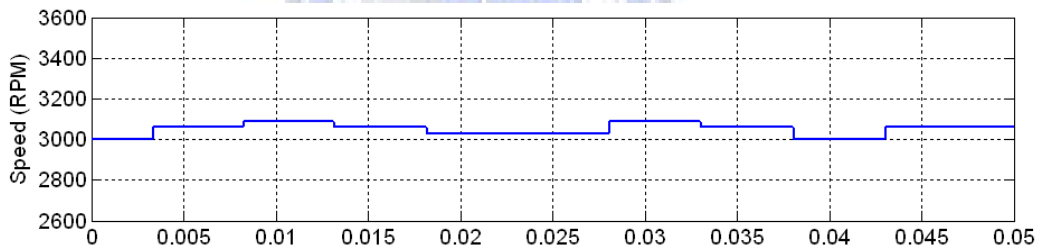


(b)

Fig. 5.8. Step response at zero current (a) 400 mA step input and (b) 240 mA step input.

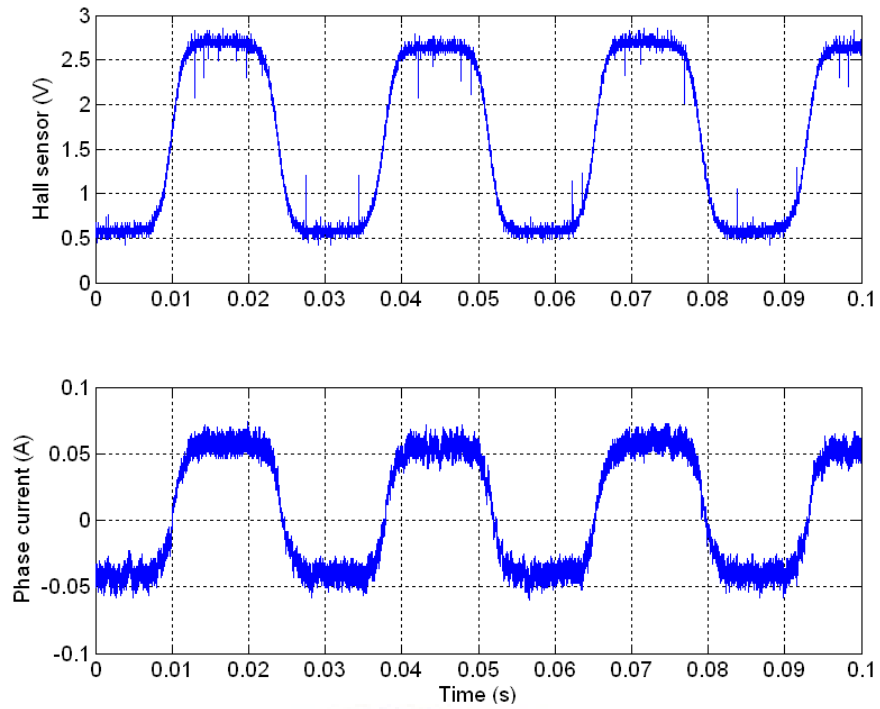


(a)

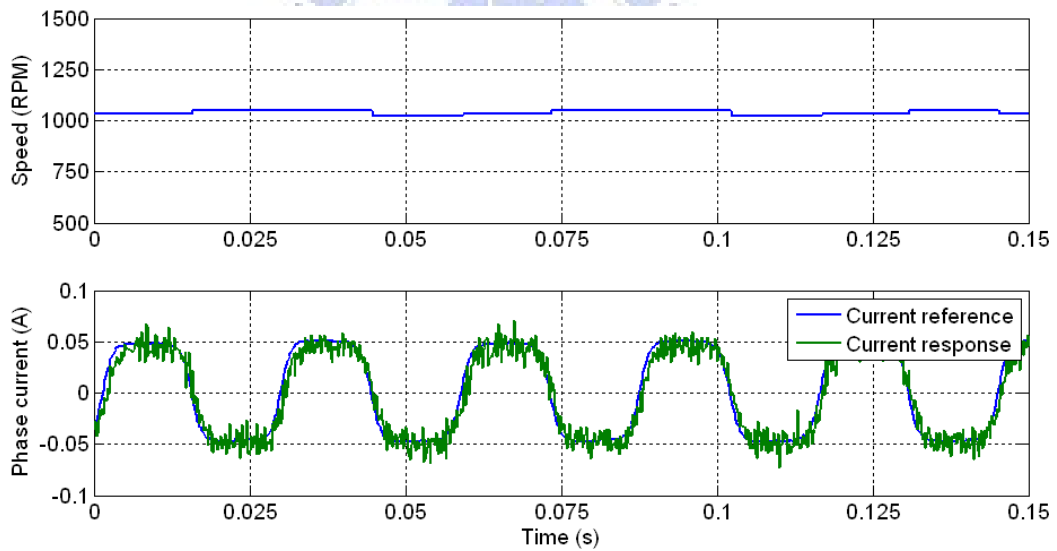


(b)

Fig. 5.9. Steady-state response of closed-loop current-mode control scheme at 3000 RPM (a) Hall sensor and phase current and (b) current reference and response.



(a)



(b)

Fig. 5.10. Steady-state response of closed-loop current-mode control scheme at 1000 RPM (a) Hall sensor and phase current and (b) current reference and response.

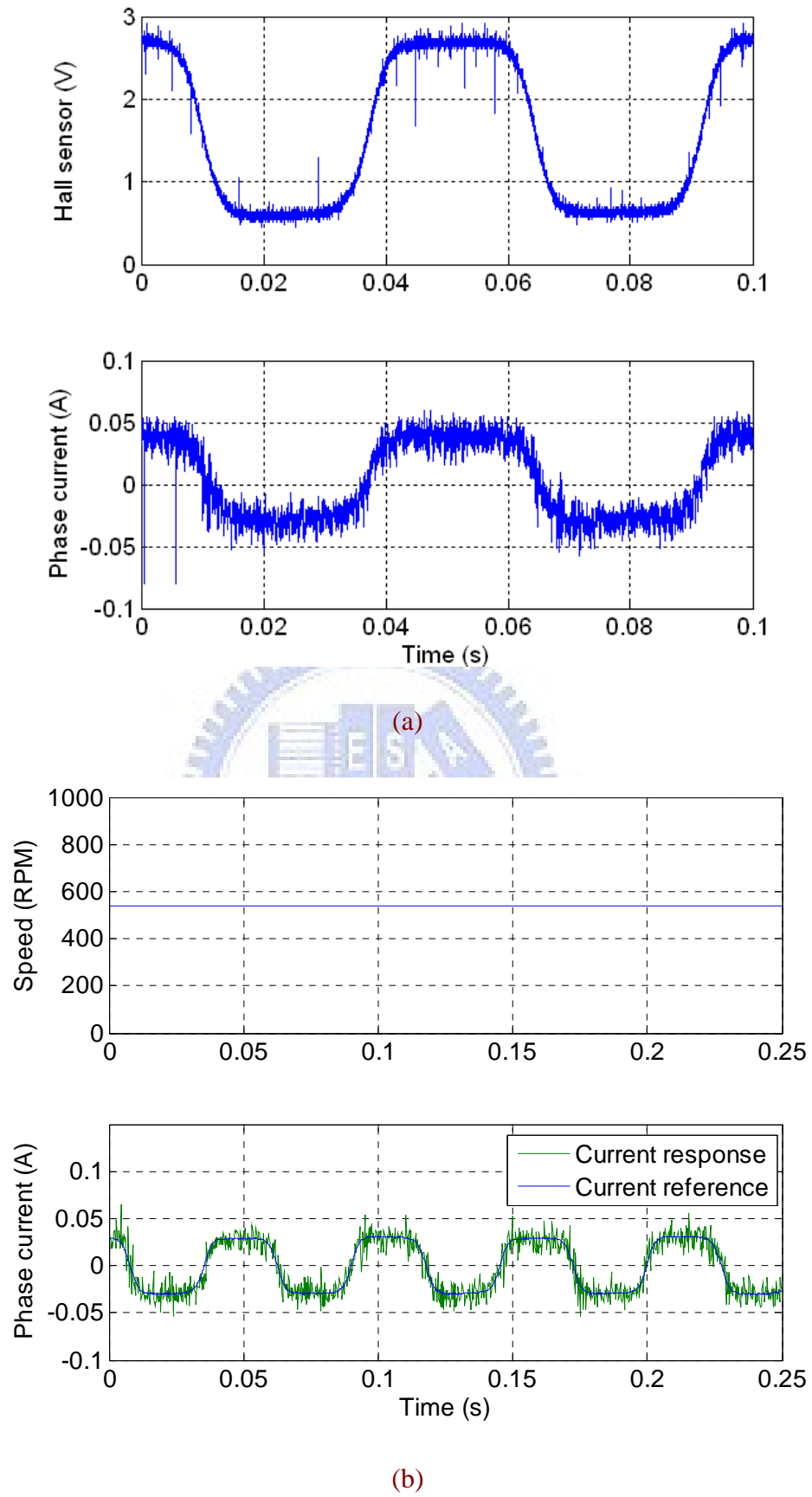


Fig. 5.11. Steady-state response of closed-loop current-mode control scheme at 500 RPM (a)

Hall sensor and phase current and (b) current reference and response.

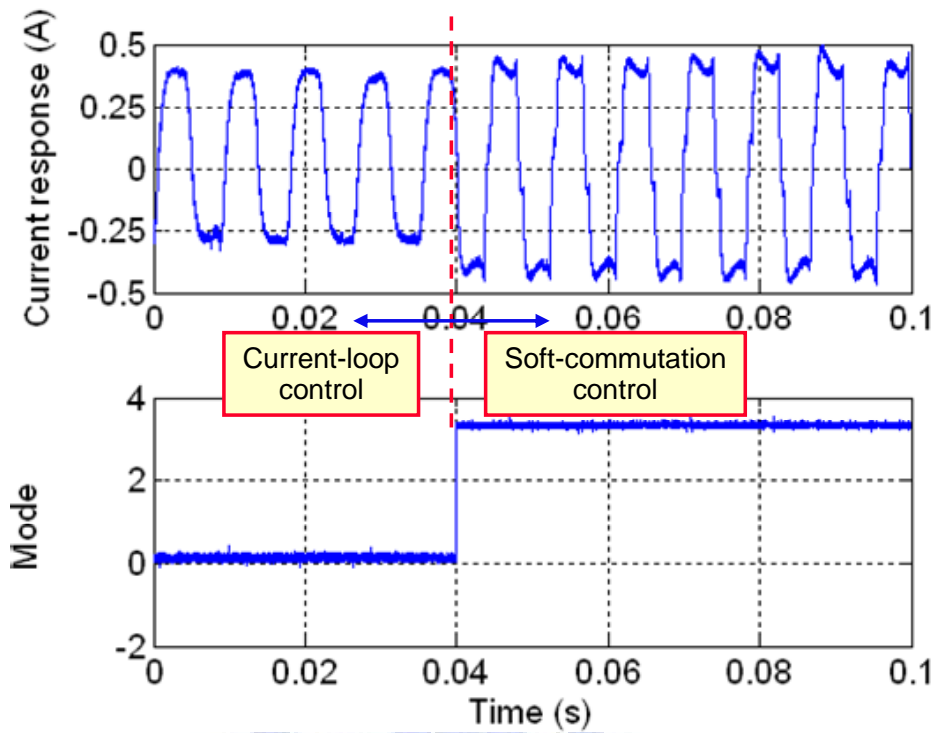
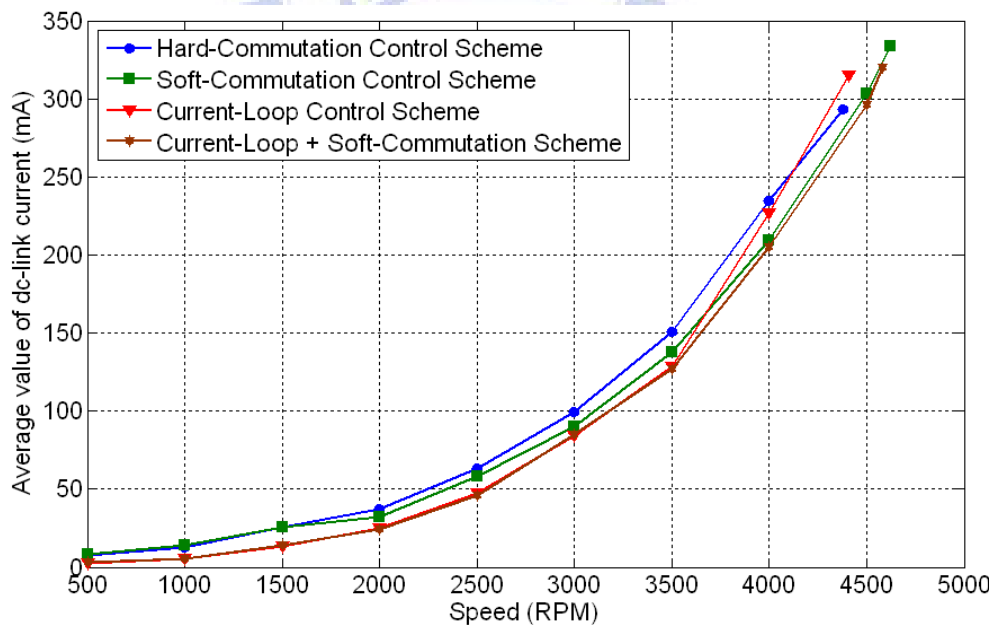
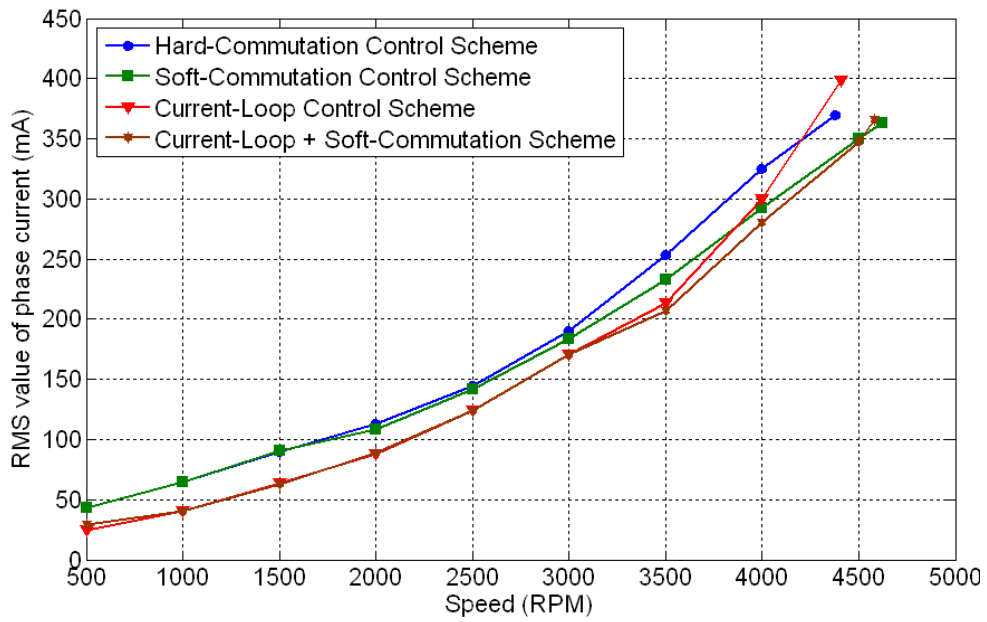


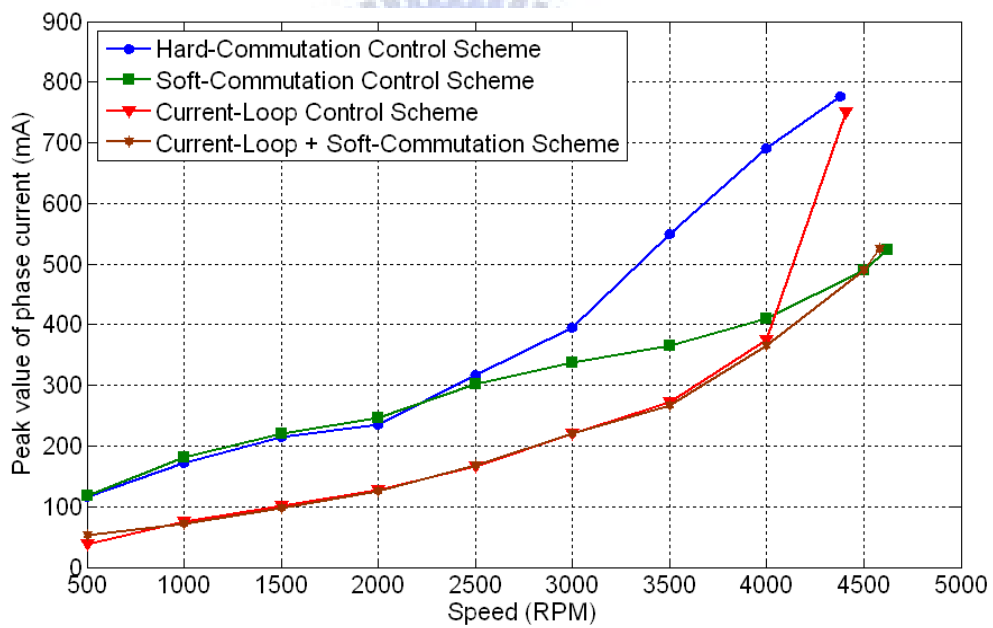
Fig. 5.12. When the fan motor over 4000 RPM, the working mode switches from current-loop control to soft-commutation control



(a)

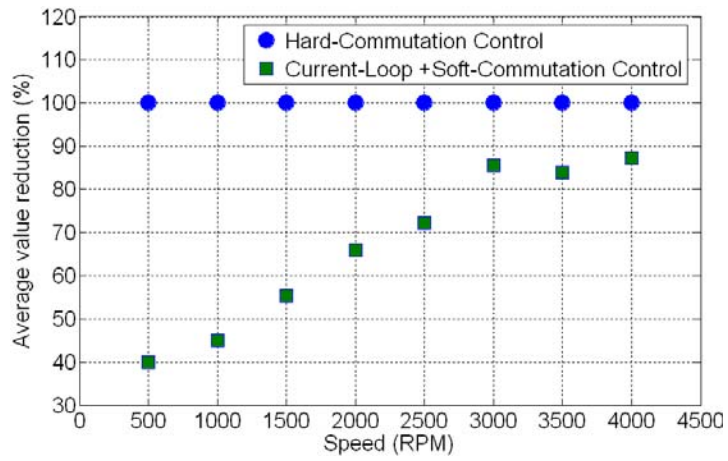


(b)

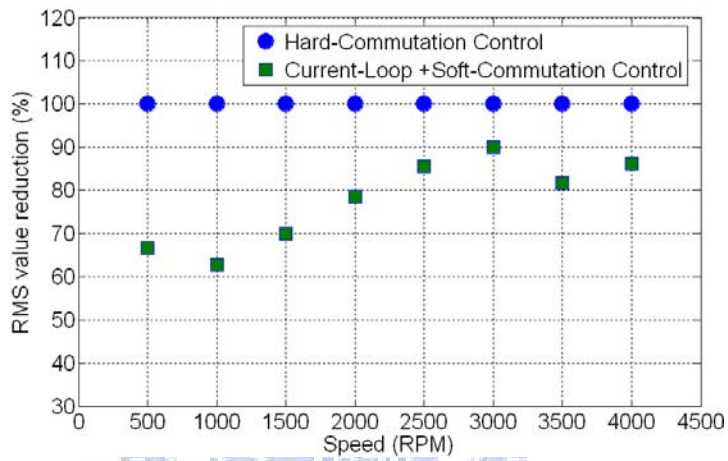


(c)

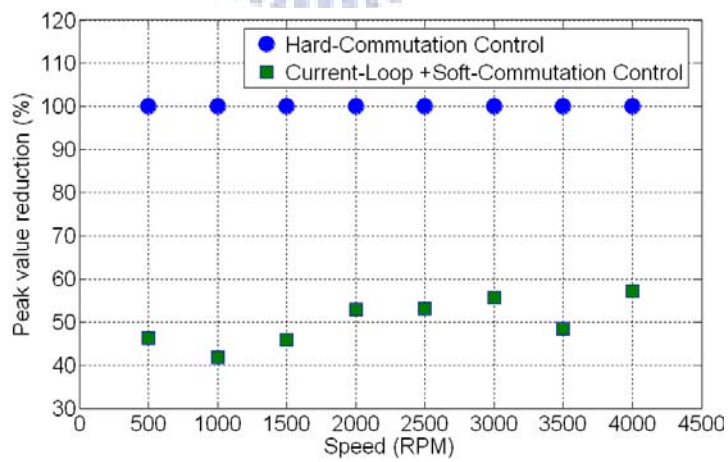
Fig. 5.13. Statistics curves of various control schemes (a) average value of dc-link current versus rotor speed, (b) RMS value of phase current versus rotor speed, and (c) peak value of phase current versus rotor speed.



(a)

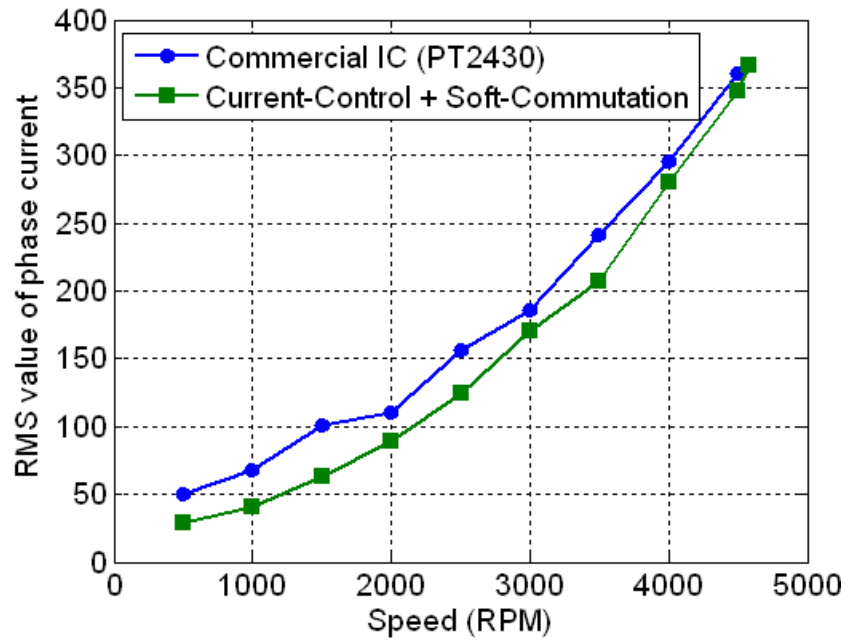


(b)

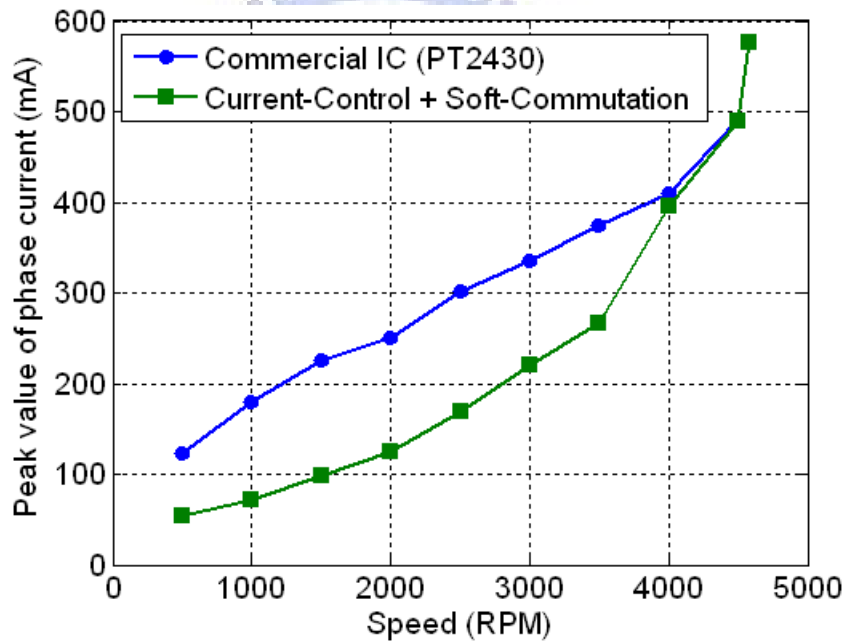


(c)

Fig. 5.14. Percentage improvement for two methods (a) average value of dc-link current (b) RMS value of phase current, and (c) peak value of phase current.



(a)



(b)

Fig. 5.15. Compare commercial IC with proposed control scheme (a) RMS value of phase current and (b) peak value of phase current.

5.3.1 Sensorless Commutation Control

Fig. 5.16 shows the ZCP detection procedure at 3000 RPM. When the driving current decreases to zero, non-excited phase voltage is sampled and compared by control system to produce the sequence of commutation signals. As expected, the timing of ZCP is almost the same to zero of Hall sensor. Fig. 5.17 shows the steady-state response when using the closed-loop current-mode control of sensorless motor drive at 3000 RPM, 2000 RPM, 1000 RPM, and 500 RPM, respectively. By way of look-up table for estimating the Hall sensor signal, the current response has smooth waveform to fit the characteristic of back-EMF. Fig. 5.18 shows the sensorless start-up procedure toward 3000 RPM and 1000 RPM, respectively. The fan motor smoothly starts without Hall sensor and speed up to the required speed. Besides, due to the power circuit rating, the peak current during start-up should be limited. Here, the experiment results show the start-up current is lower than 0.6 A. From Fig. 5.19, the statistics curves of two control methods are very close, that is, the sensorless control keeps the fan motor drive higher efficiency.

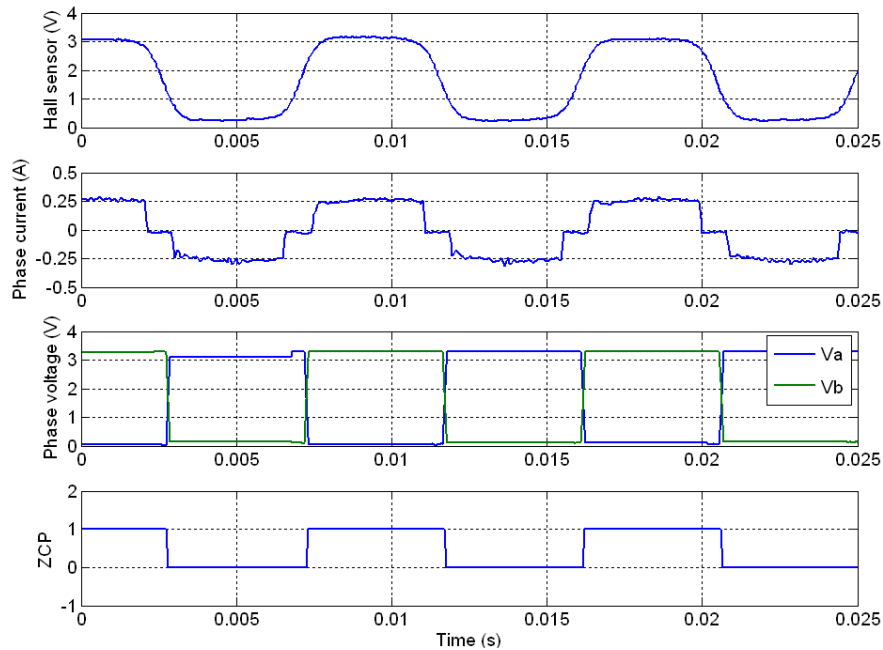
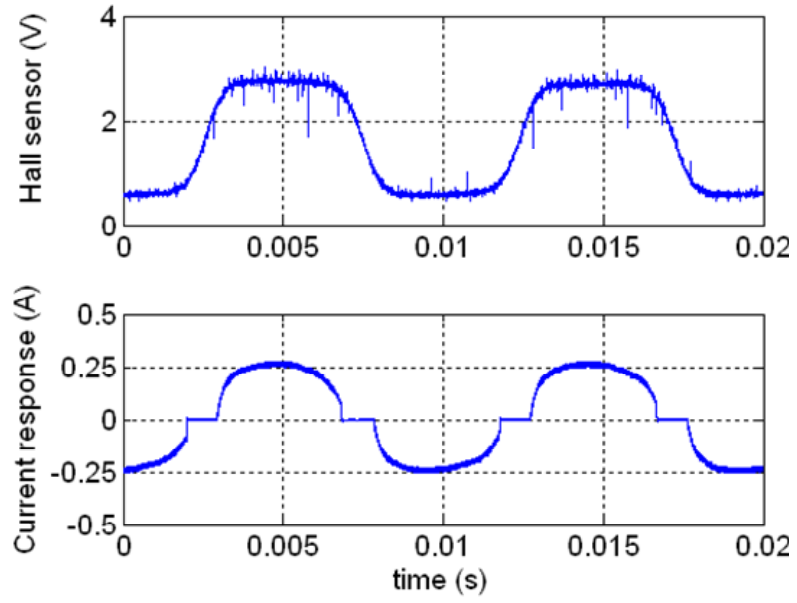
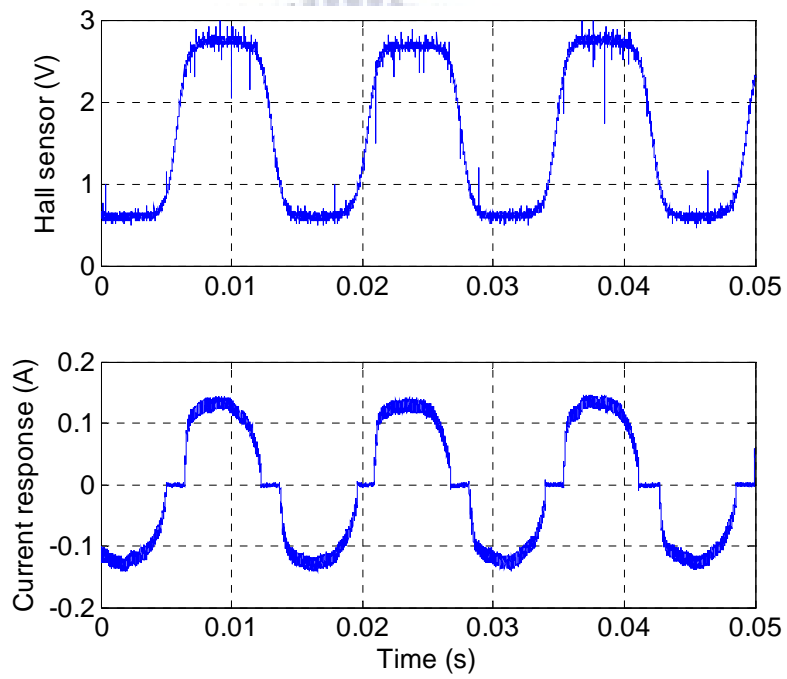


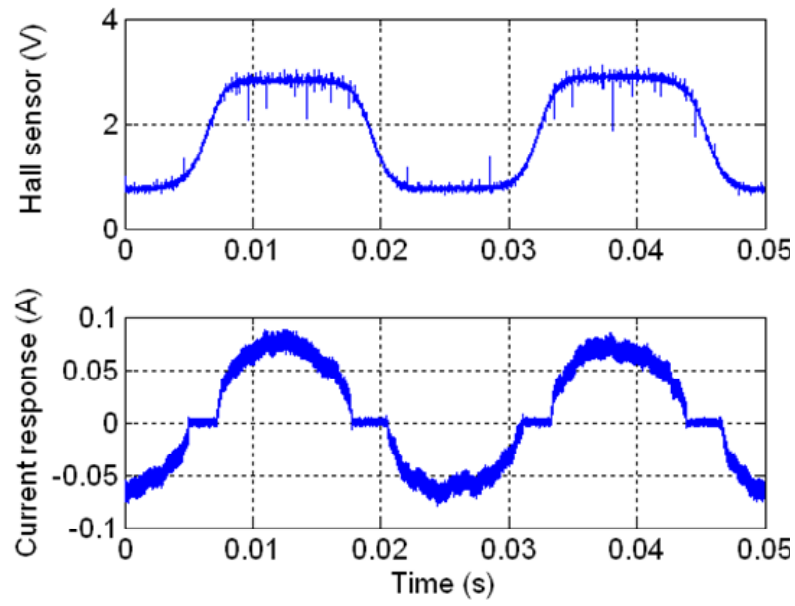
Fig. 5.16. ZCP detection procedure at 3000 RPM.



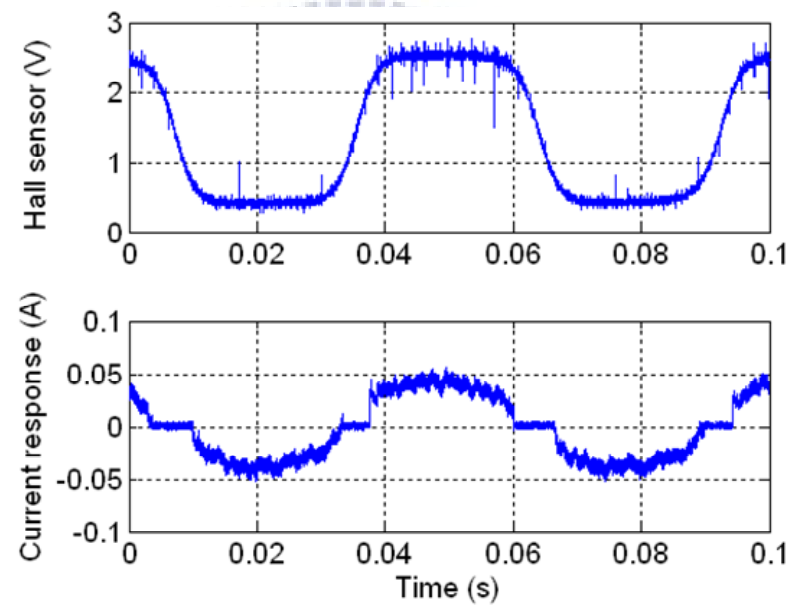
(a)



(b)

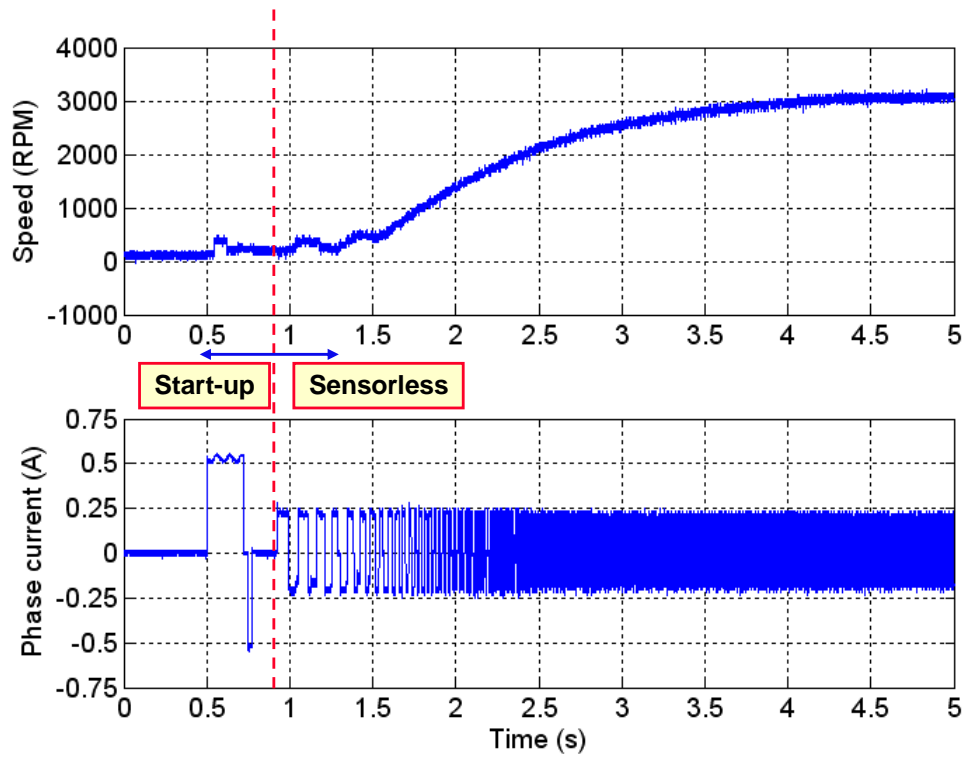


(c)

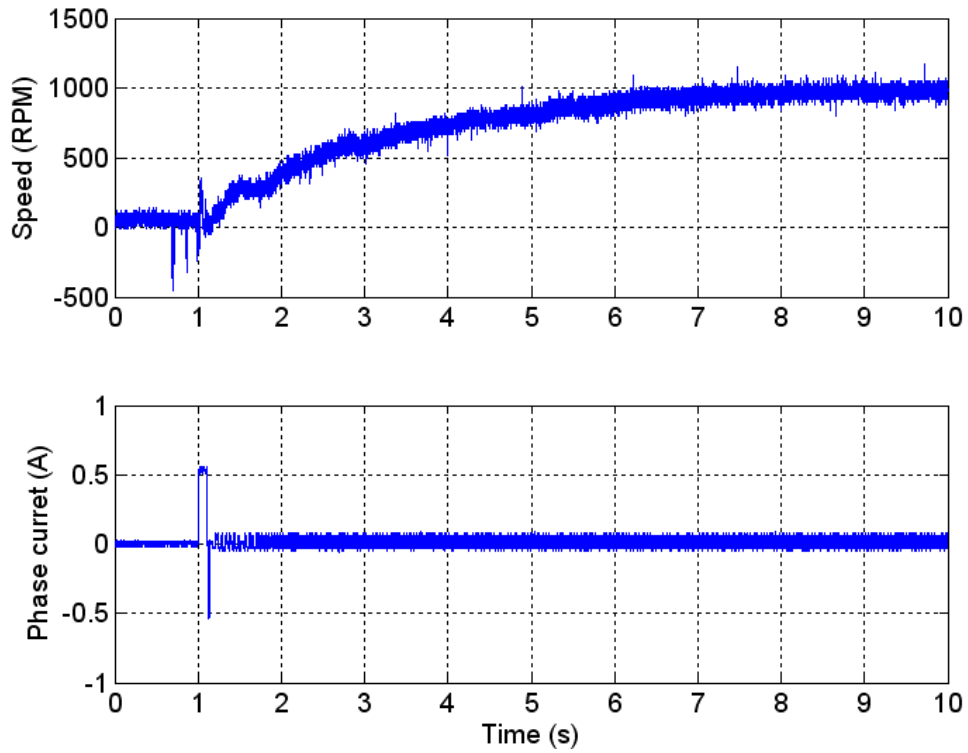


(d)

Fig. 5.17. Steady-state response of closed-loop current-mode sensorless control (a) 3000 RPM, (b) 2000 RPM, (c) 1000 RPM, and (d) 500 RPM.

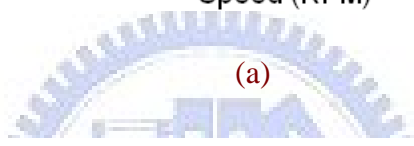
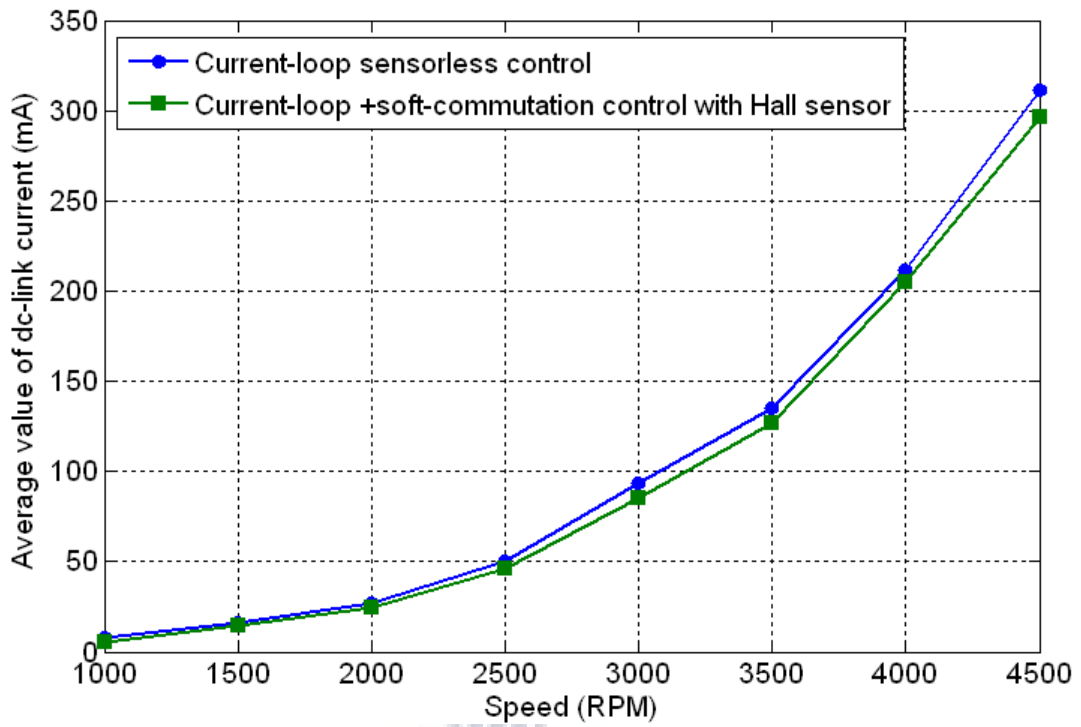


(a)

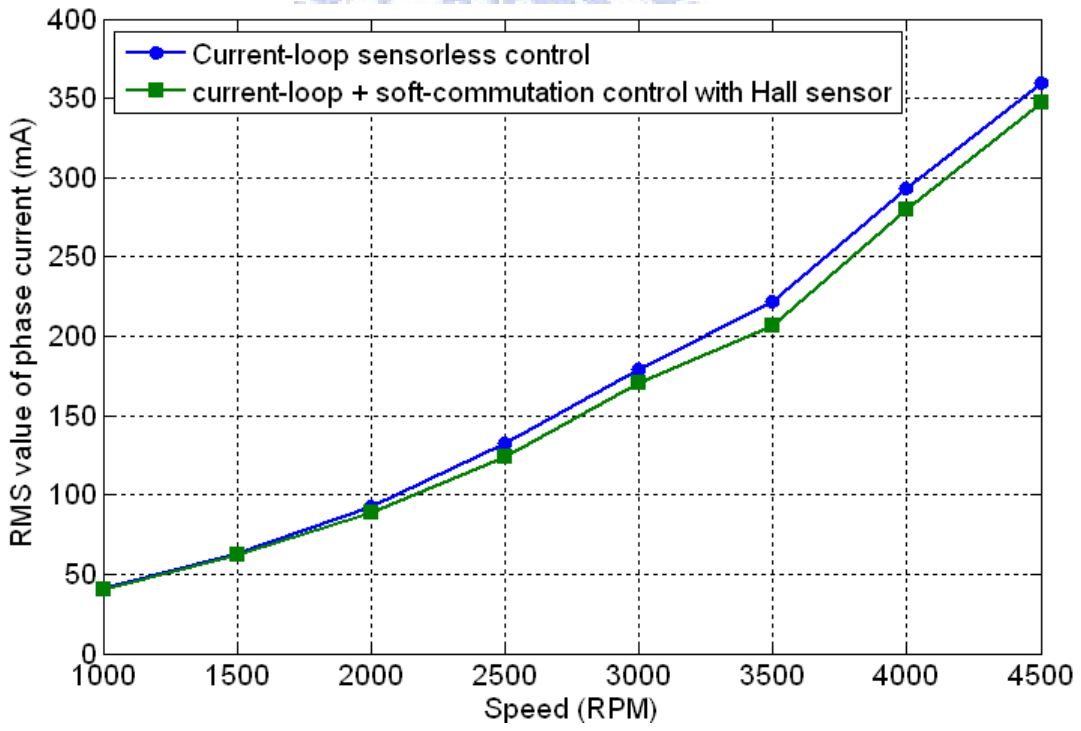


(b)

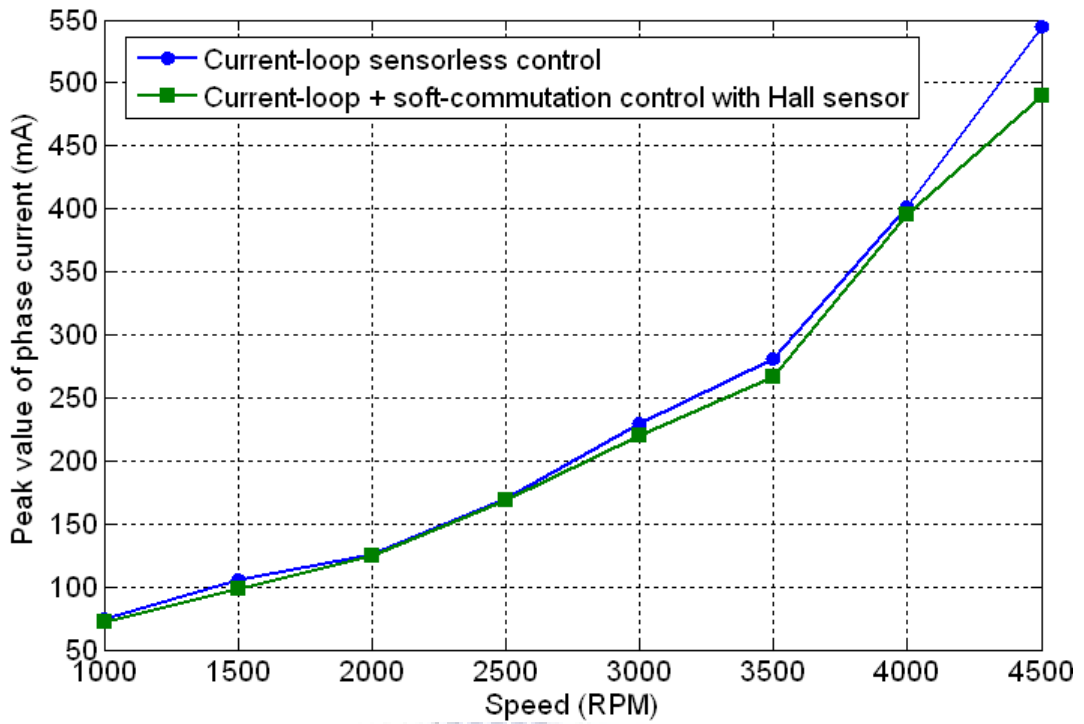
Fig. 5.18. Sensorless start-up procedure (a) toward 3000 RPM and (b) toward 1000 RPM.



(a)



(b)



(c)

Fig. 5.19. Statistics curves of various control schemes (a) average value of dc-link current versus rotor speed, (b) RMS value of phase current versus rotor speed, and (c) peak value of phase current versus rotor speed.

Chapter 6

Conclusions

6.1 CONCLUSIONS

This work presents the efficiency optimization control for single-phase BLDC fan motors with or without Hall sensor. The control scheme has been verified by computer simulation based on the proposed model. Besides, the drive system is implemented by DSP, and some experimental results have been shown to verify the performance and feasibility.

In Chapter 2, in order to prevent an intuitive try-and-error process for designing the control system for single-phase BLDC fan motor, a simple modeling method with illustrated parameter identification has been proposed. The characteristic of nonlinear back-EMF is modeled by a look-up table to confirm the accuracy of proposed model. From simulation results, the phase currents are identical with measurement results under different speed operation. Besides, the simulation results of RMS value of phase current and rotor speed curve under different duty ratio is also close to experiment measurement. Both of all confirms the validity of the proposed model.

Chapter 3 presents an efficiency optimization control scheme for single-phase BLDC fan motors with linear Hall sensor. To produce the maximum output power, the each back-EMF and phase current harmonics should be the same and in phase. This can be achieved by closed-loop current-mode control with linear Hall sensor feedback. Simulation results show that the RMS value of phase current are reduced and current spike is removed at low and middle speed operation, which means that the overall efficiency is significant promoted. For high speed operation, the control system is switched to soft-commutation control mode to

reduce the current spike and widen the high speed control range. The combination of current-loop control and soft commutation control provides the efficiency optimization and wide speed range control scheme for single-phase BLDC fan motors.

Chapter 4 presents a high efficiency and low cost of sensorless control method to drive the single-phase BLDC fan motor without Hall sensor. This method does not need any previous knowledge of the motor parameters, and is robust to motor parameter variations. As compare to the previous approaches, the presented technique has advantages of simplifying the detection procedures and lowering the realization cost. Besides, the specific sensorless starting method based on the feature of asymmetric air gap can smoothly start-up the fan motor and accelerate to high speed operation. In order to improve the overall efficiency, the closed-loop current-mode is also applied to sensorless control system. The linear Hall sensor feedback is replaced by estimated Hall sensor produced from look-up table. Simulation results have verified the proposed sensorless control method which can work properly under different speed operation.

Chapter 5 discusses the implementation of the prototype control system with or without Hall sensor on a digital signal processing hardware platform. The DSP controller performs the real-time control algorithms, including the sensorless algorithm, start-up control and current-loop control, etc. Then, the practical realization issues and analyses of experimental results are also presented.

In summary, this work presents efficiency optimization control for single-phase BLDC fan motors with or without Hall sensor. The developed control strategies are first verified by proposed model, and then fulfill on a real single-phase BLDC fan motor based on DSP controller.

6.2 FUTURE WORKS

In chapter 3, the linear Hall sensor produces an output signal which is proportional to the intensity of the induced rotor field. However, due to the phase lag caused by feedback filter, the phase current and back-EMF can not be perfectly in phase though the Hall signals which is used for command reference. This phenomenon will also exist in the sensorless control system in chapter 4. So, this may be lower the overall efficiency. To solve the problem, an auto phase tuning mechanism can be introduced to decrease the phase differences between phase current and back-EMF, and consequently increase the efficiency.

In recent years, FPGA-based hardware implementation technology has been used to motor control systems due to the advantages of their programmable hard-wired feature, fast time-to-market and reusable IP (Intellectual Property) cores. Besides, the FPGA-based system can get a very high speed level, since it can carry out parallel processing by means of hardware mode. Therefore, a fully digital control IC with or without Hall sensor can provide a simple and feasible solution for single-phase BLDC fan motor drives

Reference

- [1] Tetsuya Yoshitomi and Yasuyuki Ueshima, "Driving a single-phase motor," United States Patent, US 7,148,643 B2.
- [2] K. N. Hsu, "Pulse-width modulation speed controllable dc brushless cool fan," United States Patent, US 5,099,181.
- [3] Z. Q. Zhu, S. Bentouati, and D. Howe, "Control of single-phase permanent magnet brushless DC drives for high-speed applications," *IEEE Power Electronics and Variable Speed Drive Conf.*, pp. 327-332, Sep. 2000.
- [4] Laurence Armstrong, "Current control removes brushless DC motor commutation spikes," Application Note ZE0469, Zetex Semiconductors, Aug. 2005.
- [5] L. Sun, Q. Fang, and J. Shang, "Drive of Single-Phase Brushless DC Motors Based on Torque Analysis," *IEEE Trans. Magnetics*, vol. 43, no. 1, pp. 46-50, Jan. 2007.
- [6] A. Lelkes and M. Bufe, "BLDC motor for fan application with automatically optimized commutation angle," *IEEE Power Electronics Specialists Conf. (PESC)*, vol. 3, pp. 2277-2281, Jun. 2004.
- [7] P. P. Acarnley and J. F. Watson, "Review of position-sensorless operation of brushless permanent-magnet machines," *IEEE Trans. Ind. Electron.*, vol. 53, no. 2, pp. 352-362, Apr., 2006.
- [8] J. Shao, D. Nolan, T. Hopkins, "A novel direct back EMF detection for sensorless brushless DC (BLDC) motor drives," *IEEE Applied Power Electronics Conference and Exposition (APEC)*, vol. 1, pp. 33-37, Mar. 2002.
- [9] J. Shao, D. Nolan, M. Teissier, D. Swanson, "A novel microcontroller-based sensorless brushless DC (BLDC) motor drive for automotive fuel pumps," *IEEE Trans. Ind. Electron.*, vol. 39, pp. 1734-1740, Nov.-Dec. 2003.
- [10] J. Shao, D. Nolan, T. Hopkins, "Improved direct back EMF detection for sensorless brushless DC (BLDC) motor drives," *IEEE Applied Power Electronics Conference and Exposition (APEC)*, vol. 1, pp. 300-305, Feb. 2003.
- [11] M. F. Rahman, L. Z. E. Haque, and M. A. Rahman, "A direct torque-controlled interior permanent-magnet synchronous motor drive without a speed sensor," *IEEE Trans. Energy Conversion*, vol. 18, no. 1, pp. 17-22, Mar. 2003.
- [12] S. Bolognani, L. Tubiana, and M. Zigliotto, "EKF-based sensorless IPM synchronous motor drive for flux-weakening applications," *IEEE Ind. Appl.*, vol. 39, no. 3, pp. 768-775, May-Jun. 2003.
- [13] D. K. Kim, K. W. Lee, B. T. Kim, and B. I. Kwon, "A novel starting method of the SPM-type BLDC motors without position sensor for reciprocating compressor," *IEEE Industry Application Conf. (IAS)*, vol. 2, pp. 861-865, Oct. 2006.
- [14] L. Ying and N. Ertugrul, "A starting strategy for a robust position sensorless technique in non-salient PM AC motor drives," *IEEE Power Electronics and Motion Control Conf. (IPEMC)*, vol. 2, pp. 1028-1032, Aug. 2004.
- [15] Y. S. Lai, F. S. Shyu, and S. S. Tseng, "New initial position detection technique for three-phase brushless DC motor without position and current sensors," *IEEE Trans. Ind. Appl.*, vol. 39, pp.

485-491, Mar.-Apr. 2003.

- [16] J. S. Mayer and O. Wasynczuk, "Analysis and modeling of a single-phase brushless dc motor drive system," *IEEE Trans. Energy Conversion*, vol. 4, pp. 473-479, Sep. 1989.
- [17] D. R. Huang, C. Y. Fan, S. J. Wang, H. P. Pan, T. F. Ying, C. M. Chao, and Eric G. Lean, "A new type single-phase spindle motor for HDD and DVD," *IEEE Trans. Magnetics*, vol. 35, pp. 839-844, Mar. 1999.
- [18] Y. C. Liang and V. J. Gosbell, "Realistic computer model of dc machine for CADA topology on SPICE2," *IEEE Power Electronics Specialists Conf. (PESC)*, vol. 2, pp. 765-771, Apr. 1988.
- [19] C. B. Rajanathan, H. Acikgoz, and R. Egin, "Transient characteristics of the single phase permanent magnet synchronous motor," *IEEE Trans. Magnetics*, vol. 35, no. 5, pp. 3589-3591, Sep. 1999.
- [20] C. L. Chiu, Y. T. Chen, and W. S. Jhang, "Properties of Cogging Torque, Starting Torque, and Electrical Circuits for the Single-Phase Brushless DC Motor," *IEEE Trans. Magnetics*, vol. 44, no. 10, pp. 2317-2323, Oct. 2008.
- [21] D. Y. Ohm and R. J. Oleksuk, "Influence of PWM schemes and commutation methods for DC and brushless motors and drives," P.E. Technology Conference, Oct. 2002.
- [22] R. Shao, Z. Guo, and L. Chang, "A PWM Strategy for Acoustic Noise Reduction for Grid-Connected Single-Phase Inverters," *IEEE Applied Power Electronics Conf. (APEC)*, pp. 301-305, Feb. 2007.
- [23] T. H. Sloane, "Effects of switching frequency and input voltage on efficiency of chopper-controlled series-connected DC machines," *IEEE Industry Applications Society Conf. (IAS)*, pp. 164-168, Oct. 1988.
- [24] H. W. Lee, T. H. Kim, and M. Ehsani, "Practical control for improving power density and efficiency of the BLDC generator," *IEEE Trans. Power Electron.*, vol. 20, no. 1, pp. 192-199, Jan. 2005.
- [25] A. I. Maswood, "A PWM voltage source inverter with PI controller for instantaneous motor current control," *IEEE Power Electronics and Drive Systems Conf. (PEDS)*, pp. 834-837, 1995.
- [26] J. Rodriguez, J. Pontt, C. Silva, P. Cortes, U. Amman, and S. Rees, "Predictive current control of a voltage source inverter," *IEEE Power Electronics Specialists Conf. (PESC)*, vol. 3, pp. 2192-2196, Jun. 2004.
- [27] B. H. Cho, H. S. Bae, and J. H. Lee, "Review of current mode control schemes and introduction of a new digital current mode control method for the parallel module DC-DC converters," *IEEE Power Electronics and Motion Control Conf. (IPEMC)*, pp. 202-210, May 2009.
- [28] Y. Duan and H. Jin, "Digital controller design for switchmode power converters," *IEEE Applied Power Electronics Conf. (APEC)*, pp. 967-973, May 1999.
- [29] Y. F. Liu and X. Liu, "Recent developments in digital control strategies for DC/DC switching power converters," *IEEE Power Electronics and Motion Control Conf. (IPEMC)*, pp. 307-314, May 2009.
- [30] B. H. Cho, H. S. Bae, and J. H. Lee, "Review of current mode control schemes and introduction of a new digital current mode control method for the parallel module dc-dc converters," *IEEE Power Electronics and Motion Control Conf. (IPEMC)*, pp. 202-210, May 2009.
- [31] D. M. Van De Sype and K. De Gussemé "Small-signal Laplace-domain analysis of uniformly-sampled pulse-width modulators," *IEEE Power Electronics Specialists Conf. (PESC)*, vol. 6, pp. 4292-4298, Jun. 2004.

- [32] W. Wang, Z. Wu, W. Jin and J. Ying, "Sensorless control technology for single phase BLDCM based on the winding time-sharing method," *IEEE Industrial Electronics Society Conf. (IECON)*, pp. 5, Nov. 2005.
- [33] W. Wang, Z. Wu, W. Jin, J. Ying, S. M. Huang, and W. S. Huang, "Method and circuit for controlling sensorless single-phase BLDCM," United States Patent, US 0,214,611.
- [34] 路承達, 劉添華, "無轉軸偵測元件單相風扇驅動系統及其積體電路晶片研製" 台灣電力工程研討會, 2008.
- [35] 潘屏榮, 吳永裕, 陳遵立, "應用於雙相半波無刷直流風扇馬達之無感測轉速控制技術" 台灣電力工程研討會, 2008.
- [36] J. C. Dunfield, G. K. Heine, M. Jufer, and K. Oveyssi, "Method for starting and commutating a permanent-magnet direct current motor having a single phase winding," United States Patent, US 5,598,071.
- [37] B. I. Kwon, B. Y. Yang, S. C. Park, and Y. S. Jin, "Novel topology of unequal air gap in a single-phase brushless DC motor," *IEEE Trans. Magnetics*, vol. 37, no. 5, pp. 3723-3726, Sep. 2001.
- [38] W. Wang, Z. Wu, W. Jin, and J. Ying, "Starting methods for hell-less single phase BLDC motor," *Industrial Electronics Society Conf. (IECON)*, Nov., 2005.
- [39] 鄭光耀, 「無刷直流馬達無感測控制方法之研究與DSP實現技術之發展」, 博士論文, 國立交通大學電機與控制工程研究所, 民國九十二年十月。
- [40] 賴逸軒, 「以DSP為基礎發展永磁同步馬達使用線性型霍爾感測器與無感測控制方法」, 碩士論文, 國立交通大學電機與控制工程研究所, 民國九十四年七月。
- [41] 張晏銓, 「永磁無刷馬達使用霍爾感測器或無感測之數位控制器設計」, 碩士論文, 國立交通大學電機與控制工程研究所, 民國九十六年七月。

作者簡介

個人資料

姓名：陳煒超 (Wei-Chao Chen)

生日：民國 74 年 4 月 25 日

出生地：台灣省台北縣

專長：DSP 應用、數位電路設計與應用、

無刷直流風扇馬達系統設計與無感測控制



學歷

2007.9 ~ 2009.7 交通大學電機與控制工程研究所

2003.9 ~ 2007.6 交通大學電機與控制工程學系

2000.9 ~ 2003.6 台北市立建國高級中學

1997.9 ~ 2000.6 台北縣私立南山中學

1989.9 ~ 1995.6 台北縣立中和國小

